[21a-P01-1~8] 4 JSAP-Optica Joint Symposia 2023 (Poster)

Thu. Sep 21, 2023 9:30 AM - 11:30 AM P01 (KJ Hall)

△ : Presentation by Applicant for JSAP Young Scientists Presentation Award

▲ : English Presentation

▼ : Both of Above

No Mark : None of Above

▲[21a-P01-1] Yb-doped Fiber Pulse Laser Capable for Highspeed Wavelength Scanning

○Yifan Ma[1], Bowen Liu[1], Maolin Dai[1], Sze Yun Set[1], Shinji Yamashita[1] (1.Tokyo Univ.)

9:30 AM - 11:30 AM

▲[21a-P01-2] Nonlinear Optical Response of Jahn-Teller Susceptible Mixed Transition Metal Oxide

○(D)Ankit Sharma[1], Mansi Pathak[2], C S Rout[2], K V Adarsh[1] (1.IISER Bhopal India, 2.Jain University, Bangalore, India)

9:30 AM - 11:30 AM

▲[21a-P01-3] Unveiling NiFe2O4 Nanoparticles as an Efficient Nonlinear Optical Limiter

○(D)Naresh Aggarwal[1], Pratik V. Shinde[2], Chandra Sekhar rout[2], Adarsh K. V.[1] (1.Department of Physics, Indian Inst. of Science Education and Research, Bhopal,462066, India, 2.Centre for Nano and Materials Science, Jain Univ., Ramanagaram, Bangalore,562112, India)

9:30 AM - 11:30 AM

▲[21a-P01-4] Kerr nonlinearity in tailoring dispersion characteristics in optical fiber using a numerical analysis

○(D)Mitali Sahu[1], Partha Roy Chaudhuri[1] (1.IIT Kharagpur)

9:30 AM - 11:30 AM

▲[21a-P01-5] Analyzing Photopigments in Medicinal Plant Leaves using UV-Vis Spectroscopy

○(B)MANIKANTH KARNATI[1], ADITI NAIK[1], GAGAN RAJU[1], SHARMILA SAJANKILA NADUMANE[1], NIRMAL MAZUMDER[1] (1.Manipal Academy of Higher Education (MAHE))

9:30 AM - 11:30 AM

▲[21a-P01-6] Nonlinear Coherent Light-matter Interaction: Promising all-Optical Switching, Logic Gate and Optical Limiting Applications

○(D)Sudhanshu Kumar Nayak[1], Md Soif Ahmed[1], Chinmay Barman[1], Rahul Murali[1], Bota Bhavani[2], Seelam Prasanthkumar[2], Lingamallu Giribabu[2], Sai Santosh Kumar Raavi[1] (1.Ultrafast Photophysics and Photonics Laboratory, Department of Physics, Indian Institute of Technology Hyderabad, Kandi 502285, Telangana, India, 2.Polymers &Functional Materials Division, CSIR-Indian Institute of Chemical Technology, Tarnaka, Hyderabad-500007, India)

9:30 AM - 11:30 AM

▲[21a-P01-7] Exploring Ultra-broad Supercontinuum Generation Using Chalcogenide Fiber

○(D)Protik Roy[1], Partha Roy Chaudhuri[1] (1.IIT Kharagpur)

9:30 AM - 11:30 AM

▲[21a-P01-8] Raman scattering on two-soliton interaction in silica and chalcogenide (As_2Se_3) optical fibers

○(D)Abhisek Roy[1], Partha Roy Chaudhuri[1] （1.IIT Kharagpur）

9:30 AM - 11:30 AM

高速波長走査用 Yb ファイバパルスレーザ
Yb-doped Fiber Pulse Laser Capable for Highspeed Wavelength Scanning

東京大学先端研[1], ○麻　一凡[1], 戴　茂林[1], 柳　博文[1], セット　ジイヨン[1], 山下　真司[1]
The University of Tokyo.[1], ○ Yifan Ma[1], Maolin Dai[1], Bowen Liu[1], Sze Y. Set[1] and Shinji Yamashita[1]
E-mail: mayifan@g.ecc.u-tokyo.ac.jp

In recent years, femtosecond pulse laser has gained increasing recognition, predominantly due to its capacity for wavelength conversion and high peak power. Making it an advantageous tool for implementing spectroscopy techniques, notably Scattering Raman Spectroscopy (SRS) and Coherent Anti-Stokes Raman Spectroscopy (CARS). However, high-speed spectroscopy scanning traditionally poses a challenge [1]. Conventional tuning strategies, such as the optical parametric oscillator, often demand distinct crystal tilting angles, thereby necessitating complicated control units. This preference for external strategies tends to demand greater effort, thus presenting an area ripe for innovation and improvement.

Yb-doped fiber mode-locking laser, as a reliable laser source, its structure is well developed. We have constructed a traditional Yb-doped femtosecond laser, system layout shown in Fig.1(a) and plan to achieve wavelength scanning through its spatial filtering section, eventually applied in the subsequent SRS system. As result, we obtain pulse centered around 1020 nm, with a duration of 874 fs (Fig1(c)), repetition rate of 161 MHz and average power over 400 mW. It should be noted that the FWHM of spectrum is 6 nm, thus the pulse can be compressed further.

Within the laser cavity, the laser light passes through two gratings to achieve spectroscopic separation. By adjusting the position of collimator 2, we can direct light of different wavelengths into the fiber, thus realizing different wavelength resonances. As Nonlinear Polarization Evolution (NPE) mode-locking is relatively sensitive, typically, changes in resonance wavelength necessitate concurrent changes in polarization control, otherwise the laser could easily lose its lock. To mitigate this, we maintain a negative dispersion within the cavity, ensuring relatively stable soliton mode-locking. In addition, we have selected a particularly stable mode that is self-starting, and we continuously collected spectral data over a 12-hour period to ascertain its stability.

Currently, by adjusting the position of collimator 2 using the mirror frame, we have achieved a wavelength tuning range of 17 nm as shown in Fig.1(b). This is not our limit; the adjustment range of the collimator mount has reached its maximum, and the speed is not fast enough. We only demonstrate its tunability in this paper. For next step, we plan to add a scanning galvo followed by the grating pairs, which will enable us to achieve a wider range of tuning and ultra-high-speed scanning.

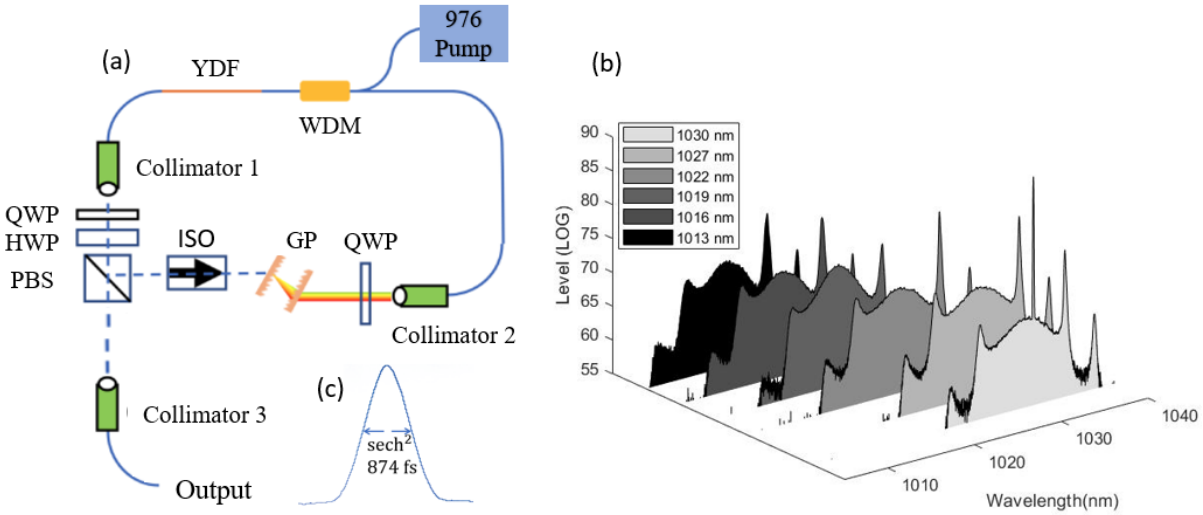

Figure 1 (a) System Layout. (b) Tuning range by moving the collimator mount. (c) Autocorrelation and pulse width

[1] Smith, E., & Dent, G. (2019). *Modern Raman spectroscopy: a practical approach*. John Wiley & Sons.

Nonlinear Optical Response of Jahn-Teller Susceptible Mixed Transition Metal Oxide

Ankit Sharma [1], Mansi Pathak [2], C.S Rout[2], K.V. Adarsh[1]

[1]Department of Physics, Indian Institute of Science Education and Research, Bhopal, 462066 India

[2]Centre for Nano and Materials Science, Jain University, Ramanagaram, Bangalore, 562112, India

E-mail: adarsh@iiserb.ac.in

The sustainability of optical nonlinearities of material systems is crucial for future technological and fundamental importance e.g., optical switching, signal processing, second harmonic generation, solar energy harvesting, optical limiting, frequency-comb, etc. In the last four decades, extensive works had been dedicated to advances in the nonlinear optics field but still, we rely on metal chalcogenides, $LiNbO_3$, BBO, etc. as a nonlinear crystal for technological applications. However, several groups have demonstrated different materials systems with relatively enhanced optical nonlinearities and their prospects, e.g., 2D TMDCs, vertical and horizontal heterostructures, and inorganic and organic perovskites. But they are still in the struggling stage for device applications due to their low growth yield, and high instability. Here, we have chosen mixed transition metal oxides $MnCo_2O_4$ and demonstrated its nonlinear optical response. Mostly, oxides are known for higher stability and wide bandgap materials and consequently, they are transparent for the visible and infrared regime. But the oxides from mixed transition metals with partially filled d-orbital provide an additional degree of freedom to exploit their oxides in the visible regime. Partial d-orbital of transition metals with tetrahedral/octahedral goes through structural distortion and stabilized the system energetically by splitting the conduction band into low and high-spin states. We exploit these properties and observed two optically active bands in optical absorption spectroscopy at ~ 768 nm and ~ 507 nm. Further, we investigated its third-order susceptibility by incorporating the open (OA) and close (CA) aperture standard Z-scan technique. We used 7 ns, 532 nm Gaussian shape laser excitation at 53 MW/cm2 and observed the valley at a tight focusing position with two shoulder peaks near the focus which is evidence of excited state absorption. Interestingly, the CA transmittance profile revealed the Kerr lensing effect i.e., self-focusing properties of $MnCo_2O_4$ under similar excitation. Finally, our study proposed another material system that can be a potential candidate for optics and photonics applications and therefore needs to be investigated extensively for the fundamental understanding of these emerging materials.

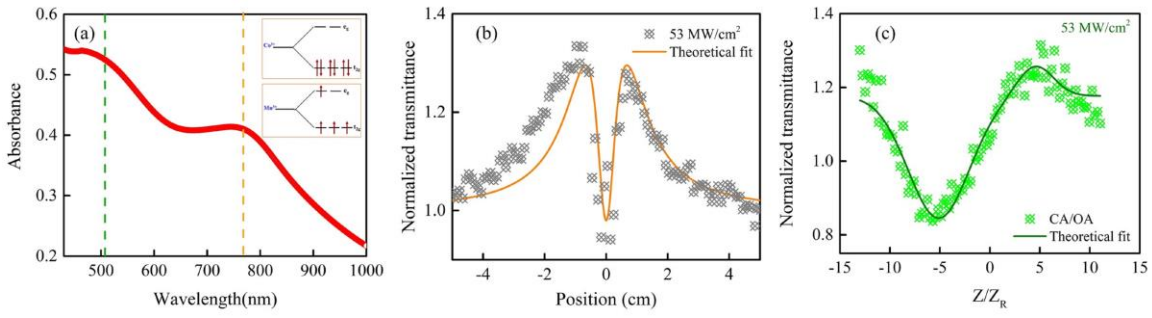

Figure 1: (a) Two split peaks which demonstrate the high and low spin state of Co^{3+}/Mn^{3+} and Co^{2+}, (b) excited state absorption via open-aperture Z-scan, and (c) close aperture Z-scan at 532 nm laser excitation.

Unveiling $NiFe_2O_4$ Nanoparticles as an Efficient Nonlinear Optical Limiter

Naresh Aggarwal[1], Pratik V. Shinde[2], Chandra Sekhar Rout[2], K. V. Adarsh[1*]

[1]Department of Physics, Indian Institute of Science Education and Research, Bhopal,462066, India

[2]Centre for Nano and Materials Science, Jain University, Ramanagaram, Bangalore,562112, India

[*] Email Corresponding author: adarsh@iiserb.ac.in

Ternary transition metal oxides (TMOs) belong to an exciting branch of material due to their high used in supercapacitors because of their excellent electrochemical properties and multiple oxidation states. Nickel ferrite oxides $NiFe_2O_4$ (NFO) are also a member of the TMOs family which have very high optical limiting strength and quick response time and have also been used in the field of pseudo-capacitors., however the nonlinear optical response of NFO is still not explored in detailed. In this article, we tailored the nonlinear optical limiting response of NFO nanoparticles and tuned its nonlinear behavior as a function of intensity for its applications as one of the best optical limiter materials. Here, we investigate the nonlinear optical performance of NFO by using the Z-scan technique based on third-order nonlinear processes in which we excite the sample by a nanosecond laser whose pulse width is 7ns and photons have energy around 2.33eV. We observed that NFO shows reverse saturable absorption behavior with a very large absorption coefficient β in the order of 10^2 cm/GW and a very low optical onset (F_{ON}) as compared to many other TMOs materials and hence it can be a hallmark material for using optical limiting applications. We also observed that NFO has a negative nonlinearity response with a nonlinear refractive index around $10^{-4}cm^2\ GW^{-1}$, which exposes its self-defocusing nature. Overall, our studies demonstrate that NFO is also a hallmark material for use as a good optical limiting material as well as a supercapacitor.

Kerr nonlinearity in tailoring dispersion characteristics in optical fiber using a numerical analysis

Mitali Sahu and Partha Roy Chaudhuri*
Department of Physics, Indian Institute of Technology Kharagpur-721 302, INDIA
*Corresponding author: roycp@phy.iitkgp.ac.in

Abstract: This work provides a useful study of the dispersion properties exhibited by standard silica fiber in the presence of Kerr nonlinearity utilizing our developed code based on Finite Difference Method (FDM).

Analysis algorithm: We devised a simple analysis method starting with Helmholtz equation for nonlinear (NL) refractive index (RI) distribution with FDM discretization by rearranging this into a matrix eigenvalue problem. For 2-dimensional analysis, the Helmholtz equation takes the form as,

$$\frac{\partial^2\psi}{\partial x^2}+\frac{\partial^2\psi}{\partial y^2}+k_0^2 n_{NL}^2\Psi(x,y)=\beta^2\psi \quad (1)$$

where, $n_{NL}^2=n_0^2+2\bar{n}_2 n_0\left(\frac{P}{A_{eff}}\right)$, n_0 and $\bar{n}_2$ are the linear RI and NL index coefficient of the corresponding medium respectively. A_{eff} is the effective area of the guided mode and the input power distribution P, takes as a Gaussian distribution form, $P=P_{max}e^{\frac{-(x^2+y^2)}{\gamma^2}}$, γ is the spot size of the input field [2].

After discretizing the above equation (1) using FDM, we get

$$\frac{\Psi_{m+1,n}-2\Psi_{m,n}+\Psi_{m-1,n}}{(\Delta x)^2}+\frac{\Psi_{m,n+1}-2\Psi_{m,n}+\Psi_{m,n-1}}{(\Delta y)^2}+k_0^2 n_{m,n}^2\Psi_{m,n}=\beta_{m,n}^2\Psi_{m,n} \quad (2)$$

where m, n = 0, 1, 2 …i.Here, $\psi_{m,0}=\psi_{m,i}=\psi_{0,n}=\psi_{i,n}=0$ condition is taken as the field distribution represents a guided mode of the fiber, under the mode condition: Clad RI $(n_{cl})<n_{eff}=\frac{\beta}{k_0}<$ Core RI (n_c). The final wave equation in the discretized form is,

$$(D_{xx}\otimes I+I\otimes D_{yy})\psi_{m,n}+k_0^2 n_{NLm,n}^2\psi_{m,n}=\beta_{m,n}^2\psi_{m,n} \quad (3)$$

The state representation in 2-dimemsion is represented in grid form with dimension $(m-1)\times(m-1)$ and the Laplacian is expressed as a sum of two sparse matrices D_{xx} and D_{yy} with the Kronecker multiplication with an identity matrix (I).

Numerical results:

We have extensively studied several situations. As typical results, we show in figure (1) and (2), the dispersion shifting and the dispersion flattening respectively with the change in input power and spot size in Kerr nonlinearity. Thus, the standard fiber exhibits a dispersion flat characteristic owing to its inherent nonlinearity.

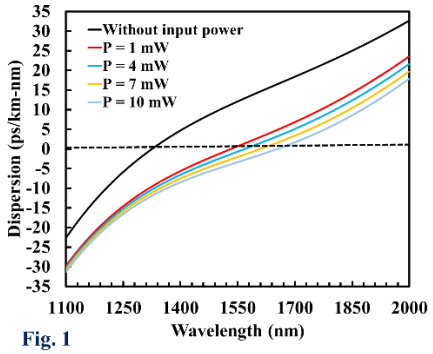

Fig. 1

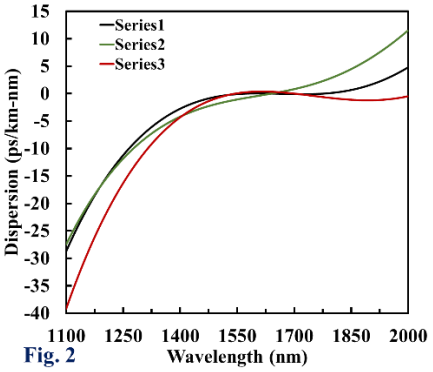

Fig. 2

Conclusion:

This study employs a simple numerical approach, based on FDM, to investigate the Kerr nonlinearity. Through the manipulation of input power, we successfully induce a shift in the dispersion curve within the C-band range (1550 nm window). Additionally, by adjusting the spot size (γ) and peak input power ($Pmax$) simultaneously, we effectively flatten the dispersion near the zero-dispersion point around the C-band region. These findings clearly reveal the potential for developing Dispersionless telecommunications system, thereby establishing exciting prospects for future nonlinear research.

References:

[1] Introduction to fiber optics by Ajoy Ghatak and K. Thyagarajan.
[2] M. Koshiba and K. Saitoh, "Structural dependence of effective area and mode field diameter for holey fibers," Opt. Express 11, 1746-1756 (2003).
[3] S. Roy and P. Roy Chaudhuri, "Analysis of Nonlinear Multi-layered Waveguides and MQW Structures: A Field Evolution Approach Using Finite-Difference Formulation," in IEEE Journal of Quantum Electronics, vol. 45, no. 4, pp. 345-350, April 2009.
[4] S.K. Mondal, S.N. Sarkar, “Effect of optical Kerr effect nonlinearity on LP, mode cutoff frequency of single-mode dispersion-shifted and dispersion-flattened fibers,” Optics Communications, vol 127, pp. 25-30, 1996.

Analyzing Photopigments in Medicinal Plant Leaves using UV-Vis Spectroscopy

Manikanth Karnati, Aditi Naik, Gagan Raju, Sharmila Sajankila Nadumane, Nirmal Mazumder*

Department of Biophysics, Manipal School of Life Sciences, Manipal Academy of Higher Education, Manipal, Karnataka, India-576104

*Corresponding author: nirmal.mazumder@manipal.edu

1. Objective:

Photopigment degradation in the leaf directly impacts the quality of the leaf over time during storage. The present study employs time dependant Uv- vis spectroscopic analysis for analysis of the nature of the leaf during storage.

2. Introduction:

Plants contain medicinal components which are essential for treating many different diseases. Research has indicated that numerous plants contain chemical compounds, among the noteworthy active elements found in plants are alkaloids, flavonoids, terpenoids, tannins, and saponins. These plant phenolic compounds can be found abundantly in various plant components, especially within the cells responsible for photosynthesis. UV-vis spectroscopy is a non-invasive technique in which the photopigments in the leaf absorb the light at different wavelengths which helps in analyzing the characteristic properties of the photopigments.

3. Material and methods:

The material used were leaves of *Ocimum tenuiflorum*, *Catharanthus roseus*, *Cymbopogon citratus*, and *Hibiscus syriacus*, a 96-well plate, puncher, ethanol, and microplate reader. The four different leaves were collected from the greenhouse, and the dorsal and ventral punches of the leaves (the size of each punch is 8mm) were made using a puncher and were loaded in flat-bottom, 96-well plates and stored at the experiment conditions before being studied. UV-Vis absorbance spectroscopic measurements were acquired using the Tecan Spark spectrophotometer and the Spark Control Magellan V 3.1 software, over the spectral range of 250-800 nm, having a scanning wavelength of step size 2 nm with the bandwidth being 5 nm. The samples were stored at room temperature and the measurement was taken every day up to day 6 to understand the degradation of photopigments with time.

4. Results and discussions:

The spectral reading was collected till day 6, then the graphs were plotted and analyzed. The chlorophyll peak was obtained between 650nm-700nm for all plants on all days. It's also observed that in plants like hibiscus the intensity of photopigments is very high and does not degrade faster, this can be stored for a longer time and its maximum medicinal properties can be retained within the leaf, whereas other leaves have a rapid deterioration of photopigment which will directly affect the medicinal properties of the leaf, during long storages. The decrease in intensity photopigment leads to a decrease in phenolic compounds present in plant cells.

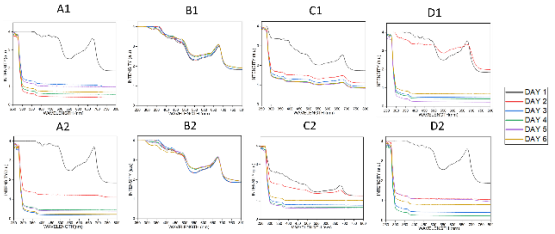

Figure 1: UV-Vis spectroscopy of 4 different medicinal leaves. dorsal side of leaves(A1-D1) and ventral side of leaves (A2-D2).left to right the plants are *Catharanthus roseus, Hibiscus syriacus, Cymbopogon citratus, and Ocimum tenuiflorum.*

5. Conclusion:

Results clearly show that with increasing storage time the photopigment intensity deteriorates and will in turn affect the medicinal properties of the leaf hence the freshly plucked leaves have better medicinal properties than the leaves stored for long durations.

Acknowledgment:

We thank Manipal School of Life Sciences, Manipal, Karnataka, India for providing infrastructure and facilities.

References:

[1]Wulandari, Lestyo, Yuni Retnaningtyas, and Hilmia Lukman. "Analysis of flavonoid in medicinal plant extract using infrared spectroscopy and chemometrics." *Journal of Analytical Methods in Chemistry* 2016 (2016).

[2] Banik, Soumyabrata, et al. "Spectroscopic methods for assessment of hand sanitizers." *Chemical Papers* 76.8 (2022): 4907-4918.

[3] Banik, Soumyabrata, et al. "Analysing the Oxidation Status of Mustard Oils using Spectroscopic Methods: a Preliminary Study." *Laser Science*. Optica Publishing Group, 2021.

Nonlinear Coherent Light-matter Interaction: Promising all-Optical Switching, Logic Gate and Optical Limiting Applications

Sudhanshu Kumar Nayak,[a] Md Soif Ahmed,[a] Chinmay Barman,[a] Rahul Murali,[a] Bota Bhavani,[b] Seelam Prasanthkumar,[b] Lingamallu Giribabu,[b] Sai Santosh Kumar Raavi[a,*]

[a]Ultrafast Photophysics and Photonics Laboratory, Department of Physics, Indian Institute of Technology Hyderabad, Kandi 502285, Telangana, India
[b]Polymers & Functional Materials Division, CSIR-Indian Institute of Chemical Technology, Tarnaka, Hyderabad-500007, India
**Corresponding author Email address: sskraavi@phy.iith.ac.in*

Spatial self-phase modulation (SSPM) is a nonlinear optical (NLO) coherent interaction between light and matters. The phase gets self-modulated due to the change of nonlinear refractive index through the nonlinear Kerr effect and produce diffraction rings at the far fields. [1] Porphyrins are the organic molecules with π-conjugation electron rich systems, they possess delocalized electric field distribution and large dipole moments that lead to have significant electrical polarization, which is a profit for higher NLO response. These molecules have various application in photovoltaics, photonics, optoelectronics, etc. [2, 3] Herein, we report the NLO properties of four metalated porphyrin-napthalimide based donor-acceptor systems named as PN-Zn, PN-Ni, PN-Cu, and PN-Fb using SSPM and continuous wave (CW) Z-scan method for exploring various optoelectronic applications like optical limiting, optical switching, and logic gates, etc.

We have performed SSPM of four samples using three different lasers of wavelengths λ=433 nm, 532 nm, and 636 nm. We have observed the number of diffraction rings (N) increases linearly with increase in intensity (I) of laser. This is because, the particles get polarized and oriented along the direction of the electric field of incident light which increased with intensity of light through SSPM effect. From slope dN/dI (N vs I graph), we have calculated the nonlinear refractive index (n_2) and nonlinear susceptibility (χ^3) using formulae [1] with values (1.72-3.82)×10^{-5} cm^2/W and (0.88-1.67)×10^{-3} esu, respectively. The SSPM results of PN-Zn with all three laser excitations is shown in Fig. 1(a), (b). All the obtained SSPM results are mentioned in Table 1. The experimental details of NLO Z-scan methods discussed elsewhere [4] has been performed using 532 nm laser excitations and data has been shown in Fig. 1(d). Different NLO parameters are extracted and calculated from Z-scan methods using the equations taken from the references [4, 5] . From open-aperture (OA) Z-scan we observed these molecules showed reverse saturable absorption (RSA) with values of two-photon absorption coefficients were in the range of ~ (0.84-4.1) × 10^{-3} cm/W. From closed-aperture (CA) Z-scan, values of n_2 and χ^3, mentioned in Table 2. From both measurements SSPM and Z-scan, we have observed the PN-Zn shows larger nonlinearities followed by PN-Ni, PN-Cu, and PN-Fb and the order difference in n_2 and χ^3 due to the different incident intensities used in both measurements.

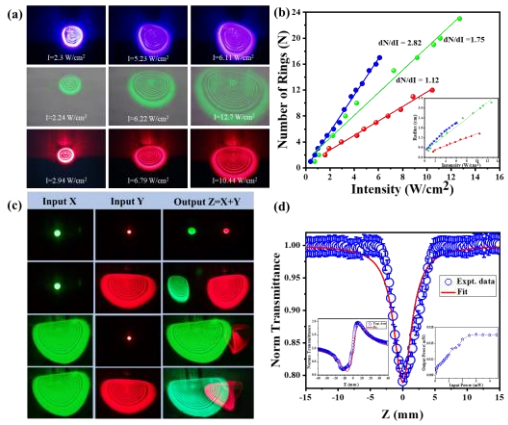

Table 1 (SSPM Results)

Sample	λ_{inc} (nm)	n_2 (cm^2/W) × 10^{-5} (10 mm/1 mm)	χ^3 esu × 10^{-3} (10 mm/1 mm)
PN-Zn	532	3.82/11.8	1.67/6.03
PN-Ni	532	2.81/6.39	1.44/3.54
PN-Cu	532	2.45/6.0	1.25/3.06
PN-Fb	532	1.72/5.62	0.88/2.87
PN-Zn	433	4.4 (10 mm)	2.25 (10 mm)
PN-Zn	636	2.51 (10 mm)	1.28 (10 mm)

Table 2 (Z-scan Results)

Sample	β (cm/W) × 10^{-3}	n_2 (cm^2/W) × 10^{-7}	χ^3 esu × 10^{-5}	OL onset (mW)
PN-Zn	4.09	1.71	8.81	2.7
PN-Ni	1.83	1.18	6.36	3.0
PN-Cu	1.57	1.02	6.12	3.5
PN-Fb	0.72	0.99	5.18	4.0

Fig. 1. (a) SSPM result of PN-Zn with excitation of λ=433 nm, 532 nm, and 636 nm, (b) The plot of diffraction ring numbers (N) versus laser intensity (I) for λ = 433, 532, and 636 nm with radius vs intensity (inset), (c) XSPM OR gate results in PN-Zn, (d) OA Z-scan, CA Z-scan and optical limit (inset) of PN-Zn.

The OR logic gate demonstration in PN-Zn has been performed by cross self-phase modulation (XSPM) using 532 nm, and 636 nm laser, the output satisfied with OR-Logic gate conditions, as shown in Fig. 1(c). The optical limiting (OL) study of PN-Zn is shown in the inset of fig. 1(d) with OL onset at 2.7 mW. Therefore, these measurements provide promising evidence that these molecules can be suitable for all-optical switching, OR-Logic gate, optical limiting optoelectronics NLO applications.

References

1. Sk, K., et al., *Nonlinear Coherent Light–Matter Interaction in 2D MoSe2 Nanoflakes for All-Optical Switching and Logic Applications.* Advanced Optical Materials, 2022. **10**(19): p. 2200791.
2. Ahmed, M.S., et al., *Metalated porphyrin-napthalimide based donor-acceptor systems with long-lived triplet states and effective three-photon absorption.* Journal of Photochemistry and Photobiology A: Chemistry, 2023. **435**: p. 114324.
3. Nayak, S.K., et al., *Femtosecond nonlinear optical properties of polycyclic aromatic hydrocarbon-based Benzo [e] pyrene derivatives.* Optical Materials, 2023. **137**: p. 113603.
4. Ahmed, M.S., et al., *Tunable near-infrared emission and three-photon absorption in lanthanide-doped double perovskite nanocrystals.* Nanoscale, 2023. **15**: p. 9372-9389.
5. Ahmed, M.S., et al., *Enhanced femtosecond nonlinear optical response in Mn-doped Cs2AgInCl6 nanocrystals.* Optics Letters, 2023: p. DOI: 10.1364/OL.494431.

Exploring Ultra-broad Supercontinuum Generation Using Chalcogenide Fiber

Protik Roy[1], Partha Roy Chaudhuri[1]
Indian Institute of Technology Kharagpur, Kharagpur, India
Email - roycp@phy.iitkgp.ac.in

I. Dispersion Engineering

To optimize the design for pulse propagation and Supercontinuum Generation (SCG), we revisited a chalcogenide glass fiber with elliptical and circular core cross-section. We take $As_{40}S_{60}$ and $As_{42}S_{58}$as core and cladding materials for standard step index fiber. By optimizing the fiber structure, we calculate the nonlinear coefficient (γ), and the group velocity dispersion (GVD, β_2), for the fundamental modes of the fibers. Table 1 presents the associated data obtained from our observations.

Table 1

	Near Zero Dispersion Wavelength (NZDW)	β_2 at NZDW (ps^2/m)	γ at NZDW $(W^{-1}m^{-1})$
Elliptical core	2.8 µm	-0.05	0.22
Circular core	3.15 µm	-0.01	0.13

By incorporating the typical parameters mentioned, we simulate the propagation of ultrafast pulses using a generalized nonlinear Schrodinger equation (GNLSE) [1], which is expressed as follows:

$$\frac{\partial}{\partial z}A + \frac{\alpha}{2}A + \left(\sum_{k\geq 2}\beta_k \frac{i^{k-1}}{k!}\frac{\partial^k}{\partial T^k}\right)A = i\gamma\left(1+\frac{1}{\omega_0}\frac{\partial}{\partial T}\right)\times\left((1-f_R)|A|^2 + f_R\int_0^\infty h_R(\tau)\,|A(z,T-\tau)|^2 d\tau\right)A \quad (1)$$

The response function R(T) of a system, which describes its nonlinearity, incorporates both immediate and delayed Raman effects. It can be expressed as,

$$R(T) = (1-f_R)\delta(T) + f_R h_R(T) \quad (2)$$

where f_R represents the fractional contribution of the delayed Raman response to the system's nonlinear polarization. It takes the value of 0.148 [2]. The Raman response term, h_R, is given by the expression

$$h_R = \frac{\tau_1^2+\tau_2^2}{\tau_1\tau_2^2} exp(-\tau/\tau_2) sin(-\tau/\tau_1) \quad (3)$$

For Chalcogenide materials, these are 23 fs and 164.5 fs, respectively [2]. The incident pump pulse is assumed to be a hyperbolic secant pulse, which can be represented as follows:

$$A(0,T) = \sqrt{P_0}\, sech\left(\frac{T}{T_0}\right) \quad (4),$$

where P_0 and T_0 are the peak input power and the pulse duration (1/1.763 of the full width at half maxima duration for the input pulse) respectively

Fig.1 presents the numerical results related to SCG obtained by launching a secant hyperbolic pulse with a width of 200 fs, and a peak power of 1 kW at a wavelength of 3.15 µm into a 10 cm long circular core fiber. The result demonstrates the SCG of 2.1 µm wavelength band at a distance of 4.2 cm. In the case of the elliptical core fiber shown in Fig. 2., the input pulse experiences the SCG of 2.2 µm at a distance of 3.3 cm when the pulse is launched at 2.8 µm wavelength. It is noteworthy that when utilizing an elliptical cross-section, the flat wavelength band further increases and this flatness is achieved with a shorter fiber length.

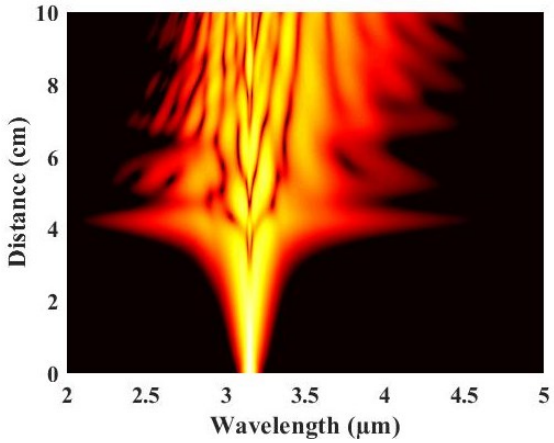

Fig. 1 SCG for circular core fiber.

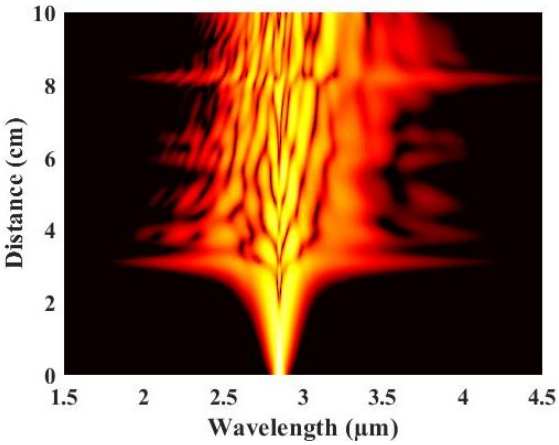

Fig. 3 SCG for elliptical core fiber.

III. Conclusion

This investigation establishes that modifying the cross-section of a fiber can enhance the flatness in the wavelength band caused by the nonlinearity in the medium, particularly with chalcogenide fiber. These findings suggest that carefully engineered chalcogenide fibers, with optimized dispersion and nonlinearity, hold great promise as efficient devices for generating broadband femtosecond infrared (IR) pulses while minimizing power consumption. Such advancements have significant implications for applications in the 2-5 µm wavelength range.

References

[1] G. P. Agrawal, Nonlinear Fiber Optics, 1989, Chap. 6.
[2] A. Salem, R. Cherif, and M. Zghal, “Raman Response of a Highly Nonlinear As 2 Se 3 -based Chalcogenide Photonic Crystal Fiber,” Progress in Electromagnetics Research Symposium (2011).

Raman scattering on two-soliton interaction in silica and chalcogenide (As_2Se_3) optical fibers

Abhisek Roy and Partha Roy Chaudhuri*
Department of Physics, Indian Institute of Technology Kharagpur
*Email: roycp@phy.iitkgp.ac.in

We study and explore the two-soliton interaction in silica and chalcogenide (As_2Se_3) fibers. For this, we focus on two temporally separated solitons in a single-mode fiber, revealing significant modification of Kerr-induced interaction by interpulse Raman scattering.

I. Dispersion Parameters for Soliton Interaction

We have computed the nonlinear coefficient (γ), and group velocity dispersion (GVD, β_2) for the fundamental mode of the fibers. Table 1 presents the observed values of γ and β_2 at 1500 nm.

TABLE 1

	β_2	γ
SILICA	-1.18×10^{-26}	0.08
CHALCOGENIDE	-5.0×10^{-26}	1.20

II. NUMERICAL MODEL

The equation governing the pulse propagation is expressed in the form:

$$\frac{\partial}{\partial z}A+\frac{\alpha}{2}A+\left(\sum_{k\geq 2}\beta_k\frac{i^{k-1}}{k!}\frac{\partial^k}{\partial T^k}\right)A=i\gamma\left(1+\frac{1}{\omega_0}\frac{\partial}{\partial T}\right)\times$$

$$\left((1-f_R)|A|^2+f_R\int_0^\infty h_R(\tau)\,|A(z,T-\tau)|^2d\tau\right)A \quad (1)$$

The Raman response function $R(T)$ is defined as,

$$R(T)=(1-f_R)\delta(T)+f_Rh_R(T) \quad (2),$$

Here f_R represents the fractional contribution of the delayed Raman response. In case of chalcogenide (As_2Se_3), f_R has the value 0.148 [4]. The Raman response term, h_R, is given by the expression

$$h_R=\frac{\tau_1^2+\tau_2^2}{\tau_1\tau_2^2}exp(-\tau/\tau_2)sin(-\tau/\tau_1) \quad (3)$$

For silica fiber, $\tau_1 = 12.2$ fs, $\tau_2 = 32$ fs, and $f_R = 0.18$.[2] For chalcogenide, these are $\tau_1 = 23$ fs and $\tau_2 = 164.5$ fs.[4]

We considered two incident pump pulses having a hyperbolic secant (sech) shape, as follows,

$$A(0,T)=\sqrt{P_0}\,sech\left(\frac{T-q_0}{T_0}\right)+\sqrt{P_0}\,sech\left(\frac{T+q_0}{T_0}\right) \quad (4),$$

where P_0 and T_0 are the peak input power and the pulse duration respectively. Here, $q_0 = 5\times10^{-13}$s.

We have applied peak power across a range of 200W to 1kW at a wavelength of 1550 nm into 2m long fibers (silica and chalcogenide). In the case of silica fiber, the interaction takes place at ~ 78 cm for a peak power of 200W. For chalcogenide (As_2Se_3), we observe the two-soliton interaction occurring at ~ 30cm at a peak power of 200W. On increasing power, the distance propagated before interaction decreases exponentially for both fibers.

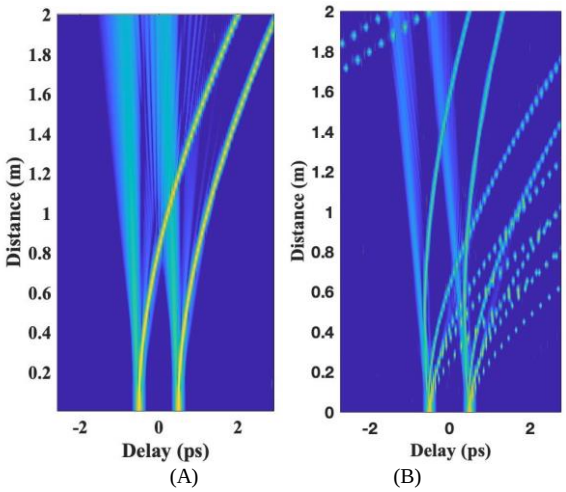

Fig. 1 Two-soliton interaction at peak power of 200W, (A) for silica fiber, and (B) for chalcogenide (As_2Se_3).

III. CONCLUSION

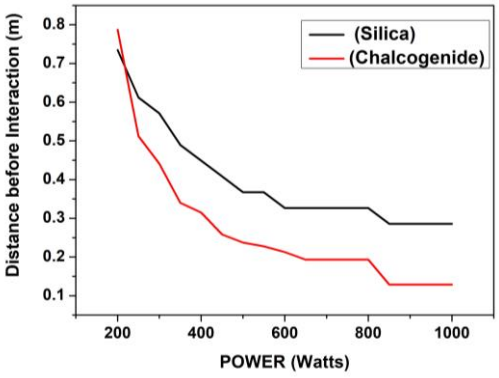

Fig. 2 Variation in interaction distance of two solitons on increasing power.

Our research has focused on the impact of interpulse Raman scattering on the nonlinear interaction between two temporally separated pulses. We have conducted a thorough analysis of the interplay between soliton dynamics and Raman scattering and concluded that, in less nonlinear material, the solitons propagate longer distances without any interaction with lower input power as depicted in silica and chalcogenide fibers. Around 500 W, the separation is maximum between silica and chalcogenide as seen in Fig. 2. These new results will be presented in the conference.

References

[1] G. P. Agrawal, *Nonlinear Fiber Optics*, 1989, Chap. 6.

[2] P. Balla, S. Buch, G.P. Agarwal.*Effect of Raman scattering on soliton interactions in optical fibers*.J. Opt. Soc. Am. B Lett., vol. 34, No. 6, pp. 1247-1254, 2017.

[3] K.Ogusu, K. Shinkawa,*"Optical nonlinearities in As2Se3 chalcogenide glasses doped with Cu and Ag for pulse durations on the order of nanoseconds"*Opt. Exp.,vol. 17,no. 10, 2009.

[19a-A602-1~7] 4.1 Plasmonics and Nanophotonics

Prabhat Verma(Osaka Univ.)

Tue. Sep 19, 2023 9:00 AM - 11:30 AM A602 (KJ Hall)

△ : Presentation by Applicant for JSAP Young Scientists Presentation Award

▲ : English Presentation

▼ : Both of Above

No Mark : None of Above

▲[19a-A602-1] [JSAP-Optica Joint Symposia 2023 Invited Talk] Label-free Raman imaging of saturated and unsaturated fatty acid uptake, storage, and return toward baseline levels in macrophages.

○Alison Jane Hobro[1], Takeshi Sugiyama[1], Nicolas Pavillon[1], Takayuki Umakoshi[1], Prabhat Verma[1], Nicholas Smith[1] (1.Osaka Univ)

9:00 AM - 9:30 AM

▲[19a-A602-2] [JSAP-Optica Joint Symposia 2023 Invited Talk] Tip-enhanced cavity-spectroscopy to control excitonic behaviors at the nanoscale

○Kyoung-Duck Park[1] (1.Pohang University of Science and Technology (POSTECH))

9:30 AM - 10:00 AM

▲[19a-A602-3] Generation of SPASER Pulse by Rapid Adiabatic Passage with Chirped Pump Pulse

○(DC)Ankit Purohit, Akhilesh Kumar Mishra

10:15 AM - 10:30 AM

▲[19a-A602-4] Lamellar Columns Photonic Crystal Mirror with High Reflectivity for Extreme-Ultraviolet Radiation

○(D)CHIH-CHUNG WANG[1], CHAO-TE LEE[2], JIA-HAN LI[1] (1.National Taiwan Univ., 2.Taiwan Instrument Research Inst.)

10:30 AM - 10:45 AM

▼[19a-A602-5] Animation of dielectric metasurface 3D hologram

○(B)TAMAKI ONOZAWA[1], Junpei Beppu[1], Tomokazu Yamaguchi[1], Shunsuke Takahashi[1], Satoshi Ikezawa[2], Kentaro Iwami[1] (1.Tokyo Univ. of Agriculture and Technology, 2.Waseda Univ.)

10:45 AM - 11:00 AM

▼[19a-A602-6] Modified Coupled-Mode Theory on Fluorescent Surface Lattice Resonance

○(P)JoshuaTinYau Tse[1], Shunsuke Murai[1], Katsuhisa Tanaka[1] (1.Kyoto Univ.)

11:00 AM - 11:15 AM

▲[19a-A602-7] Vanadium dioxide-enabled tunable metasurfaces

○(D)Zihang Zheng[1], Kai Sun[1], Yuxin Du[1], Cornelis H. de Groot[1], Xu Fang[1] (1.Univ. of Southampton)

11:15 AM - 11:30 AM

Label-free Raman imaging of saturated and unsaturated fatty acid uptake, storage, and return toward baseline levels in macrophages

a Immunology Frontier Research Center (IFReC), Osaka University, Japan
b Department of Applied Physics, Graduate School of Engineering, Osaka University, Japan
c PRESTO, Japan Science and Technology Agency, Kawaguchi, Saitama 332-0012, Japan
d Open and Transdisciplinary Research Institute, Osaka University, Japan,
Alison J. Hobro*[a], Takeshi Sugiyama[ab], Nicolas Pavillon[a], Takayuki Umakoshi[bc], Prabhat Vermab
and Nicholas Smith*[ad]
E-mail: ajhobro@ifrec.osaka-u.ac.jp, nsmith@ap.eng.osaka-u.ac.jp

Lipids play many important roles in the body including cell signaling and energy storage. The presence of excessive lipids, or disruption of normal lipid metabolic processes in the cell, has been linked to lifestyle diseases such as atherosclerosis and obesity. Where the affected cells are part of the innate immune system such dysregulation of lipids has also been implicated in impaired immune responses to infection. Therefore, understanding how macrophages are affected by the presence of fatty acids in their local environment is an important step in understanding lifestyle disease development. Using Raman spectroscopic imaging we studied the uptake of several concentrations of palmitic, stearic, oleic and linoleic acid in live macrophage cells. Macrophages readily take up these lipids, which can be observed by Raman imaging at the edge of the cytoplasm close to the cell membrane, with the exact distribution dependent on the nature of the fatty acid (unsaturated/saturated) and the exposure concentration. At the highest concentrations, all fatty acids appear to be toxic to the macrophage cells after 24 hours of exposure. By comparing the Raman intensities of the pure fatty acids and ratiometric imaging of the intensities within the macrophage cells we were able to determine that the toxicity of a fatty acid is not due directly to the amount of fatty acid present in the macrophage, rather the nature of the fatty acid is important. This demonstrates the power of high-resolution ratiometric Raman imaging for bioanalysis. In addition, we monitored macrophage cells after removing fatty acids from the surrounding environment, observing a reduction in fatty acid content of the cells over the following 48 hours, showing that even heavily lipid-laden macrophages can process these excess lipids once fatty acids are removed from the environment.

Tip-enhanced cavity-spectroscopy to control excitonic behaviors at the nanoscale

Pohang University of Science and Technology (POSTECH)[1]

Kyoung-Duck Park

E-mail: parklab@postech.ac.kr

The tunability of the bandgap, radiative emission, and energy transfer in transition metal dichalcogenide (TMD) monolayers provides a new class of functions for a wide range of ultrathin photonic devices. Additionally, understanding and controlling the nanoscale transport of excitonic quasiparticles, such as excitons and trions, in atomically thin 2D semiconductors are crucial to produce highly efficient nano-excitonic devices. In this talk, I present a dynamic nano-mechanical strain-engineering of naturally-formed wrinkles in a WSe_2 monolayer, with real-time investigation of nano-spectroscopic properties using tip-enhanced cavity-spectroscopy. We reveal the modified nano-excitonic properties by the induced tensile strain at the wrinkle apex, exhibiting the exciton funneling phenomenon. In addition, we demonstrate a nanogap device to selectively confine excitons or trions of 2D TMDs at the nanoscale, facilitated by the drift-dominant exciton funneling into the strain-induced local spot. Furthermore, we present a method for the all-optical control of the exciton-to-trion conversion process and its spatial distributions in a MoS_2 monolayer. We exploit propagating surface plasmon polaritons (SPPs) to localize hot electrons in a 2D TMD transferred on a metal–insulator–metal (MIM) waveguide. Our work provides a new strategy for robust, tunable, and ultracompact nano-excitonic devices using atomically thin semiconductors.

Generation of SPASER Pulse by Rapid Adiabatic Passage with Chirped Pump Pulse

Ankit purohit**, [£], Akhilesh Kumar Mishra*, [£, †]
[£]Department of Physics, Indian Institute of Technology Roorkee, Roorkee-247667, Uttarakhand, India
[†]Centre for Photonics and Quantum Communication Technology, Indian Institute of Technology Roorkee, Roorkee- 247667, Uttarakhand, India
Email: **a_purohit@ph.iitr.ac.in, *akhilesh.mishra@ph.iitr.ac.in

1. Introduction

The concept of surface plasmon amplification by stimulated emission of radiation (spaser) was proposed by D. Bergman and M. I. Stockman in 2003 [1-3]. The idea is to get coherent plasmon mode in nanoscale regime. In adiabatic rapid passage (ARP), the pump radiation is tuned above the resonance frequency and the radiation is swept through resonance [4].

In this article, we use Gaussian pulse to pump a spaser system. We utilize the concept of ARP and show that a chirp Gaussian pulse is more efficient for population transfer in gain medium [4]. As a result, a large number of localized surface plasmons (LSPs) are obtained.

2. Model

The spaser system consists of metal nanoparticle surrounded by a large number of quantum dots (QDs) [3, 5]. The gain medium is three-level Λ system, where all the population initially is in level $|2\rangle$. The system is pumped by the Gaussian pulse. The Hamiltonian for the proposed geometry is given by

$$H = \sum_p \left[\hbar\left(\Omega_c^p|3\rangle\langle 2| + \Omega_b^p|3\rangle\langle 1| + c.c\right)\right]. \quad (1)$$

The Rabi frequency for $|3\rangle \rightarrow |2\rangle$ transition is written as $\Omega_c = d_{32}.E(t)/\hbar$, where d_{32} is transition dipole moment, $E(t) = Aexp(-i\omega_c t)exp[-(1+iC)t^2/\tau^2]$, C is chirp parameter and τ is pulse width. The Rabi frequency for $|3\rangle \rightarrow |1\rangle$ transition is given by $\Omega_b = d_{31}.E_b(t)/\hbar = \tilde{\Omega}_b a_n(t)$, where $\tilde{\Omega}_b$ is single plasmon Rabi frequency, a_n is LSP annihilation operator. The number of LSPs is given by $N_n = |a_n(t)|^2$. The detailed semiclassical theory, with Hamiltonian and numerical parameters, is covered somewhere else [3, 5].

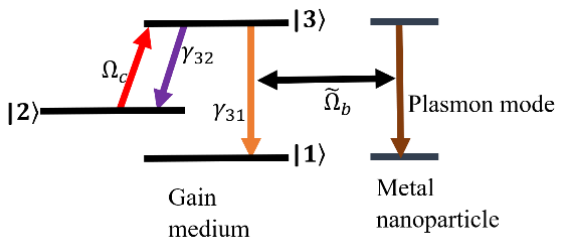

Fig. 1. Schematic of gain medium and metal nanoparticle's energy levels

3. Results and discussion

We solve the Von-Neumann equation given as [5]

$$\dot{\hat{\rho}} = -\frac{i}{\hbar}[H, \hat{\rho}] + L(\rho), \quad (2)$$

where $L(\rho)$ account the decay rates $(\gamma_{32}, \gamma_{21})$. The Gaussian pump pulse has width $\tau = 250\ fs$. The detuning term $\omega_{32} - \omega_c = 5 \times 10^{12} s^{-1}$. The chirped pump pulse induces robust population transfer in gain medium [4], which ultimately leads to the generation of an intense spaser pulse.

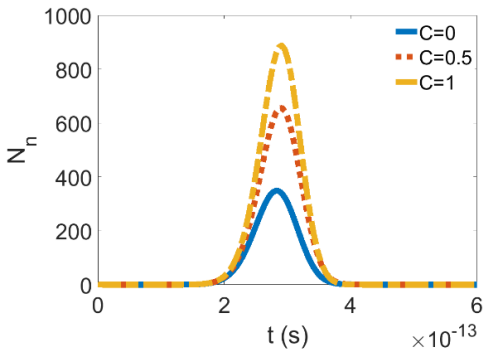

Fig. 2. Temporal evolution of N_n for differently chirped pump pulse.

As depicted in fig. (2), number of LSPs increases with increase in chirp parameter of the Gaussian pump pulse.

4. Conclusion

We reported an enhancement in spaser field induced by chirped Gaussian pump pulse. This was achieved due to robust population transfer in gain medium utilizing ARP.

Acknowledgements

A.P. would like to express sincere thanks to UGC, India for the financial support during this work.

References

[1]. David J. Bergman, and Mark I. Stockman *Physical review letters* **90** (2003) 027402.
[2] Mark I. Stockman, *Optics express* **19** (2011) 22029.
[3]. Mark I. Stockman, *Journal of Optics* **12** (2010) 024004.
[4] V. S. Malinovsky, and J. L. Krause. *The European Physical Journal D-Atomic, Molecular, Optical and Plasma Physics* **14** (2001) 147.
[5] Pankaj K. Jha, Yuan Wang, Xuexin Ren, and Xiang Zhang. *Journal of Optics* **19** (2017) 054002

Lamellar Columns Photonic Crystal Mirror with High Reflectivity for Extreme-Ultraviolet Radiation

Chih-Chung Wang [1], Chao-Te Lee [2], and Jia-Han Li [1,*]

[1] Department of Engineering Science and Ocean Engineering, National Taiwan University, Taipei 106319, Taiwan
[2] Taiwan Instrument Research Institute, National Applied Research Laboratories, Hsinchu 300092, Taiwan
E-mail: d09525016@ntu.edu.tw, * : jiahan@ntu.edu.tw

1. Introduction

For the applications in the extreme ultraviolet (EUV) region, early research [1] revealed that the suitable design of multilayer mirrors with a wavelength of 5 to 50 nm can increase the reflectivity. Li et al. have done related research on Mo/Si multilayer films and proposed vacuum voids mixing in the Si layer can be used to increase the reflectivity for EUV radiation [2]. It is found that the higher proportion of vacuum voids, the higher reflectivity can be obtained from 73.43% for no vacuum voids to 83.24% for full vacuum voids. According to [2], the reflectivity can be effectively improved by vacuum mixing Si layers in 40 pairs of Mo/Si multilayer films. Mo has a larger extinction coefficient than Si in the 13.5 nm wavelength region, so Mo is designed as an absorber to localize into the low-intensity standing wave field. By using a Si layer mixed into the vacuum, the high-intensity regions will have a smaller extinction coefficient, i.e. the imaginary part of the refractive index. The reflectance can be improved by mixing the Si layer in vacuum is because it has more difference between the real parts of the refractive index of the Si layer and the Mo layer; thereby, the interference effect is enhanced. For the multilayer columnar structure mixed into the vacuum layer [3], there are also related researches on the applications in the visible light region. It is not yet found to use similar kinds of structures in extreme ultraviolet light region. In this paper, we propose a hybrid Mo/Si multilayer cylinder-film in control of the constructive interference in multilayer films to enhance reflectivity of EUV radiation.

2. Results and Discussion

We used the finite-difference time-domain numerical method to simulate electromagnetic wave calculations, and constructed 40 pairs of Mo/Si multilayer films and special structures mixed with multilayer films (20 pairs) and cylinders (20 pairs) as shown in Fig. 1. The columns are arranged in a hexagonal grid and the pitch is 13.5 nm, which can make them more closely arranged. In order to increase the air interlayer of Si, the radius of Si in the cylinder remains 50% of the radius of Mo. According to the numerical simulation results as shown in Fig. 2., the reflectivity can be increased to about 81% compared with the conventional 40-period Mo/Si multilayer which has the reflectivity about 75%. However, it can be noticed that when the radius of the pillars becomes larger, the method using the hybrid columnar structure is more effective on reflectivity. It means that the closer the columnar structures are to each other, the greater the reflectivity enhancement effect will be.

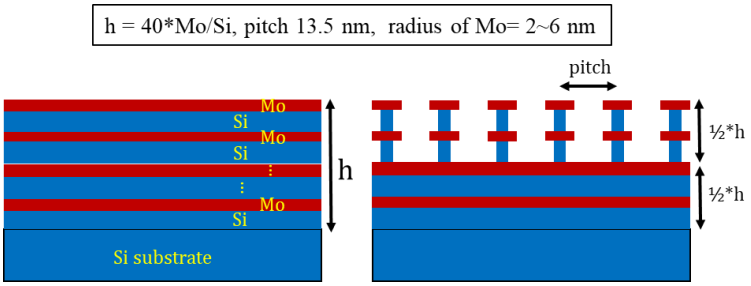

Fig. 1. Traditional 40 pairs of Mo/Si multilayer film (left), and multilayer columns and films mixed (right).

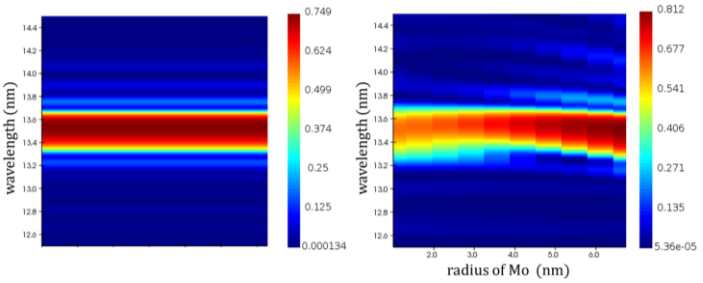

Fig. 2. Reflectivity in 12.5 nm ~ 14.5 nm of traditional 40 pairs of Mo/Si multilayer film (left), and multilayer columns and films mixed (right).

3. Conclusions

We successfully presented Mo/Si multilayer correlation simulations and showed that the columnar structure of the hollow interlayer can enhance the reflectivity. The reflectivity can be increased to about 81% for our proposed structure which is much better than the conventional 40-period Mo/Si multilayer which has the reflectivity about 75%.

Acknowledgements

We are grateful to the National Center for High-Performance Computing, Taiwan, for providing us with the computation time and using its facilities. This research was funded by National Science and Technology Council of Taiwan, grant number 111-2218-E-027-004 and 110-2221-E-002 -149 -MY2.

References

[1] E. Spiller, Appl Phys Lett 20(9), 365 (1972).
[2] Y.-M. Lee et al., Journal of Micro/Nanolithography, MEMS, and MOEMS 12(4), 043005 (2013).
[3] H. Hölscher et al., Optics Express, Vol. 21, Issue 12, pp. 14351-14361 21(12), 14351–14361 (2013).

Animation of dielectric metasurface 3D hologram

Tamaki Onozawa[1], Junpei Beppu[1], Masakazu Yamaguchi[1], Shunsuke Takahashi[1]
Satoshi Ikezawa[2] and Kentaro Iwami[1]

[1] Tokyo University of Agriculture and Technology, [2]Waseda University
E-mail: t-onozawa@st.go.tuat.ac.jp

1. Introduction

Three-dimensional (3D) metasurface holograms that enable natural 3D viewing with less fatigue are expected to be applied to 3D displays[1], AR/VR devices, and so on. In this study, we achieved a 3D holographic animation that can be observed with the naked eye without using a lens[2] as shown in Figure 1, by fabricating an array of large-area metasurface holograms. A movie that consists of 8 frames was successfully reproduced with a maximum speed of 2.8 fps.

2. Results

An array of metasurface holograms was fabricated using silicon nitride (SiN), which exhibits high transmittance in the visible light range. We calculated the phase distribution on the hologram surface to obtain a target image with a propagation distance of 30 mm. To avoid overlap between the projected and the conjugate images, the prism phase $\psi=2\pi x\sin\theta/\lambda$, where λ is the wavelength, x is the position in the x direction of each pixel, and θ is the bending angle, was overlayed on a hologram phase distribution. The phase delay and width of the nanopillars with an octagonal cross-section, a height of 1500 nm, and an array period of 340 nm were calculated using the finite element method. Based on these results, the width range from 50 nm to 170 nm was adopted to cover the full 2π phase range with the average transmittance of 97 %. A glass substrate on which SiN was sputter-deposited was used for fabrication. The substrate was coated with a resist, the structural pattern was drawn by EB lithography, and chromium was deposited by vacuum evaporation. The resist was removed by lift-off, the SiN was scraped by RIE, and the chromium was removed by wet etching. Fig. 2 shows the target images (a) and projected images (b) of the produced holograms. The projected images are reproduced with the target images with different inclinations in each frame, and can be observed without overlapping with the conjugate image due to the prism phase. The diffraction efficiency of each frame was highly efficient, ranging from 55% to 62%, and the propagation distance was 27 mm, which was almost as designed. Then the hologram was mounted on a biaxial automatic stage in the vertical and horizontal directions, and a program was created to operate all 8 frames alternately with the laser blinking. By looping the program, an operation of 2.8 fps was achieved. Improvement of the operation speed is expected by replacing the stage to the faster one.

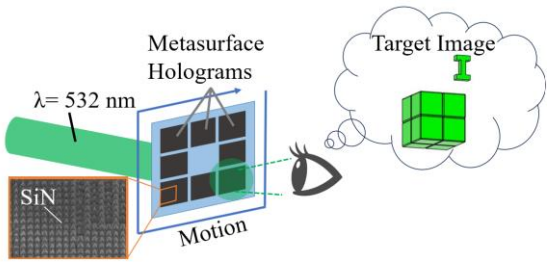

Fig. 1 Schematic diagram of metasurface holograms

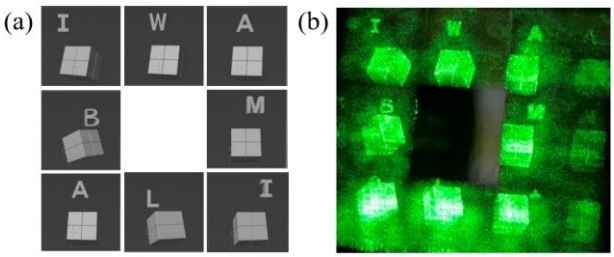

Fig. 2 All 8 target images (a) and the whole projected images of the metasurface hologram (b)

3. Conclusions

In this study, we designed, fabricated, and evaluated moving images of monochromatic 3D metasurface holograms that can be observed by the naked eye. In the future, we aim to increase the frame rate to more than 10 fps or higher by improving the stage movement speed, and to create full-color images by overlapping red and blue projection images.

Acknowledgements

This work was supported by JPS KAKENHI Grant Number 21H01781 and 22K04894, and “Advanced Research Infrastructure for Materials and Nanotechnology in Japan (ARIM)”. We would also like to thank Kyouji Matsushima, the developer of the "WaveField Library" used to calculate the phase distributions.

References

[1] Huang, Lingling, Zhang, Shuang and Zentgraf, Thomas. "Metasurface holography: from fundamentals to applications" Nanophotonics, vol. 7, no. 6, 2018, p. 1169, https://doi.org/10.1515/nanoph-2017-0118

[2] Gao, Hui et al. “Dynamic 3D meta-holography in visible range with large frame number and high frame rate.” Science advances vol. 6,28 eaba8595. 10 Jul. 2020, doi:10.1126/sciadv.aba8595.

Modified Coupled-Mode Theory on Fluorescent Surface Lattice Resonance

Kyoto Univ.[1], ◦Joshua Tin Yau Tse[1], Shunsuke Murai[1], Katsuhisa Tanaka[1]

E-mail: tse@dipole7.kuic.kyoto-u.ac.jp

Surface lattice resonance (SLR) is a plasmonic-photonic mode that is supported on nanoparticle arrays, originating from the coupling between in-plane diffraction modes and the localized surface plasmon resonance or Mie resonance on nanoparticles [1]. Previous works have shown that SLR is capable in significantly enhancing the light-matter interaction of fluorescent dye molecules and can enhance both the in-coupling efficiency as well as the directional out-coupling enhancement of the fluorescent emission [2]. SLR enhances the fluorescence absorption efficiency by confining the electromagnetic field into the vicinity of the nanoparticle array and inducing a strong light-matter interaction between the incident field and the fluorescent molecules [3]. SLR also enhances the spontaneous emission rate of fluorescent molecules through increased local density of state near the nanoparticle array, commonly known as the Purcell effect [4]. The nanoparticle array also controls the emission direction through diffraction.

In this work, we optimize the in-coupling efficiency to the fluorescent molecules by finding the conditions to maximize the absorption. The attention of this study was focused on nanoparticle arrays embedded in an index-matching layer with fluorescent dye at various concentration. We developed a modified coupled-mode theory that describes the interaction between the nanoparticle array and the fluorescent layer and analyzed the absorption behavior over a variety of configurations. Our analytical model predicts that the absorption of the SLR is mainly dependent on the absorptive and radiative decay rates of the SLR, with modulation from the non-resonant absorption.

The modified coupled mode theory is then extended to describe nanoparticle arrays that exhibit the lattice Kerker effect, which is characterized by the asymmetry between transmission and reflection response. The lattice Kerker effect is observed on nanoparticles that can support both electric dipole and magnetic dipole Mie resonances, which then forms the Electric(E)-SLR and Magnetic(M)-SLR respectively. By tuning the resonance of the E-SLR and M-SLR to the same resonant frequency, we observed extraordinary suppression in reflection and enhancement in absorption to near prefect absorption. We also discovered that the absorption of the nanoparticles and the fluorescent layer are controlled by the absorptive decay rate contributed by each component, and can be engineered to maximize the absorption to the fluorescent layer and the in-coupling efficiency towards fluorescence.

References

1. J. T. Y. Tse and H. C. Ong, Phys. Rev. B **104**, 125442 (2021).
2. S. Murai, K. Agata, and K. Tanaka, J. Appl. Phys. **129**, 183101 (2021).
3. Y. Jia, Y. Ren, X. Zhao, and F. Chen, Chin. Opt. Lett. **19**, 060013 (2021).
4. K. Guo, G. Lozano, M. A. Verschuuren, and J. Gómez Rivas, J. Appl. Phys. **118**, 073103 (2015).

Vanadium dioxide-enabled tunable metasurfaces

Zihang Zheng,[1] Kai Sun,[1,2] Yuxin Du,[1] Cornelis H. de Groot[1] & Xu Fang[1*]

[1]*School of Electronics and Computer Science, Univ. of Southampton, Southampton SO17 1BJ, UK*

[2]*School of Physics and Astronomy, Univ. of Southampton, Southampton SO17 1BJ, UK*

E-mail: x.fang@soton.ac.uk

Abstract: We numerically demonstrate output tuning in vanadium dioxide (VO_2) metasurfaces at 1550 nm, which is enabled by the phase transition of VO_2. The designs could be utilized in applications such as imaging and LiDAR sensing.

Optical metasurfaces are judiciously designed planar nanostructures that can manipulate the propagation of light waves. They have emerged as next-generation optical components with wide-ranging potential applications, where dynamic tuning is often a highly desired functionality. Several approaches have been established to achieve dynamic tuning, e.g., structural deformation [1] and coherent control [2]. This work belongs to the approach that utilizes changes in intrinsic material properties, and the tunable material used here is VO_2. VO_2 has a phase transition near room temperature, which is accompanied by a large change in its optical properties. Recent advancement in atomic layer deposition has also made deposition of high-quality VO_2 thin film more reliable and repeatable [3]. These factors make VO_2 an ideal material for tunable metasurfaces. In this work, we present several VO_2-based tunable metasurfaces and discuss their properties such as temperature dependence. The figure below shows an example device, where the metasurface functions as a light-focusing lens. The focus of the metalens changes with temperature across the phase transition.

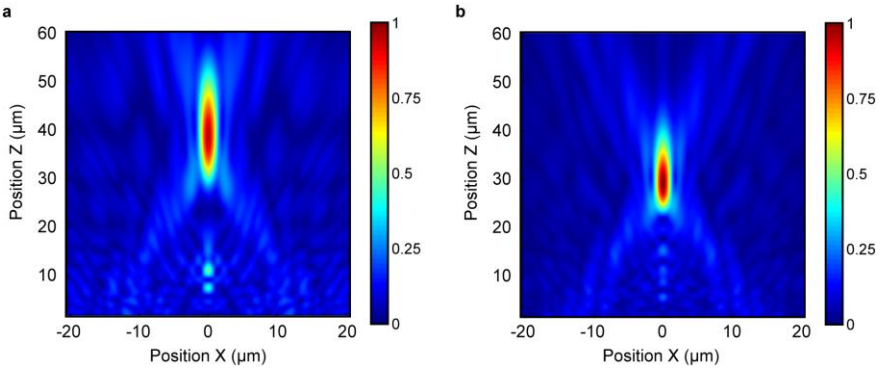

Figure 1. A tunable VO_2 metalens, showing a shift in focus with phase transition.

References: [1] H. S. Ee and R. Agarwal, “Tunable Metasurface and Flat Optical Zoom Lens on a Stretchable Substrate,” Nano Letters 16, 2818–2823 (2016). [2] F. He,Y. Feng, H. Pi, J. Yan, K. F. MacDonald, and X. Fang, “Coherently switching the focusing characteristics of all-dielectric metalenses,” Optics Express 30, 27683-27693 (2022). [3] K. Sun *et. al.*, “Room Temperature Phase Transition of W-Doped VO2 by Atomic Layer Deposition on 200 mm Si Wafers and Flexible Substrates,” Advanced Optical Materials 10() 2201326 (2022).

[19p-A602-1~15] 4.1 Plasmonics and Nanophotonics

Prabhat Verma(Osaka Univ.), Wakana Kubo(TUAT), Takuo Tanaka(RIKEN)

Tue. Sep 19, 2023 1:00 PM - 6:00 PM A602 (KJ Hall)

△：Presentation by Applicant for JSAP Young Scientists Presentation Award

▲：English Presentation

▼：Both of Above

No Mark：None of Above

▲[19p-A602-1] [JSAP-Optica Joint Symposia 2023 Invited Talk] Exploiting Photonic Topology in Semiconductor Nanophotonics

○Satoshi Iwamoto[1,2], Yasutomo Ota[3] （1.RCAST, Univ. of Tokyo, 2.IIS, Univ. of Tokyo, 3.Keio Univ.）

1:00 PM - 1:30 PM

▲[19p-A602-2] Resonant metaphotonics and metasurfaces

○Yuri Kivshar[1] （1.Australian National Univ.）

1:30 PM - 2:00 PM

▲[19p-A602-3] Transverse spin angular momentum of space-time surface plasmon polaritons

○Atsushi Kubo[1], Naoki Ichiji[1,2], Daigo Oue[3], Murat Yessenov[4], Kenneth L. Schepler[4], Ayman F. Abouraddy[4] （1.Univ. of Tsukuba, 2.The Univ. of Tokyo, 3.Univ. of Lisbon, 4.CREOL, Univ. of Central Florida）

2:00 PM - 2:15 PM

▲[19p-A602-4] Design and Characterization of High Aspect Ratio, Double Insulator Plasmonic Nanostructures for Gas Sensing Applications

○(PC)Maria Balois[1], Cheng-Hung Chu[2], Takeshi Yamaguchi[1], Takuo Tanaka[1,3,4] （1.Photon Team, RIKEN, 2.National Taiwan Univ, 3.Mets. Lab, RIKEN, 4.Tokushima Univ.）

2:15 PM - 2:30 PM

▼[19p-A602-5] Infrared Plasmonic Metasurfaces with Double Resonances for SEIRA Platforms

○(D)Tang Dang[1], Shuting Ma[1], Jiaqi Yang[1], Hitoshi Tabata[1], Hiroaki Matsui[1] （1.Univ. of Tokyo）

2:30 PM - 2:45 PM

▲[19p-A602-6] Surface Phonon Resonances in Circular Cavities on the Surface of Bioactive Hydroxyapatite for Biosensing Platforms

○(DC)Shuting Ma[1], Tang Dang[1], Hidehiko Yoda[2], Yoshita Sato[1], Hitoshi Tabata[1], Hiroaki Matsui[1] （1.The Univ. of Tokyo, 2.Utsunomiya Univ.）

2:45 PM - 3:00 PM

▼[19p-A602-7] Design, Fabrication and Evaluation of the Metasurface Optical Gas Sensor Using Deep Ultraviolet Plasmon Resonance

○(B)Mayu Sekiguchi[1], Ryo Matsuda[1], Yuji Ogawa[2], Kenichiro Matsushita[2], Satoshi Ikezawa[3], Kentaro Iwami[1] （1.Tokyo Univ. of Agriculture and Technology, 2.Meidensha Co., 3.Waseda Univ.）

3:00 PM - 3:15 PM

▲[19p-A602-8] [JSAP-Optica Joint Symposia 2023 Invited Talk] Nanoplasmonics for high-frequency rectification

○Remo Proietti Zaccaria[1] （1.Italian Institute of Technology, Genova）

3:30 PM - 4:00 PM

▲[19p-A602-9] [JSAP-Optica Joint Symposia 2023 Invited Talk] Thermal transport by surface phonon polaritons in SiN nanofilms

○Masahiro Nomura[1] （1.IIS, Univ. of Tokyo）

4:00 PM - 4:30 PM

▲[19p-A602-10] Thermal conductivity measurement of transparent thin film by photothermal heating with continuous wave laser

○(D)Nicholaus Kevin Tanjaya[1,2], Satoshi Ishii[1,2] （1.NIMS, 2.Univ. of Tsukuba）

4:30 PM - 4:45 PM

▼[19p-A602-11] Nanocavity induced by atomically thin transition metal dichalcogenide in photonic crystal waveguide

○(PC)CheeFai Fong[1], Daiki Yamashita[2,3], Nan Fang[1], Shun Fujii[2,4], Yih-Ren Chang[1], Takashi Taniguchi[5], Kenji Watanabe[6], Yuichiro K. Kato[1,2] （1.CPR, RIKEN, 2.RAP, RIKEN, 3.AIST, 4.Keio University, 5.MANA, NIMS, 6.NIMS）

4:45 PM - 5:00 PM

▲[19p-A602-12] Fabrication of gold nanobridges between gold nanoparticles by localized light

○(PC)Yuki Takeuchi[1,2], Nobuyuki Takeyasu[3], Takuo Tanaka[1,4] （1.Riken, 2.JSPS Research Fellow, 3.Okayama Univ., 4.Tokushima Univ.）

5:00 PM - 5:15 PM

▲[19p-A602-13] Helicity Preserving Scattering by Mie Resonant Silicon Nanoparticles

○HIROSHI SUGIMOTO[1], HIDEMASA NEGORO[1], MINORU FUJII[1] （1.Kobe Univ.）

5:15 PM - 5:30 PM

▲[19p-A602-14] Gallium Phosphide Nanoparticles for Low-Loss Nanoantennas in Visible Range

○Daisuke Shima[1], Hiroshi Sugimoto[1], Artyom Assadillayev[2], Soeren Raza[2], Minoru Fujii[1] （1.Kobe Univ., 2.Technical Univ. of Denmark）

5:30 PM - 5:45 PM

▲[19p-A602-15] Nanoparticle Film based on Mechanoplasmonic Sensors for Wearable Strain Applications of Human-Motion Monitoring

○Hiroaki Matsui[1], Akira Momose[2], Hidehiko Yoda[3], Aki Fujita[4] （1.The Univ. of Tokyo, 2.KISTEC, 3.Utsunomiya Univ., 4.Sci. &Technol. Inst. Co.）

5:45 PM - 6:00 PM

Exploiting Photonic Topology in Semiconductor Nanophotonics

Satoshi Iwamoto[1, 2] and Yasutomo Ota [3]

[1] RCAST, [2]IIS, The University of Tokyo, [3] Keio University
E-mail: iwamoto@iis.u-tokyo.acjp

1. Introduction

Research on optics from the viewpoint of topology has begun early 19th century [1]. Recently, the concept of topology has opened up new fields not only in condensed matter physics but also optics and photonics. One of them is topological photonics [2,3], which explores and utilizes the topological properties of light in momentum space. Topologically protected edge states of light appear at the boundary of two optical structures having distinct topological properties in their band structures. The topological edge states, as for the electronic counterparts, can robustly guide light even under the presence of structural disorders including sharp bends of the interface. Besides the physical interests, this unique feature suggesting the potential for novel photonics devices robust against fabrication imperfections/structural disorders has been attracting researchers in the field of nanophotonics.

Semiconductor-based photonic nanostructures are one of the widely used photonic structures for investigating on-chip topological photonics because of their compatibility with the present integrated photonic technologies [4,5]. We have demonstrated, for the first time, a topological nanocavity laser [6] and photonic nanocavity based on a topological corner state [7] using semiconductor photonic crystals (PhCs). In this presentation, starting with a brief introduction to topological photonics, we will discuss our recent progress on topological photonics based on semiconductor nanophotonic platforms.

2. Topological photonics based on semiconductor photonic nanostructures.

Valley photonic crystals (VPhCs) are one of the PhC structures which can host photonic topological edge states. We have proposed and experimentally demonstrated a topological slow-light waveguide based on semiconductor VPhCs [8,9]. The topological slow-light waveguide can reduce the bending loss, which is significant in conventional slow-light waveguides. VPhC topological waveguides have been applied to a ring-resonator laser [10] and integrated quantum-dot single photon sources [11]. In VPhC waveguides, triangular holes are predominantly used. This makes EB lithography common in fabrication. We have recently developed the technology for fabricating VPhC waveguides with CMOS-compatible processes as for other silicon photonic devices [12].

A big challenge in topological nanophotonics is to realize topological PhCs with broken time-reversal symmetry at telecom wavelengths. We have theoretically shown that the application of the epsilon-near-zero effect can be a possible route toward the goal [13]. In addition to these results exploiting photonic topology, if time allows, a study generating photonic topology using semiconductor photonic nanostructures [14] will be also introduced.

Acknowledgements

We would like to express sincere thanks to all the collaborators who are contributing to the work discussed here. The work here was supported by JST-CREST (JPMJCR19T1), JSPS KAKENHI (17H06138, 19K05300, 19K21959, 22H01994, and 22H00298), the Nippon Sheet Glass Foundation for Materials Science and Engineering, and Asahi Glass Foundation.

References

[1] M. V. Berry: “OPTICAL VORTICULTURE,” Topology in Ordered Phases, eds. S. Tanda, T. Matsuyama, M. Oda, Y, Asano, and K. Yakubo (World Scientific, Singapore, 2004).
[2] L. Lu, J. D. Joannopoulos and M. Soljačić: Nat. Photon. **8**, 821 (2014).
[3] T. Ozawa, H. M. Price, A. Amo, N. Goldman, M. Hafezi, L. Lu, M. C. Rechtsman, D. Schuster, J. Simon, O. Zilberberg, and I. Carusotto: Rev. Mod. Phys. **91**, 015006 (2019).
[4] S. Iwamoto, Y. Ota, and Y. Arakawa, Opt. Mater. Express **11**, 319 (2020).
[5] Y. Ota, K. Takata, T. Ozawa, A. Amo, Z. Jia, B. Kante, M. Notomi, Y. Arakawa, and S. Iwamoto, Nanophotonics **9**, 547 (2020).
[6] Y. Ota, R. Katsumi, K. Watanabe, S. Iwamoto, and Y. Arakawa, Commun. Phys. **1**, 86 (2018).
[7] Y. Ota, F. Liu, R. Katsumi, K. Watanabe, K. Wakabayashi, Y. Arakawa, and S. Iwamoto, Optica **6**, 786 (2019).
[8] H. Yoshimi, T. Yamaguchi, Y. Ota, Y. Arakawa, and S. Iwamoto, Opt. Lett. **45**, 2648 (2020).
[9] H. Yoshimi, T. Yamaguchi, R. Katsumi, Y. Ota, Y. Arakawa, and S. Iwamoto, Opt. Express **29**, 13441 (2021).
[10] R. Miyazaki, K. Kuruma, H. Yoshimi, R. Katsumi, T. Yamaguchi, Y. Ota, Y. Arakawa and S. Iwamoto, 2021 SSDM, E-5-04 (2021).
[11] K. Kuruma, H. Yoshimi, Y. Ota, R. Katsumi, M. Kakuda, Y. Arakawa and S. Iwamoto, Laser Photon. Rev., **16**, 2200077 (2022).
[12] T. Yamaguchi, H. Yoshimi, M. Seki, M. Ohtsuka, N. Yokoyama, Y. Ota, M. Okano, and S. Iwamoto, arXiv:2305.07747 (2023).
[13] T. Liu, N. Kobayashi, K. Ikeda, Y. Ota, and S. Iwamoto, ACS Photon. **9**, 1621 (2022).
[14] W. Lin, Y. Ota, Y. Arakawa and S. Iwamoto, Phys. Rev. Research **3**, 023055 (2021).

Resonant metaphotonics and metasurfaces

Yuri Kivshar*
Nonlinear Physics Center, Department of Fundamental and Theoretical Physics, Research School of Physics, Australian National University, Canberra ACT 2601, Australia
E-mail: yuri.kivshar@anu.edu.au

Abstract: We review the recent advances in *nonlinear metaphotonics* of nanoparticles and metasurfaces empowered by optical resonances. We demonstrate a giant enhancement of the second-harmonic signal generated from silicon metasurfaces at guided-mode lattice resonances and quasi-bound states in the continuum.

In metaphotonics, resonances play a pivotal role in enhancing nonlinear effects. Optical properties of metaphotonic structures, whether composed of individual nanoparticles or metasurfaces, are determined by the geometry of their units (meta-atoms) and material properties. Metallic nanostructures can host a variety of resonances, ranging from local surface plasmon resonances (LSPR) in individual nanoantennas to nonlocal lattice modes in plasmonic metasurfaces.

Compared to low efficiencies and losses in metallic structures, dielectric metasurfaces and nanoantennas provide an attractive low-loss platform for nonlinear metaphotonics. The main building blocks of dielectric metastructures are dielectric nanoparticles supporting vectorial Mie resonances. Dielectric nanostructured surfaces can also host optical bound states in the continuum (BICs), observed as quasi-BICs, with dramatically large quality factors (Q factors) from several hundred to tens of thousands. Common types of resonances in plasmonic and dielectric structures are shown in Fig. 1.

For nonlinear nanostructures, the phase matching is not applicable, and the frequency conversion efficiency is defined by the resonant characteristics such as coupling efficiency and mode Q factor. It was demonstrated recently that quasi-BICs with very large Q factors can boost the generation of the third harmonics by several orders of magnitude enabling ultrafast self-action effects in the non-perturbative regime. Also it was shown recently that silicon metasurfaces hosting quasi-BICs in the mid-IR wavelength range produce the generation of up to 11-th harmonics, as well as that individual AlGaAs nanoresonators can generate higher-order odd harmonics.

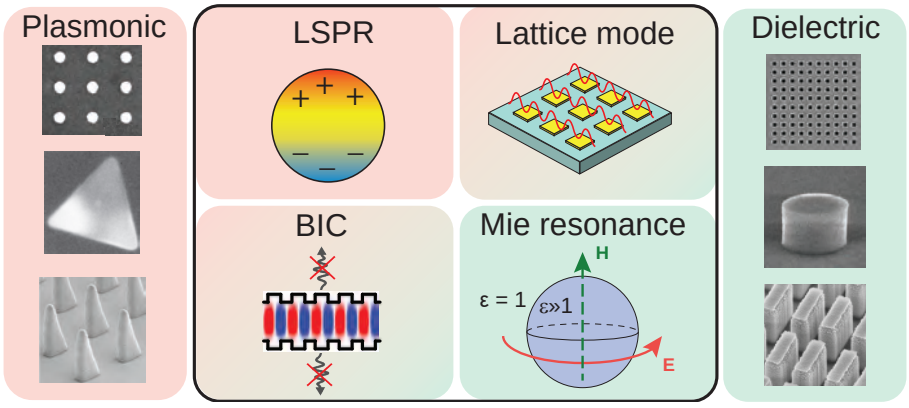

Fig. 1. **Optical resonances in metaphotonics.** Left: SEM images of plasmonic metasurfaces with lattice guided mode, LSPR, and BIC resonances. Middle: the main types of resonances in plasmonic (red), dielectric (green), and hybrid (gradient) metastructures. Right: SEM images of dielectric metastructures supporting guided-mode lattice, Mie, and BIC resonances.

As a specific example, here we demonstrate a giant enhancement of the second-harmonic generation (SHG) from resonant silicon metasurfaces. Our metasurface is composed of a square lattice of asymmetric meta-molecules consisting of bar dimers with a different width. We observe experimentally SHG and third-harmonic generation (THG) with the resonant enhancement of SHG by three orders of magnitude.

Transverse spin angular momentum of space-time surface plasmon polaritons

◦A. Kubo[1], N. Ichiji[1,2], D. Oue[3], M. Yessenov[4], K. L. Schepler[4], A. F. Abouraddy[4]

Univ. of Tsukuba [1], IIS, The Univ. of Tokyo[2], Univ. of Lisbon[3], CREOL, Univ. of Central Florida[4],

E-mail: kubo.atsushi.ka@u.tsukuba.ac.jp

Spatially structured electromagnetic fields such as evanescent waves and surface plasmon polaritons (SPPs) possess transverse spin angular momentum (*t*-SAM) in the direction perpendicular to the axis of propagation [1]. Moreover, when the SPP has a two-dimensionally structured profile at the confined interface, the *t*-SAM possesses both the in-plane (*t*-SAM∥) and the out-of-plane (*t*-SAM⊥) components, indicating that the SPP can have a three-dimensional arrangement of spin textures and thus a finite surface area on the Poincaré polarization vector sphere.

In this work, we numerical calculated the SAM distribution of the space-time surface plasmon polariton (ST-SPP) wave packet (WP), a plasmonic bullet that propagates at an arbitrary group velocity while maintaining its spatial distribution [2,3]. ST-SPP WPs with complex field structure and energy flow density distribution were found to propagate with accompanying three-dimensional spin texture and finite topological charge density. We handled a type of ST-SPP with a propagation-invariance. The spectral support domain of the ST-SPP WP was defined by an intersection of a SPP light cone with a spectral plane $\Omega = (k_y - k_0')c\tan\theta$, which is parallel to the k_x-axis and makes an angle θ with the k_y-axis (Fig.1), where k_0' is the SPP wavenumber at the carrier frequency ω_0, and $\Omega = \omega - \omega_0$. The k_y-axis was taken along the axial direction of the wave propagation. We assumed $\omega_0/2\pi = 375$ THz (~800 nm wavelength light) and the spectral width of the ST-SPP equal to a light pulse with the duration of 100 fs. The SAM of WPs, $\boldsymbol{S} = \frac{1}{4\omega}\mathrm{Im}(\varepsilon\boldsymbol{E}^* \times \boldsymbol{E} + \varepsilon\mu\boldsymbol{H}^* \times \boldsymbol{H})$ was calculated from the complex electromagnetic field of the ST-SPP. In addition, L-line singularity map $|\boldsymbol{S}|/S_z$ was calculated to evaluate where the local polarization becomes linear.

Figure 2 shows maps of the L-line singularity (Fig.2a), and *t*-SAM⊥ calculated for the ST-SPP WP with the group velocity $v_g = c$ (c: speed of light in vacuum) at the time $t = 0$ (Fig.2b) and 334 fs (Fig.2c), respectively. The shape of the L-line is characterized by a series of split rings that appear in the center of the ST-SPP WP. These split rings frame the out-of-plane SAM component of the ST-SPP. Interestingly, the spatial distribution of the *t*-SAM⊥ and the L-line singularity were maintained after the WP propagated to 100 μm, which amounted to more than twice the attenuation length of SPP (~45 μm). This result suggests the ST-SPP WP can provide robust and group-velocity tunable transportations of three-dimensional spin textures on material surfaces [4].

[1] K. Y. Bliokh, F. Nori, *Phys. Rev. A* **85**, 061801 (2012). [2] H. E. Kondakci, A. F. Abouraddy, *Nat. Photonics*, **11**, 733 (2017). [3] N. Ichiji, H. Kikuchi, M. Yessenov, K. L. Schepler, A. F. Abouraddy, A. Kubo, *ACS Photononics*, **10**, 374 (2023). [4] N. Ichiji, D. Oue, M. Yessenov, K. L. Schepler, A. F. Abouraddy, A. Kubo, *Phys. Rev. A* (*in printing, arXiv: 2301.12654*).

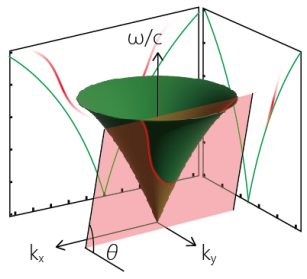

Fig.1 Spectral support domain (red line) of the ST-SPP defined as the intersection of the SPP light-cone (green cone) and the spectral plane (red plane).

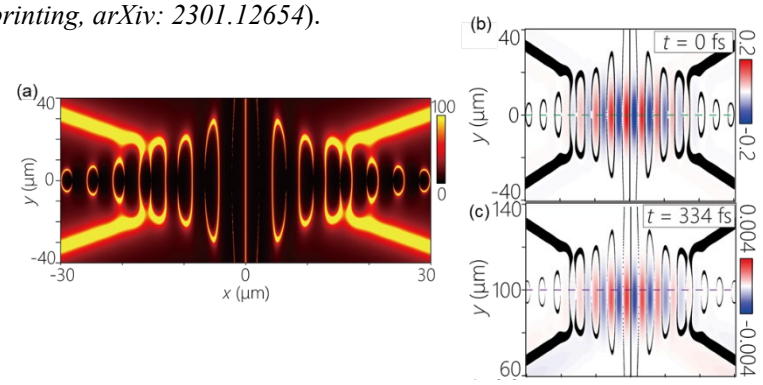

Fig.2 (a) L-line singularity map of the ST-SPP WP. (b,c) spatial distributions of the *t*-SAM⊥ of the ST-SPP WP at the time $t = 0$ (b) and 334 fs (c), respectively, plotted with the L-line map.

Design and Characterization of High Aspect Ratio, Double Insulator Plasmonic Nanostructures for Gas Sensing Applications

Maria Vanessa Balois-Oguchi[1], Cheng-Hung Chu[2], Takeshi Yamaguchi[1], and Takuo Tanaka[1,3,4]

[1] Innovative Photon Manipulation Research Team, RIKEN Center for Advanced Photonics, [2] Institute of Medical Device and Imaging, National Taiwan University, [3] Metamaterials Laboratory, RIKEN Cluster for Pioneering Research, [4] Institute of Post-LED Photonics, Tokushima University
E-mail: mariavanessa.balois@riken.jp

1. Introduction

Optical gas sensors for detecting and monitoring harmful gases is of great interest in medicine, industry and environment sectors [1,2]. With the rapid miniaturization of technology, there is an increasing demand to develop more compact, robust and sensitive gas sensors. To address this demand, plasmonic nanostructures of various designs have been implemented to detect gas molecules through techniques such as surface-enhanced infrared absorption. Our group has developed a plasmonic metamaterial infrared absorber that utilizes vertical metal-insulator-metal channel-type (c-MIM) nanostructures [3], wherein the resonance frequency of the c-MIM couples with the vibration of the target molecule to produce Fano resonance. Using this c-MIM, our group previously demonstrated the detection of butane and carbon dioxide gases. However, there were two main concerns: (1) can the molecule access the hotspots in the deeper parts of the c-MIM, and (2) can we improve the stability of the channel structure. We address these concerns through the use of a double insulator plasmonic nanostructure, that combines SiO_2 and air to engineer the position and intensity of the electromagnetic field generated at the gap between the two Au vertical walls. The c-MIM is supported by a Si grating for increased stability. In this work, we study the geometrical impact of our proposed design on frequency selectivity, electromagnetic field distribution and absorption tunability experimentally and through numerical simulations [4].

2. Methods

Finite-difference time-domain (FDTD) simulations were conducted to determine the expected resonance frequency and field distribution of the structure. The c-MIMs were fabricated using electron beam lithography for pattern drawing, electron beam evaporation for the Au and SiO_2 deposition, and inductive coupled plasma – reactive ion etching (ICP-RIE) for creating the air gap between the Au vertical walls. An energy dispersive X-ray spectrometer (EDX) combined with a scanning electron microscope (SEM) was used to determine the material distribution in the structure. A Fourier transform infrared (FTIR) spectrometer equipped with an optical microscope was used for optical characterization.

3. Results and Discussion

Figure 1a shows the fabricated high aspect ratio channel-type plasmonic structure with the inner and the outer Au walls having an aspect ratio of 18.3 and 16.7, respectively. Both Au walls have a width of 60 nm. A gap that is 30 nm in width is between the two Au walls. This gap consists of both an upper air gap and a lower SiO2 layer whose height varies with etching time during ICP-RIE etching. Through FDTD simulations, we determined that the overall height of the Au inner walls dictates the initial resonance frequency of the structure, while the filling ratio of the air/SiO_2 gap can be varied to further tune the resonance frequency. This is experimentally shown from the FTIR spectra in Figure 1b, wherein different etching times ranging from 6 to 8 min were used. From the simulations, we also found that this filling ratio can tune the distribution and the intensity of the enhanced electromagnetic field at the gap between the Au walls. An optimal filling ratio exists to obtain maximum enhancement of the electromagnetic field.

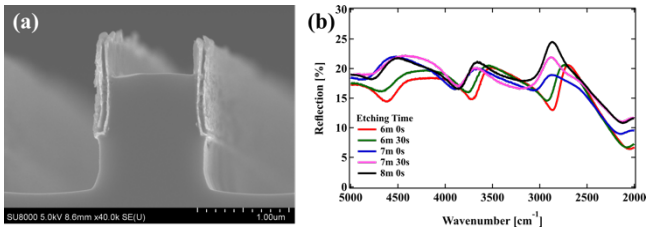

Figure 1. (a) SEM image of c-MIM. **(b)** FTIR reflection spectra of c-MIM structures whose air/SiO_2 filling ratios are varied using different ICP-RIE etching times.

4. Conclusions

We introduced the use of a double insulator c-MIM structure wherein the filling ratio of the air and the SiO_2 at the gap between the Au walls can tune the resonance frequency of the c-MIM and efficiently guide the target molecule to the enhanced electromagnetic field at the gap. Our proposed design will be useful in creating highly sensitive and robust c-MIM-based gas sensors.

References

[1] Alexander Lochbaum, et. al, Nano Lett. **20** (2020) 4169-4176.
[2] Ross Stanley, Nat. Photonics **6** (2012) 409-411.
[3] Dong-Sheng Su, ACS Sens. **4** (2019) 2900-2907.
[4] Maria Vanessa Balois-Oguchi, et. al, *in preparation*.

Infrared Plasmonic Metasurfaces with Double Resonances for SEIRA Platforms

Tang Dang[1], Shuting Ma [1], Jiaqi Yang [1], Hitoshi Tabata [1], and Hiroaki Matsui *[1]
The University of Tokyo
E-mail: dangtang@g.ecc.u-tokyo.ac.jp and *hiroaki@ee.t.u-tokyo.ac.jp

1. Introduction

Recent progress in the design and manufacturing of metal nanostructures has opened up new possibilities for generating and controlling localized electromagnetic fields and adjustable spectral resonances. Notably, the recent introduction of multispectral plasmonic nanoantennas has demonstrated significant potential for various spectroscopic applications, such as on-chip plasmon sensing of multiple analytes, as well as simultaneous detection of fluorescence and Raman signals in both the visible and infrared (IR) spectral domains. Surface-enhanced infrared absorptions (SEIRAs) can identify molecules of different chemical nature by matching the plasmonic resonances with the molecular-vibrational peaks. However, the metasurfaces with a single resonance show a narrow resonance peak, which cannot detect excitation wavelengths for a wide range of molecular vibrations. Therefore, it is required to simultaneously measure different molecular vibrations. Our presentation introduces IR metasurfaces with dual resonances consisting of two different sizes, enabling comprehensive measurements of molecular vibrations beyond conventional SEIRA devices with single resonance.

2. Results and Discussion

In our study, we primarily focused on the structure (5P) of the upper right part of Figure 1(a), which is composed of periodic large and small dot structures, as observed using scanning electron microscopy (SEM). Figure 1(a) clearly shows that the 5P structure exhibits two distinct reflection peaks, which was close to the reflection peaks derived from each sample with the large and small dot structures, respectively. We performed FDTD simulations of a sample of the 5P structure placed in air in Figure 1(b). The electric fields of the 5P structure at lower wavenumbers was similar to that of small dot sample. Conversely, at higher wavenumbers, the electric field of the 5P structure was matched with that of the large dot sample. To validate the SEIRA properties of the 5p structure, we spin-coated poly methyl methacrylate (PMMA) with varying thicknesses on the 5P structure surface. Figure 1(c) shows reflectance spectra of the 5P structure after coating PMMA layers. Notably, distinct absorption peaks could be observed at around 3000 cm^{-1} and 1750 cm^{-1}. Herein, the C=O stretching vibration

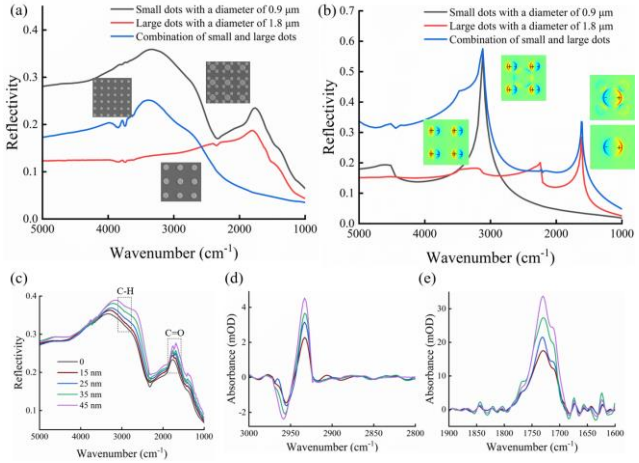

Figure 1. (a) Experimental and (b) theoretical reflectance spectra of Au dot structures with different patterns. Blue and red lines are the spectra of dot structures consisting of a single size. A black line is the spectra of the dot structure with two sizes. (c) Reflectance spectra after coating PMMA layers with different thicknesses. (d) Differential spectra of $CH_2(CH_3)$ and (e) C=O related vibrations as a function of PMMA layer thickness.

exhibited a distorted profile deviating from the normal Lorentzian shape. The peak distortion is related to an asymmetric Fano profile, resulting from the strong interaction between the molecular dipole and plasmon modes. Moreover, we also found a red-shift of resonant peaks with an increase in PMMA layer thickness due to the higher refractive index (n = 1.49) of PMMA than that of air (n = 1). It is not easy to compare directly molecular-vibrational absorptions between the bare and PMMA-coated samples due to the red-shift of resonant peaks. Therefore, we initially performed a polynomial fitting on the PMMA spin-coated sample, and utilized the following relation: $A = -\log(R\_PMMA/R\_Fitting)$ in order to clarify the molecular-vibrational absorptions. Figures 1(d) and 1(e) present calculation results of the molecular-vibrational absorptions of CH_2 (CH_3) bond and C=O bond, respectively. It was evident that the absorptions of the C-H bond and C=O bond became more pronounced as the PMMA thickness increased. Additionally, the C=O bond provided stronger absorptions compared to the $CH_2(CH_3)$ bond. This difference was due to that the SEIRA enhancement was inversely proportional to the third power of the resonance frequency. As a consequence, the resonant peak at 1750 cm^{-1} was well described as compared with that at around 2800 cm^{-1} related to the $CH_2(CH_3)$ band.

Surface Phonon Resonances in Circular Cavities on the Surface of Bioactive Hydroxyapatite for Biosensing Platforms

Shuting Ma [1], Tang Dang [1], Hidehiko Yoda [2], Yoshita Sato [1], Hitoshi Tabata [1] and Hiroaki Matsui [1]

[1] The University of Tokyo, [2] Utsunomiya University
E-mail: ma-shuting626@g.ecc.u-tokyo.ac.jp & hiroaki@ee.t.u-tokyo.ac.jp

1. Background, Contents and Purpose

Surface phonon resonance (SPhR) is a phenomenon that occurs when the collective oscillations of atomic lattice are excited by external incident fields from the mid-infrared (MIR) range at the surface of a polar dielectric [1]. SPhR-related phenomenon in the IR range is connected to surface-enhanced infrared absorption (SEIRA) toward spectroscopic measurements through the coupling between the molecular vibrations and SPhRs, leading to biosensing devices with label-free molecular recognition for monitoring biological interactions [2]. The SPhRs of some classical phononic materials such as SiC, h-BN, MoO_3, and Al_2O_3 have higher Q-factors than those of plasmonic materials, however, the sensing of these materials is limited to the target molecules. In contrast, this research focused on a well-known bioactive material, hydroxyapatite (HAp), which actively interacts with the surrounding liquid environment resulting in the change of surface status. The environment-sensitive nature of surface phonons makes it possible to function as active optical probes, defining as “active SEIRA”. In this work, Au microhole arrays were formed on HAp substrates to produce SPhRs confined in circular cavities. SPhRs in the holes with different sizes were examined by IR-ellipsometry under *s*- and *p*-polarization light at changing incident angles. The final purpose is to create HAp as a novel biosensing platform based on active-SEIRA for detecting the chemical change of host surface dependent on environment (pH) and examining the affinity to polypeptides.

2. Results, Conclusions and Prospects

Figure 1(a) shows the optical images of Au microhole structures with different hole sizes (D = 4 ~ 7 μm) in periodic 2D square arrays. As shown in Figure 1(b), in the case of D below 7 μm, new dips appeared at around 1098 cm^{-1} in the Reststrahlen band ($\omega_{TO} < \omega < \omega_{LO}$) as compared with the spectra of poly-HAp substrate. These new dips were identified to be surface phonon polariton wave occurring at the air/HAp interface in the circular cavities defined by the walls of the Au holes. These surface phonon modes, related to the PO_4^{3-} vibrations, were only excited under the *p*-polarization light. Additionally, we also observed wide resonant dips at wavenumbers larger than ω_{LO} , which were attributed to the circular slot antenna resonance with cavity modes. The increase of the hole size led to a red-shift of the resonance dip. Before, SPhRs-related studies were discussed on polar dielectrics such as SiC, GaN and BN. This is the first report to show SPhRs on the surface of ceramic HAp with higher Q-factors than many previous phononic materials. Figure 1(c) contains the reflectance spectrum of the sample with D = 5 μm under oblique incidence. The resonances became stronger as the incident angle increased and the Q-factor could reach 162 at θ = 50°. The obtained results gave a strong proof that HAp had the potential to be one of candidates as phononic materials and SEIRA platforms. Further, we’ll treat HAp by pH-controlled Tris-buffer solutions for clarifying the relationship between surface changes (charges, ions) and SPhRs. Moreover, we plan to examine the affinity of polypeptides to host surface based on the active-SEIRA. In this case, we explore an effective way for screening high binding peptides to HAp with no need for complex and time-consuming animal testing.

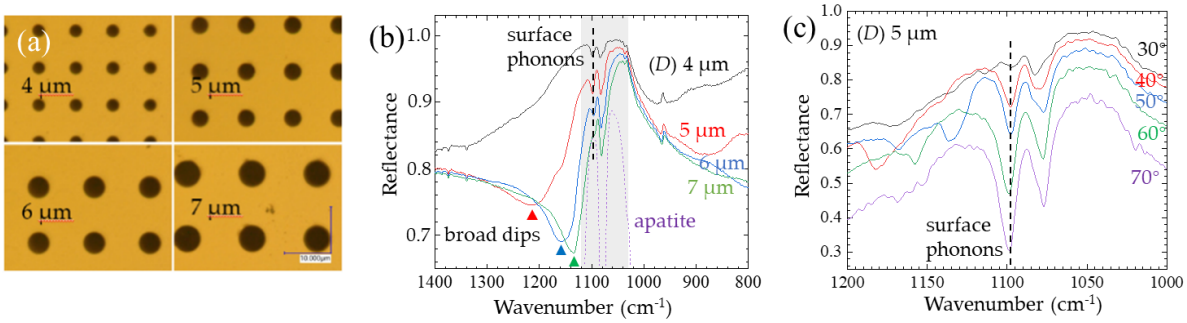

Figure. 1. (a) Optical images of the microhole arrays (D = 4 ~ 7 μm) in Au film on HAp substrate. (b) Reflectance spectrum of Au microhole films on HAp. The purple dotted line is the reflectance spectra of HAp substrate. The grey column indicates the Reststrahlen band (1030 ~ 1120 cm^{-1}). (c) Reflectance spectrum of Au microhole film (D = 5 μm) on HAp substrate at different incident angles.

References

[1] Joshua D. Caldwell, et al. Nanophotonics. **4** (2015) 44-68. [2] Frank Neubrech, et al. Chem. Rev. **117** (2017) 5110-5145.

Design, Fabrication and Evaluation of the Metasurface Optical Gas Sensor Using Deep Ultraviolet Plasmon Resonance

Mayu Sekiguchi[1], Ryo Matsuda[2], Yuji Ogawa[2], Kenichiro Matsushita[2], Satoshi Ikezawa[3], and Kentaro Iwami[1]

[1] Tokyo University of Agriculture and Technology, [2] Meidensha Corporation, [3] Waseda University
E-mail: m-sekiguchi@st.go.tuat.ac.jp

1. Introduction

Ozone and ammonia gases detections are in strong demand among high-voltage equipment to avoid nitric acid corrosion. An optical gas sensor has realized a low detectable concentration of 20 ppm butane with the aid of plasmon resonance at the infrared wavelength.[1] As ozone and ammonia have large absorption cross-sections at the deep-ultraviolet region, the achievement of low-concentration detection is expected. In this study, we designed, fabricated, and evaluated an optical gas sensor using deep-ultraviolet plasmon resonance.

2. Results

Figure 1 shows a schematic drawing of the proposed plasmonic device for the gas sensor. A metasurface that consists of vertically-aligned aluminum walls periodically arrayed in a 200 μm square.[2] Figure 2 shows the simulated transmittance spectra of the proposed device calculated using COMSOL Multiphysics 6.0 (COMSOL Inc., USA). Figure 2 shows that the absorption peaks split back and forth as the incident light angle θ increases. θ is the angle from the z-axis in the y-z plane of incident light in Figure 1. The sensor was fabricated on a 2-cm-square silica glass substrate through in six steps: Si sputtering, electron beam lithography, Si etching, aluminum oblique deposition, aluminum etching, and Si etching. Electron microscopy after oblique deposition of aluminum on Si pillars showed that the widths of the structures were about 20 to 40 nm larger than the designed values. This indicates that excessive aluminum was deposited on the sidewalls of the Si pillars.

Figure 3 shows the measured transmittance spectra of the fabricated device with varying incident angles θ. As shown in Figure 3, the absorption dips are obtained for every plot at 230-240 nm. It is considered that these dips are due to the incident angle dependence of the plasmon resonance, as shown in Figure 2. However, the shapes and wavelength range of the dips in Figure 3 are different from in Figure 2. we considered that the difference was caused by incomplete manufacturing.

3. Conclusions

We designed, fabricated, and evaluated a gas sensor element using deep-ultraviolet plasmon resonance. Next, the processing conditions for oblique deposition will be optimized to improve the structural dimensions since excessive aluminum was deposited in order to proceed to the gases detection experiments.

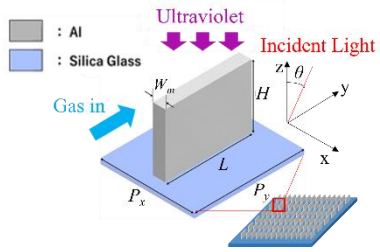

Fig. 1 The proposed device

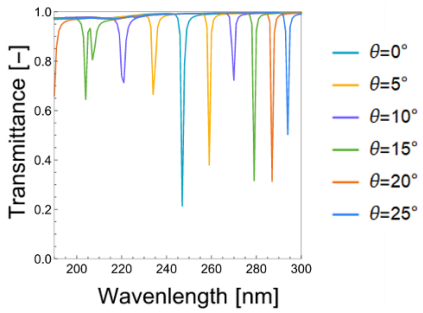

Fig. 2 Simulation results of transmittance at different incident angles

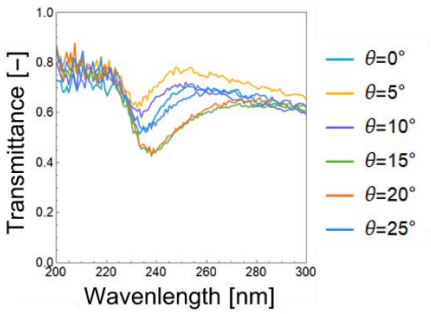

Fig. 3 Spectral analysis at different incident angles

Acknowledgements

This research is supported in part by “Advanced Research Infrastructure for Materials and Nanotechnology in Japan (ARIM)” of the Ministry of Education, Culture, Sports, Science and Technology (MEXT), in part by JST Adaptable and Seamless Technology transfer Program through Target driven R&D (A STEP) Grant Number JPMJTM22BU.

References

[1] D. S. Su, D. P. Tsai, T. J. Yen, and T. Tanaka, “Ultrasensitive and Selective Gas Sensor Based on a Channel Plasmonic Structure with an Enormous Hot Spot Region,” ACS Sensors, vol. 4, no. 11, pp. 2900–2907 (2019).

[2] R. Watanabe, R. Matsuda, S. Ikezawa, K. Iwami, ”Development of ozone and ammonia gas sensor using ultraviolet plasmon resonance,” The 39th Symposium on Sensors, Micromachines and Applied Systems, 15P2-P-26 (2022) .

3:30 PM - 4:00 PM (Tue. Sep 19, 2023 1:00 PM - 6:00 PM A602)

▲[19p-A602-8] [JSAP-Optica Joint Symposia 2023 Invited Talk] Nanoplasmonics for high-frequency rectification

○Remo Proietti Zaccaria[1] (1.Italian Institute of Technology, Genova)

Keywords: nanoplasmonics

Thermal transport by surface phonon polaritons in SiN nanofilms

Masahiro Nomura
IIS, The Univ. of Tokyo
E-mail: nomura@iis.u-tokyo.ac.jp

Thermal conduction becomes less efficient as structures scale down into submicron sizes due to the predominant phonon-boundary scattering that hinders phonons more efficiently than Umklapp scattering. Recent studies indicated that this thermal performance reduction could be avoided by using surface phonon-polaritons (SPhPs), which are evanescent electromagnetic waves generated by the hybridization of optical phonons and photons. These waves propagate along the surface of polar dielectric materials and could be heat carriers capable of remarkably enhancing the thermal performance of micro- and nanoscale devices. We experimentally observe the dominant heat contribution of SPhPs in SiN nanofilms

Figure 1 shows the measurement setup and thermal conductivity of four SiN nanomembranes (thickness: 30-200 nm) at different temperatures ranging from 300 and 800 K. The thermal conductivity of the membranes thinner than 50 nm increases with temperature, as expected for the SPhP contribution, while that of a 200 nm-thick membrane decreases, in agreement with the phonon counterpart (Fig. 1c). In general, the thermal conductivity decreases as the temperature increases due to more frequent phonon-phonon scattering. However, the two thinner membranes, i.e. 30 and 50 nm-thick membranes, become twice more conductive when their temperature rises from 300 to 800 K [1]. This behavior represents the fingerprints of SPhPs: much longer propagation length of SPhPs ~ mm, while the mean free paths of phonons are below 100 nm [2]. The hybridization of phonons with photons enables ultrafast thermal transport in such a system.

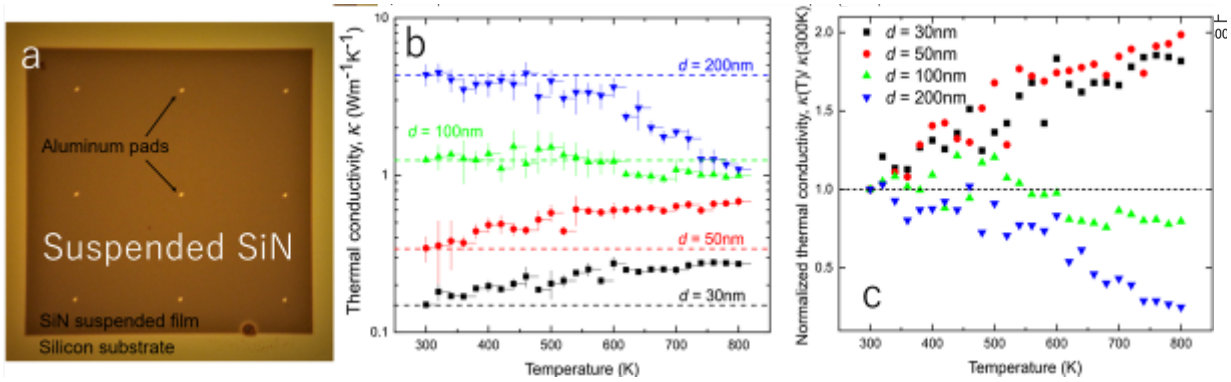

Fig. 1. (a) Optical microscope image of the sample. (b) Thermal conductivity as a function of temperature, for SiN membranes with different thicknesses. (c) Thermal conductivity normalized by the value at room temperature.

References

[1] Y. Wu et al., Sci. Adv. 6, eabb4461 (2020). [2] Y. Wu, et al., Appl. Phys. Lett. 121, 112203 (2022).

Thermal conductivity measurement of transparent thin film by photothermal heating with continuous wave laser

NIMS[1], Univ. of Tsukuba[2]
○(D2) Nicholaus K. Tanjaya[1,2], Satoshi Ishii[1,2]
E-mail: sishii@nims.go.jp

1. Introduction

Optical methods using lasers to extract thermal conductivities including frequency-domain thermoreflectance, time-domain thermoreflectance, and laser flash methods require either pulse lasers or frequency modulated lasers to heat samples. In contrast, we recently developed a thermal conductivity measurement scheme based on quantitative phase microscope (QPM) where a heating laser can be a continuous (CW) laser. The use of CW laser simplifies the optical system. Additionally, our method has an advantage to extract thermal conductivity and thermo-optic coefficient (TOC) simultaneously. In terms of the fitting model of our method, so far it was limited only for transparent substrate. In the current work, we experimentally show that with the modified fitting model, our system can measure the thermal conductivity and TOC of a transparent film on a transparent substrate. A measurement result for an indium gallium zinc oxide (IGZO) thin film deposited on a glass substrate is presented as an example.

2. Method

The optical setup was identical to the one reported in [1] where a CW laser at 788 nm wavelength was used for heating the sample. A 600-nm thick IGZO was sputtered on a glass substrate, and an additional 50-nm thick titanium nitride (TiN) thin film was sputtered on the IGZO where TiN acted as a surface heat source. The phase difference was acquired by the Fourier transform and inverse Fourier transform from the collected interferogram by subtracting the reconstructed phase of the heated and non-heated states. Then, a semi-analytical model was built to model laser power-dependent phase shift of the sample. Since the glass thermal conductivity, the glass substrate and thin film thickness and glass TOC were known, the fitting parameters were reduced to thin film thermal conductivity and TOC.

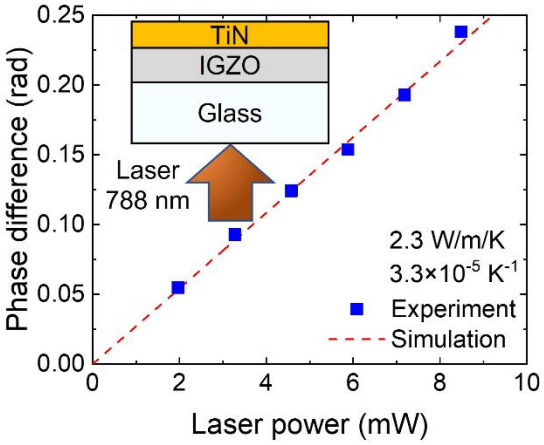

Fig. 1. Measured and fitted results of the power-dependent phase difference for the 600-nm thick IGZO on the glass substrate, including the fitted thermal conductivity and TOC of the IGZO.

3. Results and discussion

The experimental and fitted phase differences for the 600-nm thick IGZO are shown in Fig. 1. The result shows a good agreement between the experimental and fitted phase differences. The fitting result gave 2.3 W/m/K and 3.3×10^{-5} K^{-1} for the IGZO thermal conductivity and TOC. From the reference, the IGZO thermal conductivity is 1.4 W/m/K[2], indicating a reasonable agreement to our measured thermal conductivity. The current work shows that our method is not limited to the determination of the substrate thermo-optic properties but can be extended to thin-film thermo-optic characterization based on the revised fitting model. Our method has the advantage of cost-effective thermal conductivities and TOC characterization compared to other laser heating methods.

References

1. Tanjaya, N.K., K. Toda, T. Ideguchi, and S. Ishii, Opt. Lett., 2023. **48**(12): p. 3311-3314.
2. Yoshikawa, T., T. Yagi, N. Oka, et al., Appl. Phys. Express, 2013. **6**(2): p. 021101.

Nanocavity induced by atomically thin transition metal dichalcogenide in photonic crystal waveguide

[O]C.F. Fong[1], D. Yamashita[2,3], N. Fang[1], S. Fujii[2,4], Y.-R. Chang[1], T. Taniguchi[5], K. Watanabe[6] and Y. K. Kato[1,2]

[1]*Nanoscale Quantum Photonics Laboratory, RIKEN Cluster for Pioneering Research, Saitama 351-0198, Japan*
[2]*Quantum Optoelectronics Research Team, RIKEN Center for Advanced Photonics, Saitama 351-0198, Japan*
[3]*Platform Photonics Research Center, National Institute of Advanced Industrial Science and Technology (AIST), Ibaraki, 305-8568, Japan*
[4]*Department of Physics, Faculty of Science and Technology, Keio University, Yokohama, 223-8522, Japan*
[5]*Research Center for Materials Nanoarchitectonics, National Institute for Materials Science, 1-1 Namiki, Tsukuba 305-0044, Japan*
[6]*Research Center for Electronic and Optical Materials, National Institute for Materials Science, 1-1 Namiki, Tsukuba 305-0044, Japan*

Email: cheefai.fong@riken.jp

Photonic crystal (PhC) cavities can be formed by depositing materials onto PhC waveguides post-fabrication to modulate the local refractive index. Previous studies suggested that ultrahigh Q-factor PhC cavities could be formed with a small local refractive index modulation of ~0.1% [1, 2]. However, experimental attempts to create such cavities by depositing poly(methyl methacrylate) (PMMA) onto GaAs PhC waveguides were unable to achieve ultrahigh Q cavities because of the thick polymer layer [3]. Another approach of placing nanowires along the PhC waveguide to induce the formation of nanocavities have also been reported [4, 5]. Alternatively, 2D materials with their atomically thin nature represent a novel platform to realize the small refractive index modulation to induce high Q nanocavity in a PhC waveguide. In this work, we report the observation of high Q-factor nanocavities formed by placing atomically thin transition metal dichalcogenide (TMDC) flakes onto PhC waveguides.

We first performed finite element method (FEM) simulations and verified that even monolayer TMDC flakes could induce the formation of nanocavities in silicon (Si) PhC waveguides, with theoretical Q-factors of the order of 10^6. We then transferred mono- to few-layered WSe_2 flakes onto the Si PhC waveguides and successfully observed the formation cavity modes in the transmission spectra (Fig. 1).

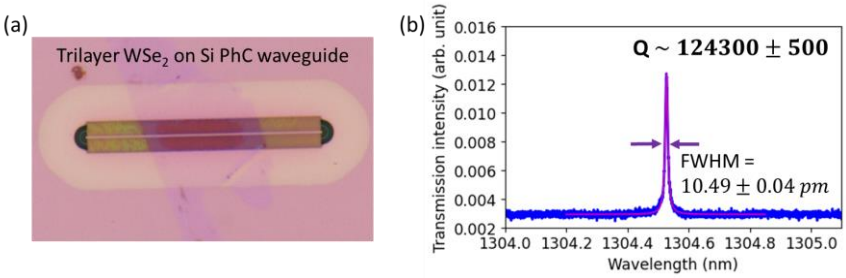

Fig. 1 (a) Optical micrograph of a trilayer WSe_2 flake covering a part of the Si PhC waveguide. (b) Transmission spectra showing the cavity mode with a Q-factor of the order of 10^5.

Acknowledgments: This work is supported in part by JSPS KAKENHI (JP22K14623, JP20J00817, JP22K14624, JP22K14625 and JP23H00262) and ARIM of MEXT (JPMXP1222UT1138), as well as the RIKEN Incentive Research Projects. The growth of hBN crystals is supported by the JSPS KAKENHI (Grant Numbers 20H00354, 21H05233 and 23H02052) and World Premier International Research Center Initiative (WPI), MEXT, Japan. C.F. F. is supported by the RIKEN SPDR fellowship. Y.-R.C. is supported by the JSPS Postdoctoral Fellowship (JP22F22350). We acknowledge support by the RIKEN Information Systems Division for the use of the Supercomputer HOKUSAI BigWaterfall and SailingShip, as well as the use of the COMSOL license.

[1] Opt. Express 14, 12451 (2006). [2] Opt. Express 16, 18657 (2008). [3] Opt. Express, OE 25, 24615 (2017). [4] Nature Materials 13, 279 (2014). [5] ACS Photonics 4, 1040 (2017).

Fabrication of gold nanobridges between gold nanoparticles by localized light

Yuki Takeuchi[1,2], Nobuyuki Takeyasu[3], and Takuo Tanaka[1,4]

[1] Metamaterials Laboratory, RIKEN Cluster for Pioneering Research, Japan
[2] JSPS Research Fellow (PD), Japan,
[3] Graduate School of Natural Science and Technology, Okayama University, Japan,
[4] Institute of Post-LED Photonics, Tokushima University, Japan

E-mail: yuki.takeuchi@riken.jp

1. Introduction

Metallic nanostructure enhances the field intensity of incident light by several orders of magnitude on the surface. The enhanced field can be utilized as *e.g.,* highly sensitive sensor, driving force of chemical reactions, etc., which are never achieved with only light irradiation. For those applications, it is necessary to match the resonance of the nanostructures with excitation wavelength of used light source. The resonance wavelength depends on the size, surrounding media, and geometry. Thus, a wide variety of methods have been developed to control geometries of the nanostructures. Among the geometries, dumbbell structure allows us to tune the resonance widely from visible to near-infrared (NIR) region. The resonance wavelength is determined by the thickness of the center handle [1]. However, it is still challenging to control the thickness of the handle on nanoscale.

We have been studying chemical reactions induced by light localized at the surface of metallic nanoparticle. The localized light enables the induce the reaction not only organic molecules but also metal ions, in other words, reductions. By utilizing reduction, gold nanobridges can be fabricated at the gaps between gold nanoparticles (AuNPs) where intense electric fields are formed to drive the metal ion reductions. In this talk, I will discuss application of the localized light-induced metal ion reductions to metal nanofabrication, where AuNP oligomers were linked via gold bridges generated from gold ion reduction induced by light localized at the gaps and the thickness of the handle was controlled by the time of illumination.

2. Experiments & Results

AuNP oligomers such as the dimer were prepared by adding NaCl and ethanol to the monomer aqueous solution. In order to link AuNP oligomers by ion reduction, $NaAuCl_4$, which is the gold ion source, was added to the solution and the solution was illuminated with fluorescent light. The optical property of linked AuNPs was evaluated by measuring the extinction spectra. The geometry of illuminated AuNP oligomers were directory observed and the linkages were confirmed with transmission electron microscope (TEM).

Fig. 1(a) shows the extinction spectra of the oligomer solution with different illumination times. The extinction in the near-infrared (NIR) region increases with continuous of the illumination. On the other hand, the peak at ~ 300 nm which was derived from the absorption of $AuCl_4^-$ (gold ions) decreased, indicating that gold ions were consumed due to the reduction under the light illumination. Fig. 1(b) shows TEM images of AuNP dimer before and after the light illumination. While a spatial gap was observed between AuNPs before the illumination, the gap was filled with gold after the illumination. It indicated that the AuNP dimer was linked via the gold bridge, which was measured by an energy dispersive X-ray spectroscopy, formed by the reduction of gold ions. From those experimental results, it was considered that the linkage of AuNP oligomers led to resonance shift to NIR region.

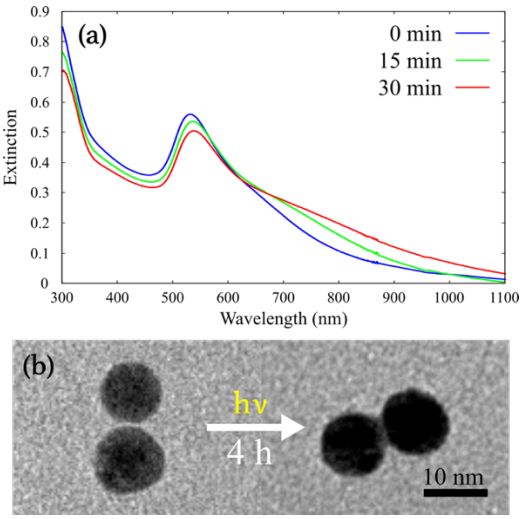

Figure 1(a) Extinction spectra of illuminated AuNP oligomer solution containing gold ions with different illumination time. (b) TEM images of AuNP dimers before and after light illumination for 4 hours.

3. Conclusions

We successfully fabricated gold nanobridges and linked AuNPs by using localized light-induced gold ion reductions. This concept to deposit the metal with a few nanometers in length on the surface of metal nanoparticles by the nanophononics approach might be useful to finer control the geometry of metal nanostructures.

Acknowledgements

This research was supported by JSPS KAKENHI Grant Number JP22KJ2306. We gratefully thank Dr. T. Kikitsu in RIKEN center for emergent matter science for TEM observations.

References

[1] Marek Grzelczak, Ana Sánchez-Iglesias, Benito Rodríguez-González, Ramón Alvarez-Puebla, Jorge Pérez-Juste, Luis M. Liz-Marzán, Adv. Funct. Mater. **18** (2008) 3780– 3786.

Helicity Preserving Scattering by Mie Resonant Silicon Nanoparticles

Hiroshi Sugimoto, Hidemasa Negoro, Minoru Fujii

Kobe University,
E-mail: sugimoto@eedept.kobe-u.ac.jp

1. Introduction

A material system with the electromagnetic duality symmetry responds symmetrically to electric and magnetic fields. Such "dual" system can preserve the helicity of the incident field, *i.e.*, preserve the handedness of circularly polarized incident light (helicity). Helicity preserving nanostructures and metasurfaces have been recently attracting much attentions because they can enhance optical responses of chiral molecules. In general, the resonant nanostructures are "non-dual" and the scattered light does not preserve the helicity of the incident circularly polarized light (Figure 1a). On the other hand, if the incident light is right-handed circular polarization (RCP), the scattered light by "dual" nanoparticles is RCP to all directions (Figure 1b). This is achieved only when a particle responds equally to electric and magnetic fields, which is not the case in natural materials at the optical frequency.

In this work, we present silicon (Si) nanoparticles with Mie resonances can be "dual" nanoparticles. When the nanoparticle exhibits the helicity-preserving scattering, the local chiral fields around the constituent nanoparticles are strongly enhanced, which improves the sensitivity of chiral molecular sensing. We experimentally demonstrate that a solution of Si nanospheres with electric and magnetic Mie resonances can be "dual" at the Kerker condition.[1]

2. Results

Solutions of crystalline Si nanospheres with narrow size distributions are prepared by a method previously reported by our group.[2,3] Figure 1c shows the photos of the solutions and a TEM image of the representative sample. We can see the colored solutions due to the Mie resonance of the Si nanospheres with different sizes. The TEM image demonstrates the spherical and monodisperse Si nanospheres in the sample. To measure the helicity of the scattered light, the nanoparticle solution is illuminated by RCP broadband light. Light scattered to the normal direction is sent to a spectrometer and the polarization is resolved by a quarter wave plate and a linear polarizer to measure the intensities of the RCP and left-handed circular polarization (LCP) components of scattered light. The degree of circular polarization that is equivalent to the helicity density[4] are obtained for different wavelengths.

Figure 1d shows the measured and calculated helicity density spectra of gold (Au) nanosphere solution (D_{ave} = 89.0 nm, σ = 9.9 nm) as a reference. The helicity density is nearly zero in the whole wavelength range. This means that the scattered light by Au nanospheres does not preserve the helicity, *i.e.*, "non-dual". On the other hand, the helicity density of the Si nanospheres in Figure 1e depends on the wavelength. The helicity density is 0.70 (dual), at 685 nm that corresponds to the Kerker condition for electric and magnetic dipole Mie resonances. This means that 85% of the helicity of incident photons are preserved.

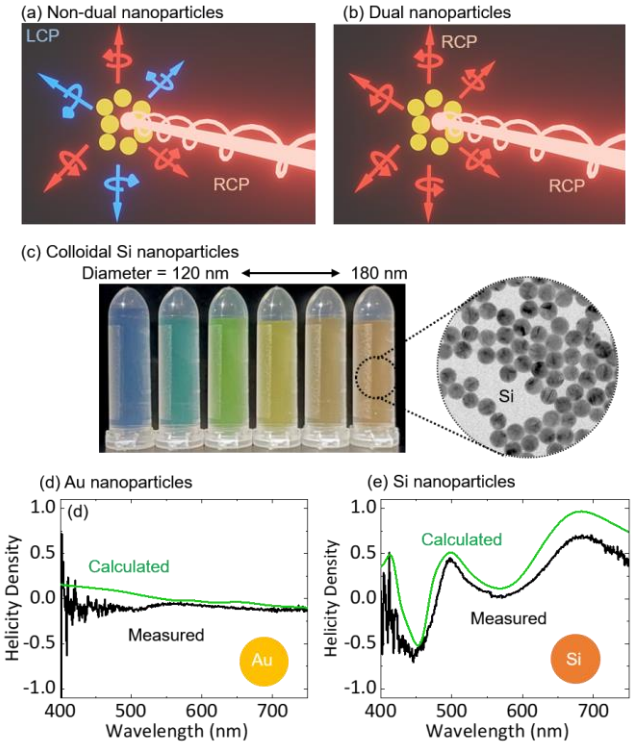

Figure 1. Schematic illustrations of scattering by (a) non-dual and (b) dual nanoparticles. (c) Photos of solutions of Si nanospheres with different diameters. TEM image of Si nanospheres is also shown. Measured and calculated helicity density spectra of solutions of (d) Au nanospheres and (e) Si nanosphere solution.

3. Conclusions

We have shown that a colloidal suspension of Si nanospheres can be a "dual" metafluid that preserves the helicity of incident light at the Kerker conditions. The "dual" nanoparticles can enhance the chiral near-fields in the solution, which may enhance the sensitivity of chiral sensing.

References

[1] H. Negoro, H. Sugimoto, M. Fujii, *Nano Lett.* **2023**, *23*, 5101.
[2] H. Sugimoto, T. Okazaki, M. Fujii, *Adv. Opt. Mater.* **2020**, *8*, 2000033.
[3] T. Hinamoto, S. Hotta, H. Sugimoto, M. Fujii, *Nano Lett.* **2020**, *20*, 7737.
[4] J. Olmos-Trigo, C. Sanz-Fernández, F. Sebastián Bergeret, J. José Sáenz, *Opt. Lett.* **2019**, *44*, 1762.

Gallium Phosphide Nanoparticles for Low-Loss Nanoantennas in Visible Range

Daisuke Shima[1], Hiroshi Sugimoto[1], Artyom Assadillayev[2], Søren Raza[2], Minoru Fujii[1]

[1] Kobe University, [2] Technical University of Denmark
E-mail : sugimoto@eedept.kobe-u.ac.jp

1. Introduction

High index dielectric nanoantennas can localize light into very small space by Mie resonances and enhance the light-matter interactions. Until now, the most studied dielectric material for a nanoantenna is silicon (Si) because of the high refractive index (n > 3.5) in the visible to NIR range and the low extinction coefficient in the red to near infrared (NIR) range. However, the extinction coefficient of Si increases at shorter wavelength, in particular below 600 nm. This limits the performance of a nanoantenna in the short wavelength range. An alternative material of a nanoantenna operating in a short wavelength range is gallium phosphide (GaP). It has a moderately high refractive index (n > 3) and a small extinction coefficient because of the much larger indirect band gap 2.26 eV (~550 nm) than that of Si (1.12 eV) [1]. However, research on GaP nanoantenna is very scarce. For example, a spherical GaP nanoparticle (NP) has not been developed and the antenna performance has not been studied.

In this work, we develop colloidal solution of spherical GaP NP nanoantennas operating below 600 nm. We produce spherical GaP NPs by the combination of mechanical milling and a pulsed laser melting in liquid process. We conduct the single particle scattering spectroscopy and reveal that the NPs exhibit size tunable Mie resonances in the visible range [2].

2. Sample preparation

Ball milling and pulsed laser melting in liquid (PLML) processes are combined for the fabrication of spherical GaP NPs. Figure 1 shows a schematic of the preparation procedure. First, GaP NPs with an irregular shape and the sizes of < 1 μm are prepared by planetary ball milling for 30 min at 800 rpm. Then, the NPs are dispersed in acetone with the concentration of 1 mg/mL, and the solution was the subject to the PLML process. In the PLML process, particles are heated in a liquid by pulsed laser irradiation, converted to melt droplets, and then instantaneously cooled by a surrounding medium. For the PLML process, we use the third harmonics of pulsed Nd:YAG laser (5 ns pulse duration, 20 Hz repetition), and the particles are irradiated for 1 min with a laser fluence of 63 mJ·pulse^{-1}·cm^{-2}.

Figure 1. Schematic of preparation procedure of GaP NPs.

3. Results and discussion

Figure 2a shows SEM images of GaP NPs with diameters from 310 to 174 nm after PLML process. Figure 2b show measured scattering spectra of corresponding single GaP NPs. Calculated scattering spectra of spherical GaP NPs with the same diameters are shown in Figure 2c. The NPs have smooth surface and almost spherical shape. Measured scattering spectra have distinctive peaks and comparison between measured and calculated spectra allows us to assign the peaks to different Mie modes. The smallest NP (D = 174 nm) supports the lowest-order Mie resonances, magnetic and electric dipole (MD, ED) modes, while the largest NP (D = 310 nm) supports the higher-order Mie resonances up to magnetic octupole (MO) and radial higher-order magnetic quadrupole (MQ^2) modes in the visible range. The GaP NPs have distinctive Mie resonances below 600 nm. For example, the distinctive MQ peak is seen at 450 nm in a 191 nm GaP NP (blue curve). Also, the EQ peak is observed at 480 nm for a 230 nm GaP NP. This suggests the nanoantenna with size tunable Mie resonances operation at the short wavelength range.

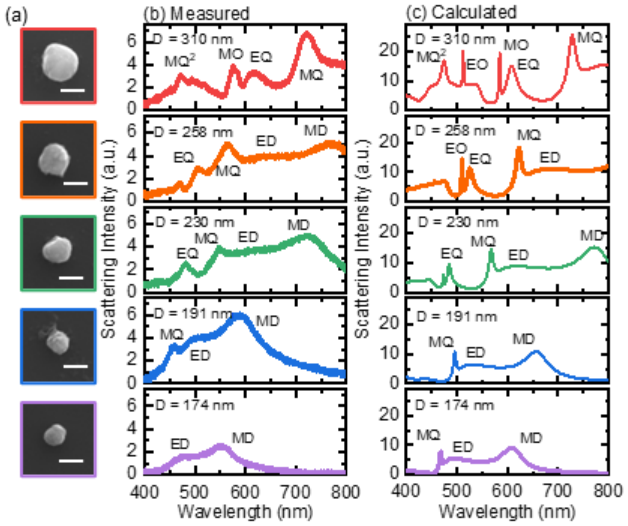

Figure 2. (a) SEM images of GaP NPs. Scale bars are 200 nm. (b,c) Measured (b) and calculated (c) scattering spectra of corresponding GaP NPs.

In the presentation, we report the Mie resonances supported by GaP NPs by comparing with that of Si NPs and demonstrate Purcell enhancement of dye molecules by GaP NPs.

References

[1] J. Cambiasso, et.al. Nano Lett. 2017, 17, 1219.
[2] D. Shima, et.al, Adv. Optical Mater. 2023, 2203107

Nanoparticle Film Based Mechanoplasmonic Sensors for Wearable Strain Applications of Human-Motion Monitoring

Hiroaki Matsui [1], Akira Momose [2], Hidehiko Yoda [3] and Aki Fujita [4]

[1] The University of Tokyo, [2] Kanagawa Institute of Industrial Science and Technology, [3] Utsunomiya University, and [4] Science & Technology Inst. Co.
E-mail: hiroaki@ee.t.u-tokyo.ac.jp

1. Introduction

Recently, electronic devices with stretchable features have received much attention because of the huge promises of strain sensors for human motion monitoring. Flexible strain sensors can monitor large mechanical deformations exceeding commercial electric strain sensors. Similarity, the mechanical method is known as one of external field control of SPRs, which provides an alternative while promising approach for mechano-plasmonic devices.

In this work, we aim to investigate operating mechanism, strain sensing activities and demonstration of stretchable strain sensors by human motion monitoring. Our group has implemented the structural and chemical control of the plasmonic properties of assembled films of Sn-doped In_2O_3 nanoparticles (ITO-NP films). Herein, we propose mechanical applications as dynamic control of plasmonic properties of the ITO-NP films for optical strain sensing techniques. In particularly, the ITO-NP films show highly resonant reflections in the IR range as consequences of optical properties as metamaterials, which are used as optical probes of strain detection. We report the challenges in the use of flexible skin-mountable and wearable sensors as the potential applications of flexible strain sensors using the SPRs of ITO-NP films.

2. Results and Discussion

Figure 1(a) shows reflectance spectra of the NP film placed on a PDMS substrate sheet measured under different applied strains (ε) from 0 to 50%. The total reflectance gradually decreased with an increase in applied strain, which was observed following with blueshifts of two resonances (peaks I and II). Herein, the electrical field of the incident light was parallel to the loading direction [inset of Figure 1(b))]. Reflectance changes at peaks I and II exhibited linear manners, relating to the strain - stress relations generated in the strained NP film. In addition, we observed optical anisotropy in reflectance change of the strained NP film, suggesting formation of anisotropic surface morphologies in the strained NP film. Actually, the anisotropic fragment structures were observed by high-resolution optical microscopy [Figures 1(c) and 1(d)]. The fragments played a key role in determining the optical properties.

Next, we demonstrated the flexibility of the optical strain sensor as a wearable device. Finger movement is a representative portion of wearable strain measurements. We attached the NP film to the joint part of the index finger using a glove with an adhesive tape to monitor human motion in real time. The spectral changes of the NP film were observed at different finger-bending angles [Figures 2(a) - 2(c)]. Figure 2(d) shows the reflectance spectra of the NP film as a function of the bending angle (α) measured by

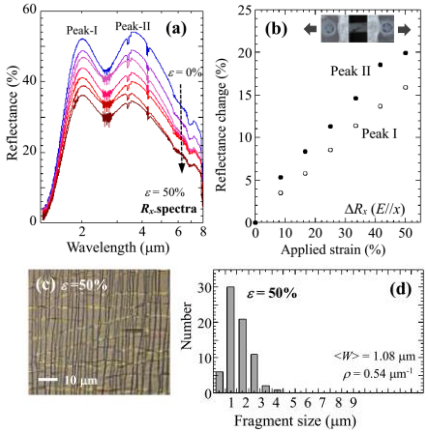

Figure .1 (a) Reflectance spectra as a function of applied strain. (b) Reflectance changes in resonant peaks I and II as a function of applied strain. (c) Optical surface image and histogram of fragment sizes of the NP film under an applied strain of 50%.

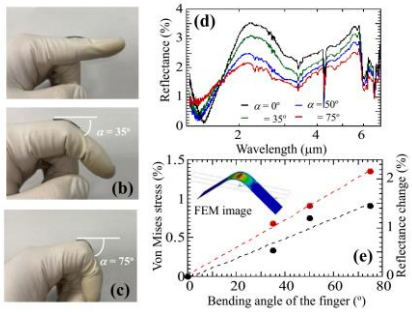

Figure 2. Images of the bending angles (α) of the index finger at (a) 0°, (b) 50°, and (c) 75°. (d) Reflectance spectra of the ITO NP film at different bending angles. (e) Relationship between the change in reflectance and von Mises stress as a function of the bending angle. Inset represents a simulated von Mises stress image on the joint part of the index finger at a bending angle of 75°.

placing the index finger. As the bending angle increased from 0° to 75°, the reflectance gradually decreased with a peak shift to the region with a shorter wavelength, relating to an increase in mechanical deformation. This spectral change was related to the stress distribution on the finger. The correlation between the stress and reflectance revealed that the NP film could detect the mechanical deformation of a human motion such as finger flexion.

Acknowledgment

This study was conducted by Ichimura Foundation for New Technology, and JSPS Scientific Research (B) (grant 18H01468).

[20a-A602-2~6] 4.1 Plasmonics and Nanophotonics

Nicholas Smith(Osaka Univ.)

Wed. Sep 20, 2023 10:15 AM - 11:45 AM A602 (KJ Hall)

△ : Presentation by Applicant for JSAP Young Scientists Presentation Award

▲ : English Presentation

▼ : Both of Above

No Mark : None of Above

▲[20a-A602-2] [JSAP-Optica Joint Symposia 2023 Invited Talk] New Developments in Plasmonics and Nanophotonics for Full-Color Tuning of Resonance Spectra in a Wide Wavelength Range

○Koichi Okamoto[1] (1.Osaka Metro. Univ.)

10:15 AM - 10:45 AM

▲[20a-A602-3] Dynamically tunable structural color filter using a phase change material.

○(DC)Ram Prakash S[1], Rajesh Kumar[1], Anirban Mitra[1] (1.Indian institute of technology ROORKEE)

10:45 AM - 11:00 AM

▼[20a-A602-4] Absorption Enhancement of WS_2 with All-dielectric Metasurface Based on Mie Resonance and Degenerate Critical Coupling

○(D)Dingwei Chen[1], Junichi Takahara[1,2] (1.Grad. School of Eng., Osaka Univ., 2.Photonics Center, Grad. School of Eng., Osaka Univ.)

11:00 AM - 11:15 AM

▲[20a-A602-5] Influence of Substrate temperature on the performance of Schottky photodetector based on Au/n-Si structure.

○(DC)DINESH DUDI[1], BRAHIM AISSA[2], RUI N. PEREIRA[3], ANIRBAN MITRA[1] (1.IIT ROORKEE, 2.HBKU QATAR, 3.Univ. of Aveiro)

11:15 AM - 11:30 AM

▲[20a-A602-6] Near-field intensity enhancement under an aberrated focusing

○(D)Sarita Mehra[1], Rajan Jha[2], Rakesh Kumar Singh[1] (1.IIT-BHU, Varanasi, 2.IIT-Bhubaneswar)

11:30 AM - 11:45 AM

New Developments in Plasmonics and Nanophotonics for Full-Color Tuning of Resonance Spectra in a Wide Wavelength Range

Osaka Metro. Univ.[1] , ◦Koichi Okamoto[1]

E-mail: OkamoT@omu.ac.jp

Tuning optical properties using nanophotonics and plasmonics has attracted significant attention across various fields. Different fabrication methods, including top-down and bottom-up approaches, have been utilized to create diverse nanostructures. Each method has its own advantages and disadvantages. In this study, we present novel nanostructures and recently discovered methods.

For instance, we achieved wide wavelength tuning and obtained full colors using random nanohemisphere-on-mirror (NHoM) structures [1]. These structures enabled full coverage of the standard RGB color space and exhibited color quality comparable to periodic structures. NHoM structures also demonstrated improved sensor performance and successful colorimetric sensing with protein drops [2]. Moreover, we successfully controlled resonance spectra in the deep ultraviolet (UV) [3, 4] and near-infrared (IR) [5] regions using similar random structures. The flexibility in tuning optical properties holds great promise for the advancement of plasmonics and nanophotonics. Additionally, we discovered that heat treatments can significantly enhance the optical properties of Au and Ag nano-disks fabricated using electron beam lithography [6]. By manipulating the temperature, we can easily adjust the resonance wavelength. This simple and effective method allows for flexible tuning of plasmonic properties and opens up a wide range of potential applications.

One futuristic application of plasmonics is the development of high-efficiency light-emitting diodes (LEDs). In our research, we propose a new method to enhance the emission efficiencies of InGaN/GaN by depositing dielectric thin films between GaN and metal nanostructures [7]. Furthermore, we introduce a novel approach that utilizes dielectric thin films instead of metals, combined with UV laser irradiation [8]. This advancement simplifies the application to LED devices without the need for specialized light extraction structures. These breakthroughs pave the way for highly advanced light-emitting devices, including highly efficient RGB LEDs and micro-LED displays.

The author would like to express gratitude to Prof. T. Matsuyama and Prof. K. Wada (Osaka Metro. Univ.), Prof. K. Tamada (Kyushu Univ.), Prof. M. Terazima, Prof. M. Funato, and Prof. Y. Kawakami, (Kyoto Univ.) for their valuable discussions and support. This work has been supported by the JSPS Grants-in-Aid for Specially Promoted Research (No. JP20H05622) and Scientific Research (S) (No. JP19H05627), as well as exploratory research (No. JP21K19218).

[1] K. Okamot, K. Okura, P. Wang, S. Ryuzaki and K. Tamada, *Nanophotonics*, **9**, 3409 (2020).
[2] S. Maeda, N. Osaka, R. Niguma,T. Matsuyama,K. Wada, K. Okamoto, *Nanomaterials*, **13**, 1650 (2023).
[3] K. Shimanoe, S. Endo, T. Matsuyama, K. Wada, K. Okamoto, *Sci. Rep.* **11**, 5169 (2021).
[4] S. Endo, K. Shimanoe, T. Matsuyama, K. Wada, K. Okamoto, *Opt. Mater. Express*, **12**, 2444 (2022).
[5] K. Shimanoe, S. Endo, T. Matsuyama, K. Wada, K. Okamoto, *Appl. Phys. Exp.*, **14**, 042007 (2021).
[6] N. Osaka, M. Ozawa, T. Matsuyama, K. Wada, K. Okamoto, *Opt. Mater. Express*, **13**, 1504 (2023).
[7] S. Kaito, T. Matsuyama, K. Wada, M. Funato, Y. Kawakami, K. Okamoto, *Appl. Phys. Lett.*, **122**, 151110 (2023).
[8] S. Kaito, T. Matsuyama, K. Wada, M. Funato, Y. Kawakami, K. Okamoto, *Research Square*, DOI：10.21203/rs.3.rs-2515057/v1, Patent Application Number: 2022-014115, PCT/JP2023/003083

Dynamically tunable structural color filter using a phase change material.

Ram Prakash S[1], Rajesh Kumar[1], Anirban Mitra[1]

[1] Department of Physics, Indian Institute of Technology Roorkee, Roorkee, 247667, India
E-mail : rprakashs@ph.iitr.ac.in

1. Introduction

Structural colors produced by metamaterials have attracted huge interest due to their use in color printing [1], chromatic display [2] and optical encryption [3]. The dynamical color tunability can be achieved by using phase change material (PCM) in the metamaterial design. $Ge_2Sb_2Te_5$ (GST) is a PCM that shows a large contrast in its dielectric permittivity upon phase transformation. Here, we present a generation of structural color using GST based tunable reflective metamaterial. By changing the crystallization of GST, many colors can be generated. Further, high resolution wide color gamut is obtained by varying the geometrical parameters of the metamaterials design. The results show a promising route to achieve a dynamically tunable color filter using a phase change material.

2. Design and Results

The schematic diagram of the tunable color filter is shown in Figure 1(a). On top of the Aluminum metal substrate a thin film Al_2O_3 is deposited. GST square gratings with a specific period (P_x and P_y) and side length of $a_x=F_x*P_x/100$ and $a_y=F_y*P_y/100$ are deposited on top of the Al_2O_3. Here, F_x and F_y are the fill fraction of square grating. The thickness of Al is chosen as 100 nm. Self developed

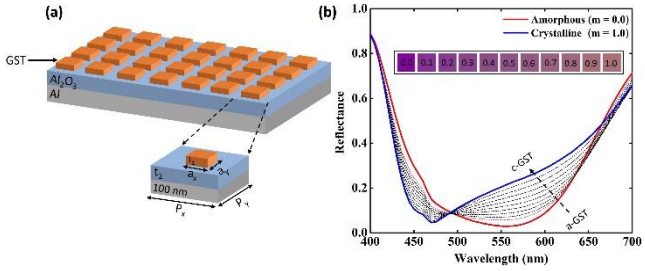

Figure 1: a) Schematics of GST based tunable color filter. b) The reflectance spectrum of the color filter for different crystallization fraction of GST

MATLAB code of Rigorous Coupled Wave analysis (RCWA) is used to solve the electromagnetic fields [4]. The refractive index of GST in both phases is obtained from previous experimental results [5]. The effective permittivity of GST in mixed phase can be written as [6]

$$\frac{\epsilon_{eff}(\lambda)-1}{\epsilon_{eff}(\lambda)+2} = m \times \frac{\epsilon_c(\lambda)-1}{\epsilon_c(\lambda)+2} + (1-m) \times \frac{\epsilon_a(\lambda)-1}{\epsilon_a(\lambda)+2}$$

Here m is the crystallization fraction of GST in the range 0 to 1, $\epsilon_a(\lambda)$ and $\epsilon_c(\lambda)$ is the permittivity of GST in amorphous and crystalline phase, respectively. The reflectance spectra for both phases of GST are obtained by normally incident plane waves from 400 nm to 780 nm and is shown in Figure 1(b). The geometrical parameters are F_x = F_y = 75%, P_x = P_y = 250 nm, t_1 = 15 nm, t_2 = 200 nm. By varying m from 0 to 1 the reflectance minimum gradually blue shifts to smaller wavelength. The inset in Figure 1(b) shows the corresponding colors generated for various crystallization fraction of GST. A maximum color difference ΔE_{2000} of 31.9 is observed with complete phase transformation.

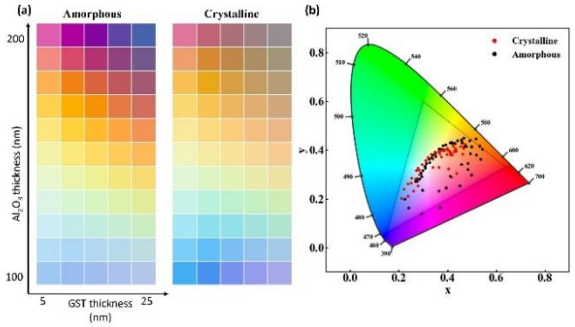

Figure 2: a) Color Pallet produced by the GST in both the phases with a period and fill fraction of 250 nm and 75%, respectively. b) All colors produced by the metamaterial plotted in CIE chromaticity diagram

Further, more colors can be generated by varying the geometrical parameters such as the thickness of GST and Al_2O_3. Figure 2 shows the colors produced by varying the thickness of GST from 5 nm to 25 nm and Al_2O_3 from 100 nm to 200 nm while the period and fill fraction are fixed at 250 nm and 75%, respectively. It is observed that the increase in Al_2O_3 thickness changes the hue of color generated while the increase in GST thickness leads to the decrease in saturation. Figure 2(b) show the CIE chromaticity diagram of all the colors produced in both the phases of GST. Overall, we generated 110 colors by changing the phase, thickness of GST, and Al_2O_3.

3. Conclusions

In conclusion, the proposed tunable structural color filter shows a wide color gamut and can be dynamically tuned by varying the phase of GST. Further, by changing the thickness of GST and Al_2O_3 we could generate a large number of color with different hue and saturation. Thus, the proposed color filter could be utilized in image encryption, anti-counterfeiting, and dynamic displays.

References

[1] S. Sun, ACS Nano 11, 4445–4452 (2017).
[2] C. Ríos, Adv. Mater. 28, 4720–4726 (2016).
[3] X. Luo, Adv. Opt. Mater. 8, 1902020 (2020).
[4] R. C. Rumpf, Prog. In Electromagn. Res.B 35,241–261 (2011).
[5] K. Shportko, Nat. Mater. 7, 653–658 (2008).
[6] R. Prakash Appl. Opt. 61, 2888 (2022).

Absorption Enhancement of WS_2 with All-dielectric Metasurface Based on Mie Resonance and Degenerate Critical Coupling

Dingwei Chen[1] and Junichi Takahara[1,2]

1 Grad. School of Eng., Osaka Univ., 2-1 Yamadaoka, Suita, Osaka 565-0871, Japan
2 Photonics Center, Grad. School of Eng., Osaka Univ., 2-1 Yamadaoka, Suita, Osaka 565-0871, Japan
E-mail: takahara@ap.eng.osaka-u.ac.jp

1. Introduction

Atomically thin Two-dimensional (2D) transition-metal dichalcogenides (TMDCs), such as WS_2, have emerged over the past few years for their unique optical and transport features in optoelectronic and photonic applications[1,2]. Nevertheless, their ultrathin thickness results in weak optical absorption [3]. To accomplish strong light absorption, a dielectric-based metasurface based on Mie resonance and degenerate critical coupling can realize superimposed modes enhancement effects on WS_2[4].

Here, we achieve a huge absorption increase of WS_2 with an all-dielectric metasurface, when peaks of electric and magnetic dipole (ED and MD) modes of metasurface overlaps in the wavelength near the peak related to excitonic transitions in monolayer WS_2.

2. Results and Discussion

First, we study the optical spectrum of Mie resonator metasurface substrate. Figure 1a shows the structure design of WS_2 on the metasurface. Among them, the Mie metasurface is comprised by Mie resonator arrays with period *d*, radius *r*, and thickness *h*. Figure 1b shows the calculated absorption spectral map of Si Mie resonators with *h* = 55-115 nm. ED and MD modes increase as *h* increases, while the MD mode experienced a larger red shift compared to the ED mode. An overlap of two modes shows when *h* = 89 nm.

In Figure 1c, when ED and MD modes overlap, simulated absorption of WS_2 on the metasurface shows a huge excitonic peak of “A” compared with absorption of individual metasurface. Without background, the absorption of WS_2 is increased by about 68% compared with WS_2 on Si substrate as shown in Figure 1d. At the same time, the 9 nm red shift of the absorption peak shows that the absorption enhancement of WS_2 is related to the influences of Mie resonator modes on the energy band structure of WS_2.

3. Conclusions

The absorption of WS_2 monolayer as high as 0.73 is achieved with a red shift of 9 nm. This architecture could be used in the future as a highly efficient tunable single-color photodetector. Moreover, the suggested dielectric metasurface holds promise for semiconductor 2D materials in visible wavelength.

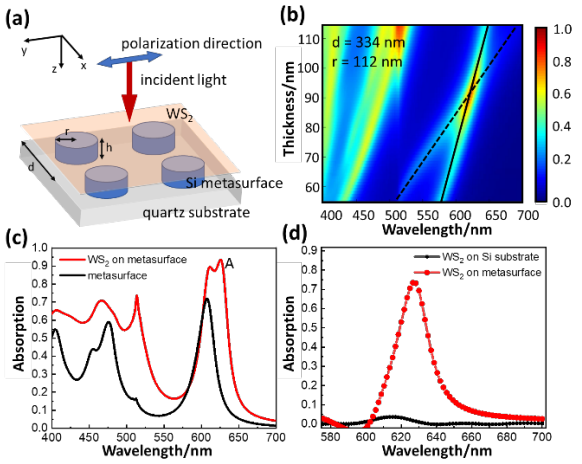

Figure 1. (a) Schematic illustration for WS_2 on Si metasurface, which is constituted by Si Mie resonator arrays. (b) Absorption spectral map of Si Mie resonators with change of thickness *h*. Among them, *d* = 334 nm and *r* = 112 nm. (c) Absorption for metasurface with *h* = 89 nm, *d* = 334 nm and *r* = 112 nm (black line), and WS_2 on the metasurface (red line). (d) Absorption without background for WS_2 on Si substrate (black line) and metasurface in (c) (red line).

Acknowledgements

This work was supported by the Japan Society for the Promotion of Science (JSPS) KAKENHI 23H00274. Dingwei Chen was supported by the China Scholarship Council (No. 202204910108).

References

[1] Q. Wang, *et al.*, Nature Nanotech. **7**, 699 (2012).
[2] W. Xu, *et al.*, Nature **541**, 62 (2017).
[3] E. Buhara, *et al.*, Plasmonics **16**, 687 (2021).
[4] R. Xu, J. Takahara, Opt. Lett. **46**, 805 (2021).

Influence of Substrate temperature on the performance of Schottky photodetector based on Au/n-Si structure

Dinesh Dudi[1], Brahim Aissa[2], Rui N. Pereira[3], Anirban Mitra[1]
[1] Department of Physics, Indian Institute of Technology Roorkee, Roorkee, 247667, India
[2]Qatar Environment & Energy Research Institute (QEERI), Hamad Bin Khalifa University (HBKU), Qatar Foundation, PO Box 34110, Doha, Qatar
[3] Department of Physics and i3N-Institute for Nanostructures, Nanomodelling and Nanofabrication, University of Aveiro, 3810-193 Aveiro, Portugal.
E-mail: dinesh_d@ph.iitr.ac.in

1. Introduction

Nowadays, metal nanoparticles (NPs) are particularly very promising and intriguing in research and technology because of their quantum confinement effect, easy manufacturing, low-cost, controllable synthesis, and more effective charge transport [1]. These nanostructures are utilized to develop a device such as gas sensors, solar cells, photodetectors, and LEDs. The surface plasmon resonance wavelength of the metal NPs can be tailored to certain spectral areas by modifying their size, shape, and surrounding dielectric medium [2]. The energy of incident light below the semiconductor's bandgap energy can be detected using an internal photoemission Schottky barrier photodetector developed at the interface of a metal and semiconductor.[3] The interface between deposited metal and the semiconductor surface plays a significant role in determining the quality of a Schottky contact. As the annealing temperature rises, several aspects of the interface alter. In this report, Au-NPs /n-Si-based Schottky photodetector is fabricated by depositing Au-nanoparticle thin film on a Si substrate at different substrate temperatures using a pulsed laser deposition technique. The Au NPs/ n-Si photodetector shows good responsivity of 1.095 A/W under the illumination of a 735nm wavelength LED source.

2. Design and Results

Using the PLD technique, gold nanoparticle thin films were formed on cleaned n-type silicon substrates. All the substrates were ultrasonically cleaned with acetone, ethanol, and de-ionized water in that order, taking 3 min for each step with the final cleaning step in diluted HF: H_2O (1:10) solution for the 30s for SiO_2 layer removal. The third harmonic of the Nd: YAG laser, operating at a wavelength of

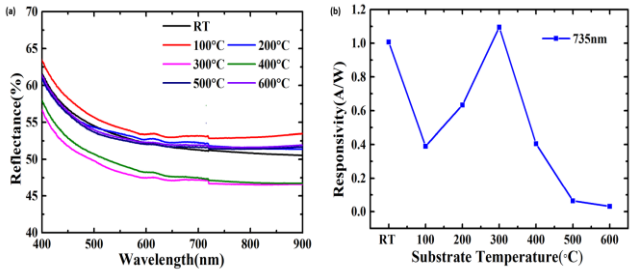

Figure 1: a) Reflectance spectra and b) responsivity of Au/n-Si photodetector

355nm, with a pulse repetition rate of 10 Hz and pulse width of 8 ns, was utilized to ablate the gold target after the PLD chamber was evacuated to a base pressure of 1.5× 10^{-5} mTorr. The distance between the target and substrate is fixed at 3.5 cm for deposition, the number of laser shots is 300, and the energy was 70 mJ/Pulse. Gold thin films were grown at different substrate temperatures (Room Temperature(RT)-600°C) in steps of 100°C and post-annealed at the same temperature for 30 minutes. Thermal evaporation was used to create a 100 nm thick silver bottom electrode on the Si, and finger-shaped silver contacts were implanted on top of the Au nanoparticle thin films to serve as an upper electrode.

Fig 1(a) shows the reflectance spectra of the thin gold films, which were deposited on an n-Si substrate at different substrate and annealing temperatures. The minimum reflectance is obtained when the annealing temperature is 300°C. As the substrate temperature increases at first, reflectance decreases, and after 300°C, it increases.

The ratio of the photogenerated current (I_{ph}) to the incident light power (P_{in}) is known as the device's responsivity (R). The response is characterized as [4]

$$R = \frac{I_{ph}}{P_{in}} = \frac{I_{illu} - I_{dark}}{P_{in}}$$

Where I_{dark} is the dark current, I_{illu} is the photogenerated current, and P_{in} is the incident power of light. In Fig 1(b), we obtained the maximum photo response for a sample deposited at 300°C. There is minimum reflectance for the 300°C deposited sample showing particles of different sizes that can absorb a broad part of light spectra. and the dark current for this device is also very low 0.2mA. The responsivity of the Au NPs/n- Si Schottky diode exhibits maximum responsivity of 1.095 A/W at 300°C substrate and annealing temperature at +5V under 735nm light illumination.

3. Conclusions

Au nanoparticle thin film is deposited on quartz and n-type silicon wafer at different temperatures (100°C-600°C) in steps of 100°C by PLD. The Reflectance spectra show minimum reflectance when the annealing temperature is 300°C. Schottky diode based on Au NPs/n-Si exhibits maximum responsivity of 1.095 A/W at 300°C substrate and annealing temperature at +5V under 730nm light illumination.

References

[1] Jun J., Ceram. Int", Volume 35, Issue 7, 2009.
[2] Y.A. Akimov Plasmonics 4, 107–113, (2009)
[3] S.M. Tunhuma Physica B 480 201–205, 7 (2015)
[4] S. Chaudhary AIP Conf. Proc. 2220, 090022-1, (2020)

Near-field intensity enhancement under an aberrated focusing

Sarita[1*], Rajan Jha[2], Rakesh Kumar Singh[1]

[1] Laboratory of Information Photonics & Optical Metrology, Department of Physics, Indian Institute of Technology (Banaras Hindu University), Varanasi, 221005, India, [2] Nanophotonics and Plasmonics Laboratory, School of Basic Sciences, Indian Institute of Technology Bhubaneswar, Bhubaneswar, 751013, India
E-mail: sarita.rs.phy19@itbhu.ac.in

1. Abstract

Near-field intensity enhancement due to the plasmonic response of nanoparticles is investigated with the Mie theory and multipole expansion for an aberrated focusing system. Spherical aberration and defocusing are considered as an aberration in the focusing system.

2. Introduction

When a focused beam scatters through a nanoparticle (NP), an enhancement in intensity is observed in the near-field due to the plasmonic properties of the NP [1]. An aplanatic lens system of high numerical aperture is used to make a tight focal spot. An optical system having aberration is a common problem which affects the shape and size of the beam at the focus [2].

A tight focus of a linearly polarized beam is considered for illuminating a plasmon active silver NP of 50nm radius in a dielectric media glass having refractive index ($n_m = 1.52$). The expansion coefficient defining the incident and scattered field using Mie theory, for an aberrated system, is expressed as

$$A_n = \frac{-i^n k f e^{ikf} E_0 (2n+1)}{2n^2 (n+1)^2} \int_0^{\alpha} e^{ikW(\rho)} \sqrt{\cos(\theta)} * \left\{ \frac{P_n^1(\cos\theta)}{\sin\theta} + \frac{dP_n^1(\cos\theta)}{d\theta} \right\} \sin\theta d\theta \quad (1)$$

where n is the multipole order, k is the wave number, f is the focal length of the lens, E_0 is the amplitude of field, and $P_n^1(\cos\theta)$ is associated Legendre polynomial. The angular semiaperture of the lens is $\alpha = 60°$.

Wave aberration is represented as $W(\rho) = A_s \rho^4 + A_d \rho^2$ where $\rho = \sin\theta / \sin\alpha$. A_s and A_d are the coefficients of spherical aberration and defocusing in wavelength units. To reduce the effect of aberration, a balancing condition $A_d = -A_s$ is introduced. The average radial (K_r) and tangential (K_t) intensity enhancement is expressed as [1]

$$K_r = \frac{9}{16(ka)^4} \sum_{n=1}^{\infty} \frac{|A_n|^2}{|A_1|^2} \frac{2n^3 (n+1)^3}{2n+1} \left[|a_n|^2 |\chi_n|^2 + |\psi_n|^2 - 2\,\mathrm{Re}\{a_n \chi_n\} \psi_n \right], \quad (2)$$

and

$$K_t = \frac{9}{16(ka)^2} \sum_{n=1}^{\infty} \frac{|A_n|^2}{|A_1|^2} \frac{2n^2 (n+1)^2}{2n+1} \left[|a_n|^2 |\chi_n'|^2 + |b_n|^2 |\chi_n|^2 + |\psi_n|^2 + |\chi_n'|^2 - 2\,\mathrm{Re}\{a_n \chi_n'\} \psi_n' - 2\,\mathrm{Re}\{b_n \chi_n\} \psi_n \right] \quad (3)$$

where a_n, b_n are the scattering coefficients, χ_n, ψ_n are the Riccati-Bessel functions, χ_n', and ψ_n' are the respective derivatives [4].

3. Result

Average radial and tangential intensity enhancement are presented in Fig 1(a), (b) respectively with respect to wavelength of incident light ranging from 300nm to 900nm for different strengths of aberration.

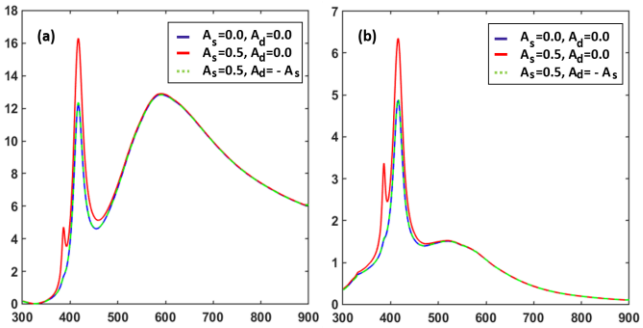

Fig 1: Average (a) radial, (b) tangential intensity enhancement for a silver NP without aberration (blue curve), with aberration (red curve), and with defocusing to balance aberration (dashed green) with respect to wavelength.

4. Conclusion

The effects of spherical aberration and defocusing on the plasmon excited near-field intensity are numerically examined. An increase in the near-field intensity is observed due to the presence of spherical aberration.

Acknowledgements

Sarita acknowledges support from her institute IIT-BHU, and UGC (SRF) scholarship.

References

[1] Mojarad N M, Sandoghdar V and Agio M J. Opt. Soc. Am. B 25 (2008) 651-658.
[2] Singh, Rakesh Kumar, P. Senthilkumaran, and Kehar Singh Invertis J. Sci. Technol 1.4 (2008) 197-230.
[3] Singh, Rakesh Kumar, P. Senthilkumaran, and Kehar Singh JOSA A 25.6 (2008) 1307-1318.
[4] Bohren C F and Huffman D R 1983 John Wiley & Sons

4 JSAP-Optica Joint Symposia 2023 | Oral presentation | 4.2 Photonics Devices, Photonic Integrated Circuit and Silicon Photonics

[19p-A310-1~13] 4.2 Photonics Devices, Photonic Integrated Circuit and Silicon Photonics

Kondo Keisuke(Utsunomiya Univ.), Naoko Inoue(住友電工)

Tue. Sep 19, 2023 1:00 PM - 5:00 PM A310 (KJ Hall)

△：Presentation by Applicant for JSAP Young Scientists Presentation Award

▲：English Presentation

▼：Both of Above

No Mark：None of Above

▲[19p-A310-1] [JSAP-Optica Joint Symposia 2023 Invited Talk] Video-rate Spectral Imaging Chip based on Metasurfaces

○Yidong Huang[1], Kaiyu Cui[1], Jian Xiong[1], Jiawei Yang[1] （1.Tsinghua University）

1:00 PM - 1:30 PM

▲[19p-A310-2] Low temperature annealing for vanadium dioxide in photonic integrated circuits

○(DC)Yuxin Du[1], Kai Sun[1], Zihang Zheng[1], Cornelis H de Groot[1], Xu Fang[1] （1.Univ. of Southampton）

1:30 PM - 1:45 PM

▼[19p-A310-3] Hybrid silicon all-optical switching devices integrated with two-dimensional materials

○Daiki Yamashita[1,2], Nan Fang[1], Shun Fujii[1,3], Yuichiro Kato[1] （1.RIKEN, 2.AIST, 3.Keio Univ.）

1:45 PM - 2:00 PM

▲[19p-A310-4] Grating Diffraction Select Radial Mode at the Inner Active Cladding of Hybrid-Cavity Microlaser

○(DC)Jinghan Chen[1], Abazi Adrian[2,3], Eich Alexander[2,3], Tomishige Yoshitaka[1], Takeda Harunobu[1], Mikami Yuya[1], Tate Naoya[1], Oki Yuji[1], Schuck Carsten[2,3], Yoshioka Hiroaki[1] （1.Kyushu Univ., 2.Munster Univ., 3.SoN Munster）

2:00 PM - 2:15 PM

▲[19p-A310-5] Gain Induced Dispersion Effects on Airy Pulse

○(D)Deependra Singh Gaur[1], Akhilesh Kumar Mishra[1] （1.IIT Roorkee）

2:15 PM - 2:30 PM

▲[19p-A310-6] Electric Field-Induced Mode Switching in Few-Mode Fibers

○(D)Isha Sharma[1], Partha Roy Chaudhuri[1] （1.IIT KGP）

2:30 PM - 2:45 PM

▲[19p-A310-7] Shifting zero-dispersion wavelength of silica-dielelctric Bragg fiber

○(D)Saikat Mondal[1], Partha Roy Chaudhuri[1] （1.IIT Kharagpur）

2:45 PM - 3:00 PM

▲[19p-A310-8] [JSAP-Optica Joint Symposia 2023 Invited Talk] Beam Steering with Integrated Optical Phased Array using DNN

○Makoto Nakai[1], Isamu Takai[1] （1.Toyota Central R&D Lab）

3:15 PM - 3:45 PM

▲[19p-A310-9] Inverse Design of Low Back Reflection Grating Coupler

○Yuduan Wang[1], Tsuyoshi Horikawa[1], Ohiso Yoshitaka[1], Tomohiro Amemiya[1], Nobuhiko Nishiyama[1,2,3] （1.Tokyo Tech., 2.IIR, 3.PETRA）

3:45 PM - 4:00 PM

▲[19p-A310-10] Morphology dependent shape resonances by optical fiber encaved nanoantenna for refractive index sensing

○(D)Jasleen Kaur[1,2], Kaushal Vairagi[1,2], Samir K Mondal[1] （1.Micro &Nano-optics Centre, CSIR-Central Scientific Instruments Organisation, Chandigarh 160030, India, 2.Academy of Scientific and Innovative Research (AcSIR), Ghaziabad-201002, Uttar Pradesh, India）

4:00 PM - 4:15 PM

▲[19p-A310-11] AlN Stressor Layer for Ge-on-Si Photonic Devices

○Jose Alberto Piedra[1], Shohei Kaneko[1], Takaaki Fukushima[1], Keisuke Yamane[1], Junichi Fujikata[2], Yasuhiko Ishikawa[1] （1.Toyohashi Univ. Tech., 2.Tokushima Univ.）

4:15 PM - 4:30 PM

▲[19p-A310-12] Radius Optimization of SoI Rectangular Waveguide based Optical Power Splitter and Combiner

○(B)Wridheeman Bhattacharya[1], Devansh Srivastava[1], Ritu Raj Singh[2] （1.Indian Institute of Information Technology Ranchi, Jharkhand, India, 2.Netaji Subhas University of Technology, Delhi, India）

4:30 PM - 4:45 PM

▲[19p-A310-13] Wavelength Independent Coupling Length Variation analysis using Silicon on Insulator based Rectangular Waveguide for Coupler/Splitter Application

○(DC)SHALINI VARDHAN[1], RITU RAJ SINGH[1] （1.Department of Electronics and Communication Engineering, Netaji Subhas University of Technology, Delhi, India）

4:45 PM - 5:00 PM

Video-rate Spectral Imaging Chip based on Metasurfaces

Yidong Huang, Kaiyu Cui, Jian Xiong, Jiawei Yang

Department of Electronic Engineering, Tsinghua University, Beijing, China

E-mail: yidonghuang@tsinghua.edu.cn

Spectral imaging extends the concept of traditional color cameras to capture images across multiple spectral channels, and is widely used in many fields such as remote sensing, precision agriculture, biomedicine, environmental monitoring and astronomy. Conventional spectral cameras based on scanning methods suffer from low acquisition speed, large volume and high cost.

On-chip spectral imaging based on broadband modulation of metasurfaces and computational spectral reconstruction provides a promising scheme for the realization of consumer portable spectral cameras. In this work, a ultraspectral imaging chip is demonstrated based on freeform shaped metasurfaces[1,2]. Benefiting from the capability of multiplexing and reconfiguration of the metasurface supercell, the chip has an overall size of only 0.5 cm^2 with integrating more than 150,000 micro-spectrometers. The spectral imaging chip operates in the visible band of 450-750 nm, and the resolution of double peaks is as high as 0.5 nm. Using this real-time ultraspectral imaging chips, the dynamic changes of the characteristic spectrum of hemoglobin and its derivatives in the vivo rat brain were measured [1]. This technology can be further used to derive the activity of neurons in the brain through the mechanism of neurovascular coupling. Furthermore, rapid spectral imaging was realized for the driving scene combining deep unfolded neural network with a video-rate of 36 frames per second, which is expected to solve the problem of metamerism recognition in the automatic driving scene. These results show great potential in applications such as machine vision, industrial process control and other fields of real-time sensing.

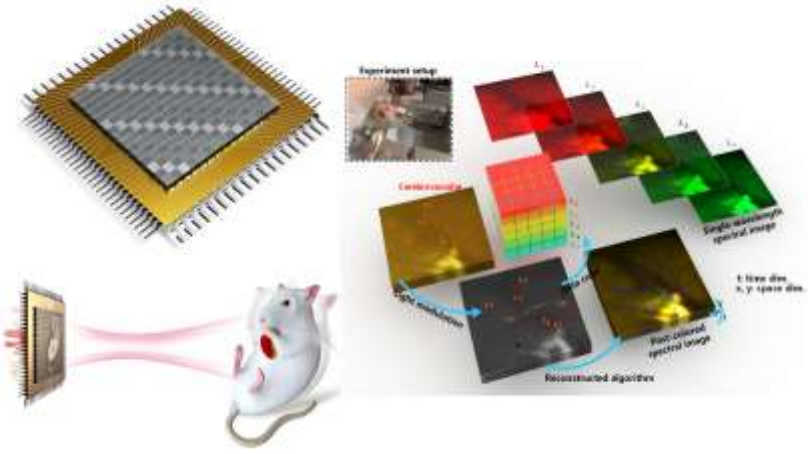

Figure Spectral imaging chip based on metasurfaces and the brain spectral image of a vivo rat.

[1] Xiong, J. et al., *Optica* **9**, 461-468 (2022)
[2] Yang, J. et al., *Laser & Photonics Reviews* **16**, 2100663 (2022)
[3] Yang, J. et al., *Chip*, 100045, (2023)

Low temperature annealing for vanadium dioxide in photonic integrated circuits

Yuxin Du,[1] Kai Sun,[1,2] Zihang Zheng,[1] Cornelis H. de Groot[1] & Xu Fang[1*]

[1]*School of Electronics and Computer Science, Univ. of Southampton, Southampton SO17 1BJ, UK*

[2]*School of Physics and Astronomy, Univ. of Southampton, Southampton SO17 1BJ, UK*

E-mail: x.fang@soton.ac.uk

Abstract: We show at the annealing temperature of vanadium dioxide (VO_2) fabricated using atomic layer deposition can be suppressed to 300 °C, significantly improving the compatibility of VO_2 with photonic integrated circuits.

The solid-state phase transition of VO_2 occurs at approximately 68 °C, significantly lower than other phase transition materials and phase change materials. This phase transition can be trigger by various external stimuli [1], and it is accompanied with a large change in the material's optical properties. These factors have made VO_2 a very attractive materials for optical and optoelectronic data processing. For example, we have recently numerically demonstrated that a VO_2-based microring resonator can mimic the classical conditioning observed in biology. For these emerging thin film- or nanostructure-based applications, atomic layer deposition is frequently the method of choice. Nevertheless, as-deposited VO_2 thin films are amorphous and require high-temperature annealing, a process that is often incompatible with photonic integrated circuits. In this work, we show that high-quality VO_2 thin films can be obtained with a low annealing temperature of 300 °C. This temperature can be tolerated by most photonic integrated circuits, and represents an important technical step in the development of VO_2-based computing circuits.

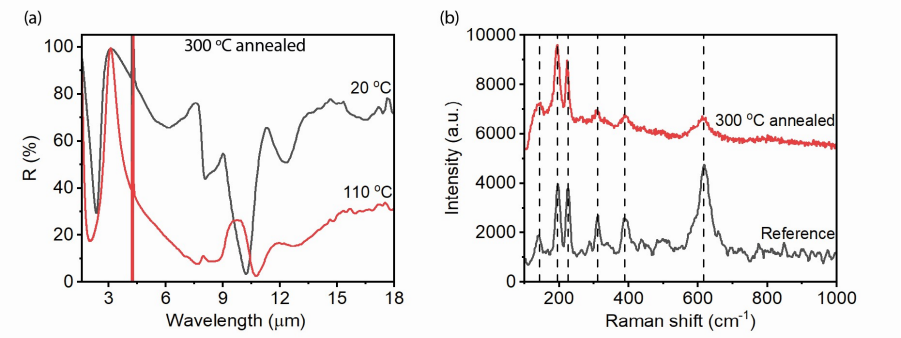

Fig. 1. Properties of a VO_2 thin film. The film was deposited using atomic layer deposition, and then annealed under an oxygen pressure of 2.5 Torr for 3 hours at 300 °C. (a) The reflection of the thin film shows a large contrast between the insulating phase (20 °C) and the metallic phase (110 °C). (b) Its Raman spectrum also shows pronounced VO_2 peaks that align with a reference sample.

References: [1] H. Takeya *et. al.*, "Bolometric photodetection using plasmon-assisted resistivity change in vanadium dioxide," Scientific Reports 8, 12764 (2018). [2] K. Sun *et. al.*, "Room Temperature Phase Transition of W-Doped VO_2 by Atomic Layer Deposition on 200 mm Si Wafers and Flexible Substrates," Advanced Optical Materials 10, 2201326 (2022).

Hybrid silicon all-optical switching devices integrated with two-dimensional materials

○D. Yamashita[1,2], N. Fang[3], S. Fujii[1,4] and Y. K. Kato[1,3]

[1]*Quantum Optoelectronics Research Team, RIKEN Center for Advanced Photonics, Saitama 351-0198, Japan*
[2]*Platform Photonics Research Center, National Institute of Advanced Industrial Science and Technology (AIST), Ibaraki 305-8568, Japan*
[3]*Nanoscale Quantum Photonics Laboratory, RIKEN Cluster for Pioneering Research, Saitama 351-0198, Japan*
[4]*Department of Physics, Faculty of Science and Technology, Keio University, Kanagawa 223-8522, Japan*
E-mail: daiki.yamashita@aist.go.jp

Silicon photonics has garnered attention as a platform for photonic integrated circuits (PICs), which monolithically integrates electronic and photonic devices in a same chip. On-chip all-optical switching is an essential component for the PICs. Fast and energy efficient all-optical switches based on microcavites have been demonstrated, and currently, the performance is limited by the substrate material which is silicon [1]. The use of III-V semiconductors [2] and organic molecules [3] as substrate materials has circumvented this limitation and high-performance switching has been reported, however the inability to fabricate directly on silicon substrates is a major problem in various aspects such as monolithic on-chip integration and cost reduction.

Here we propose hybrid all-optical switching devices that combine silicon nanocavities and two-dimensional semiconductor materials. By exploiting the refractive index modulation caused by photo-induced carriers in the two-dimensional material instead of the silicon substrate, we have overcome the limit of switching speed restricted by the carrier lifetime of silicon. Air-mode photonic crystal nanobeam cavities capable of efficient interaction with two-dimensional materials are fabricated [4], and molybdenum ditelluride, a two-dimensional material with a rapid carrier recombination, is transferred onto the cavities. A thin molybdenum ditelluride flake loaded on a cavity is excited by an optical control pulse to shift the resonant wavelength of the cavity for switching operation. We have successfully implemented a high-speed (~30 ps) all-optical switching with low-excitation energy (~500 fJ). The switching speed has improved by approximately 10^2 times compared to devices without two-dimensional materials.

This work is supported in part by JSPS (KAKENHI JP22K14624, JP22K14625, JP20H02558, JP23H00262, JP20K15199, JP20J00817), and MEXT (ARIM JPMXP1222UT1137). N.F. is supported by RIKEN Special Postdoctoral Researcher Program.

References

[1] T. Tanabe, K. Nishiguchi, A. Shinya, E. Kuramochi, H. Inokawa, M. Notomi, K. Yamada, T. Tsuchizawa, T. Watanabe, H. Fukuda, H. Shinojima, and S. Itabashi, Appl. Phys. Lett. 90, 031115 (2007).
[2] K. Nozaki, T. Tanabe, A. Shinya, S. Matsuo, T. Sato, H. Taniyama, and M. Notomi, Nat. Photon. 4, 477–483 (2010).
[3] X. Hu, P. Jiang, C. Ding, H. Yang, and Q. Gong, Nat. Photon. 2, 185–189 (2008).
[4] N. Fang, D. Yamashita, S. Fujii, K. Otsuka, T. Taniguchi, K. Watanabe, K. Nagashio, Y. K. Kato, Adv. Opt. Mater. 10, 2200538 (2022).

Grating Diffraction Select Radial Mode at the Inner Active Cladding of Hybrid-Cavity Microlaser

Jinghan Chen[1], Adrian Abazi[2,3], Alexander Eich[2,3], Yoshitaka Tomishige[1], Harunobu Takeda[1], Yuya Mikami[1]
Naoya Tate[1], Yuji Oki[1], Carsten Schuck[2,3], Hiroaki Yoshioka[1]

[1]Graduate School and Faculty of Information Science and Electrical Engineering, Kyushu University,
[2]Department for Quantum Technology, University of Münster
[3]Center for Soft Nano Science (SoN)
E-mail: chenjinghan@laserlab.ed.kyushu-u.ac.jp

1. Introduction

Miniaturized, tunable, on-chip lasers are crucial to developing photonic integrated circuits (PICs). Microrings, a common integrable laser, often exhibit multi-mode propagation that leads to unstable lasing. Researchers have integrated azimuthal gratings onto microrings to improve performance to realize single-mode lasing [1]. However, microring lasers with active semiconductor cores face challenges related to design flexibility and the need for precision in fabrication. We introduce a hybrid-cavity grating-integrated lasers, incorporating a Si_3N_4 microring and active polymeric cladding. This design simplifies fabrication and provides flexible gain choices for diverse wavelength lasing. The issue is the complexity of the mode due to the broad distribution of the active cladding. We demonstrate the generation and selection of radial modes from the grating diffraction at the inner active cladding. And the radial mode is partly coupled with whispering gallery modes (WGMs) propagating in the microring.

2. Methods

The structure and parameters of the active cladding grating integrated microring laser are as Fig. 1 shows. The Si_3N_4 grating-integrated microring structures were fabricated via electron-beam-lithography and reactive ion etching on a thermal SiO_2 on Si substrate. The active layer consists of a triazine-based hyperbranched polymer with a refractive index of 1.78, doped with Pyrromethene 597 dye.

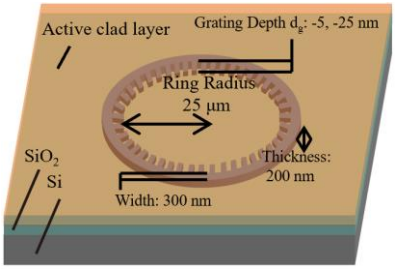

Fig.1 Structure and parameters of the microlaser.

3. Results and discussions

Figure 2(a) presents the excitation image of the microlaser, and Fig. 2(b) magnifies the diffraction pattern taken from Fig. 2 (a) after applying the Laplacian Gaussian filter. The grating is interpreted as a composite of second-order distributed feedback (DFB) grating segments. The radial diffraction generates and selects the radial mode at the inner active cladding as only the wavelength that meets the Bragg condition will be selected for DFB grating [2]. The spectra of Fig. 2(c) encompass two groups of modes, characterized by a free spectrum range of 1.72 nm and 1.15 nm, which are assigned to radial modes and WGMs, marked in red and green, respectively. For Fig. 2(d), the radial mode is modified by the diffraction grating, lasing along the stop band centered with the Bragg wavelength, and is partly coupled to the WGMs (coupling mode is marked in purple). That suggests a selection of radial mode from the grating diffraction.

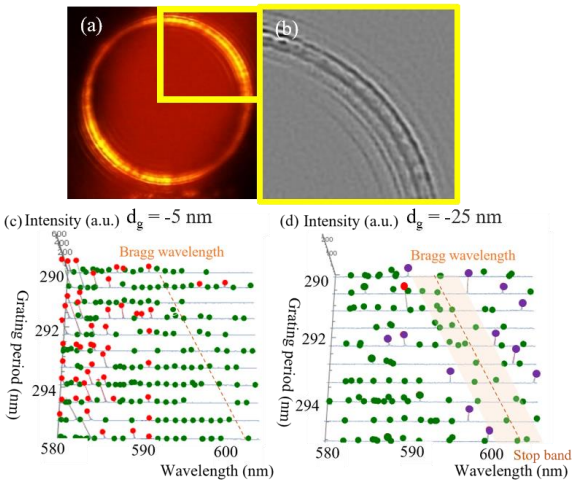

Fig.2 (a) excitation image of d_g -25 nm, (b) diffraction pattern enlarged from (a) after the Laplacian Gaussian filter, (c) spectra of the microlaser with d_g -5 nm, and (d) spectra of the microlaser with d_g -25 nm.

4. Conclusion

We have successfully fabricated active cladding grating-integrated microring lasers. We demonstrated that the radial mode was generated and selected from the grating diffraction condition at the inner active cladding under a sufficient grating depth. The radial mode is partly coupled to the WGMs propagating in the microring.

Acknowledgments

This work was supported by JST-CREST (JPMJCR20T4), JSPS KAKENHI Grant Number JP19KK0379. C.S. acknowledges support from the Ministry for Culture and Science of North Rhine-Westphalia (No. 421-8.03.03.02-130428).

References

[1] Arbabi, A., et al, Opt. Express. **23**.4 (2015) 5335-5347.
[2] Yariv, Amnon. IEEE J. Quantum Electron **9**.9 (1973) 919-933.

Gain Induced Dispersion Effects on Airy Pulse

Deependra Singh Gaur and Akhilesh Kumar Mishra
Department of Physics, Indian Institute of Technology Roorkee, Roorkee Uttarakhand India
Email: ds_gaur@ph.iitr.ac.in, akhilesh.mishra@ph.iitr.ac.in

Introduction

Semiconductor optical amplifiers (SOA) is an essential part in the modern long range optical communication system. SOA provides high gain over large bandwidth and consumes low power [1]. The study of optical pulse propagation inside SOA provides interesting insights [2,3]. Airy pulse, a self-accelerating pulse is known for its self-acceleration and quasi-dispersive nature [4]. In this work, we study the Airy pulse propagation in the linear regime of a SOA. We observe that peak value of the Airy pulse and trajectory of the Airy pulse depend upon the gain dispersion parameter of SOA.

Theoretical Model

The pulse propagation equation, which models the dynamics of the optical pulse in a SOA media is expressed as [2]

$$\frac{\partial U}{\partial z} = \frac{1}{2}(1 - i\alpha)g_0 \exp\left(-s\int_{-\infty}^{T}|U|^2 d\tau\right)\left(U + d^2\frac{\partial^2 U}{\partial T^2}\right), \quad (1)$$

where U, α and g_0 are pulse envelope, linewidth enhancement factor and small signal gain respectively. The parameter s is related to the input pulse energy E_{in} and saturation energy E_{sat} of the SOA. Gain induced dispersion parameter $d = T_2/T_0$ where T_2 is known as polarization relaxation time of two-level equivalent of SOA and T_0 is the input pulse width.

The input pulse envelope is expressed as

$$U(0,T) = Ai(T)\exp(aT), \quad (2)$$

where $Ai(T)$ represents the airy function and a is truncation factor.

Results

We study the role of gain induced dispersion on Airy pulse dynamics in linear regime of a SOA by considering the case where pulse energy remains below the saturation energy during amplification process. Therefore, we set $s = 0$ and solve eqn. (1) numerically as well as theoretically. The functional form of the Airy pulse, after z distance of propagation, is expressed as eqn. (3), which reveals that amplitude of the Airy pulse grows with the propagation distance whereas the argument of the Airy pulse $(T + b^4 - a^2)$ demonstrate that pulse trajectory expression depends upon the linearly and quadratically on propagation distance. For small values of d and z, linear term dominates, and pulse follows linear path while the path becomes curved with increasing value of d and z. The output pulse at $z = 10$ cm is shown in fig. 1 (a) and the peak gain value is shown in fig. 1 (b).

$$U(z,T) = \exp\left[\frac{(1 - i\alpha)g_0 z}{2}\right]Ai(T + b^4 - a^2)\exp\left[\frac{2}{3}b^6 - a^2b^2 + b^2T + \frac{a^3}{3}\right] \quad (3)$$

where $b^2 = a + \frac{1}{2}(1 - i\alpha)d^2 g_0 z$, and $b^4 = a^2 + ad^2 g_0 z + \frac{1}{4}d^4 g_0^2 z^2 - \frac{1}{4}\alpha^2 d^4 g_0^2 z^2 - i\alpha a d^2 g_0 z - \frac{i}{2}\alpha d^4 g_0^2 z^2$.

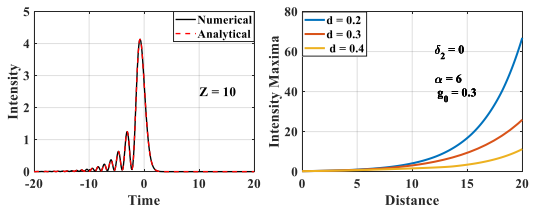

Fig. 1 Airy pulse propagation in SOA with $\alpha = 6$, $d = 0.2$ and $g_0 = 0.3$ cm^{-1}, (a) Input and output profiles of the pulse, (b) Intensity peak variation with propagation distance for different values of d.

Conclusion

We have shown that peak gain of the Airy pulse in SOA is large for small value of d whereas the trajectory of the pulse depends upon the propagation distance and gain dispersion parameter d.

References

1. A. E. Bednyakova, D. Khudozhitkova, A. Kokhanovskiy, and S. K. Turitsyn, "Nonlinear spectral blueshift in semicondutor optical amplifiers" Opt. Lett. 46, 4754-4760, 2021
2. G. P. Agrawal, "Effect of Gain Dispersion on Ultrashort Pulse Amplification in Semiconductor Laser Amplifiers" IEEE J. of Quantum electronics 27 (1991)
3. A. K. Mishra, O. Karni and G Eisentein, "Coherent control in quantum dot gain media using shaped pulses: a numerical study" Opt. Express 23, 29940-29953 (2015)
4. D. S. Gaur and A. K. Mishra, "Impact of harmonic potential induced nonlinearity on Airy pulse" J. Opt. 24 (2022)

Electric Field-Induced Mode Switching in Few-Mode Fibers

Isha Sharma[1], Partha Roy Chaudhuri[1*]
[1] Department of Physics, Indian Institute of Technology Kharagpur-721302, India
*email : roycp@phy.iitkgp.ac.in

1. INTRODUCTION

In the past few years, there has been a lot of R&D attention in developing optical fiber based technologies in photonics and broadband communication system. Data communication, cloud computing has demanded an exponential growth in communication traffic. To overcome it, few-mode fibers and mode division multiplexing (MDM) has emerged as a favorable solution. Mode convertors play a crucial role as key components in MDM systems. Numerous types of mode convertors have been proposed and experimentally demonstrated so far, employing diverse techniques such as acoustooptic transducers, structured optical waveguides etc. [1].

We devised an all fiber configuration for selective excitation and switching between higher order modes excited in a few-mode fiber. In our previous research, we introduced a novel approach based on cantilever beam deflection techniques for sensing the surrounding electric field [2]. We conducted a series of experiments to investigate and validate the effectiveness of this method. Now, we implement our cantilever technique to achieve the switching between higher order modes based on introducing a controlled perturbation offset in the input launching conditions. We coat the fiber with $BiFe_{0.9}Co_{0.1}O_3$ as probe sample and placed it in an electric field.

II. EXPERIMENTAL DETAILS AND RESULT

The experimental setup for mode switching is illustrated in Fig. 1. The setup includes an input He-Ne laser source. The light is coupled into one end of a single-mode fiber (SMF) using a light coupling unit. The other end of the SMF is coated with our probe material (coated length 1.0 cm with coated thickness of 0.36 mm). A four-mode fiber (FMF) is positioned head-on with respect to the exit of the input cantilever fiber, placed between two electric field plates. Under the influence of an electric field, the coated fiber undergoes deflection due to the induced polarization of the probe sample. This deflection leads to modulation of the input launching conditions, thereby altering the mode excitation within the fiber resulting in the switching of the output mode. To begin the experiment, we couple the light emitted from the SMF into the FMF using a mechanical butt coupling method. By bringing the fibers into close proximity, we establish a near-ideal alignment that facilitates the desired mode excitation corresponding to LP_{02}. On applying the electric field, we observe the phenomenon of mode switching within the FMF. Figure 2 visually illustrates the mode profiles and their transformations as the electric field is applied, for cases with varying plate separations. In this case, switching between circularly symmetric mode to azimuthal asymmetric mode is taking place.

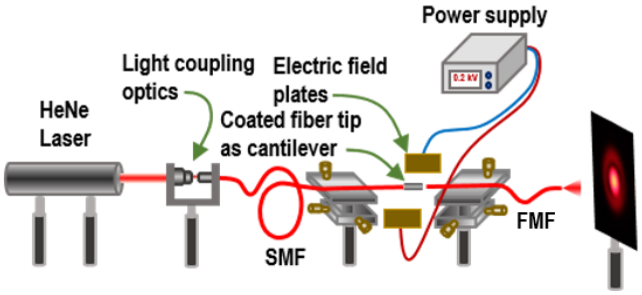

Fig. 1. Schematic of experimental set-up.

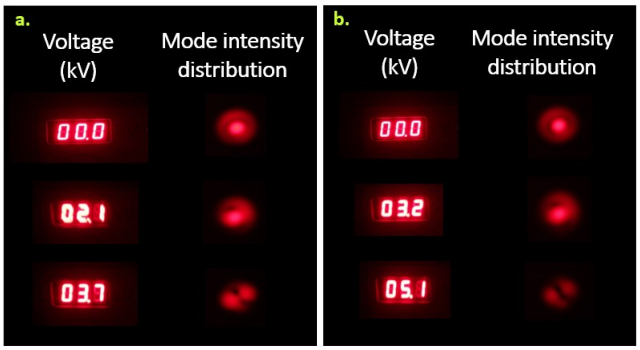

Fig.2. Real time monitoring of mode intensity distribution at different voltage values at fiber exit for varying plates distance at (a) 1.4 (b) 1.9 cm.

III. CONCLUSIONS

We introduce a novel method for achieving mode switching within a few-mode fiber by utilizing an electric field in a fiber-to-fiber transmission setup. This approach offers a means to achieve dynamic and controllable mode manipulation based on the electric field-induced deflection of the coated fiber, presenting opportunities for various applications in sensing, communications, and beyond. Also, by fine-tuning of experimental parameters, we can enhance the sensitivity of the system. Furthermore, our all-fiber setup offers several advantages due to its inherent characteristics, including light weight, safety, flexibility, immunity to electromagnetic interference etc.

IV. REFERENCES

[1] A. K. Memon, and K. X. Chen, Opto-Electronics Review, 29 (2021).
[2] Isha Sharma, Partha Roy Chaudhuri, Optical Fiber Technology, 62 (2021) 102472

Shifting zero-dispersion wavelength of silica-dielelctric Bragg fiber

Saikat Mondal[1], Partha Roy Chaudhuri[1]
Department of Physics, Indian Institute of Technology, Kharagpur, India
E-mail: roycp@phy.iitkgp.ac.in

I. INTRODUCTION

The coaxial Bragg fiber inherently gives the freedom of multi-parameter tailoring to achieve desired transmission properties, [1], which in turn, enables one to control the propagation characteristics, namely, group velocity dispersion (GVD), zero dispersion wavelengths (ZDW).

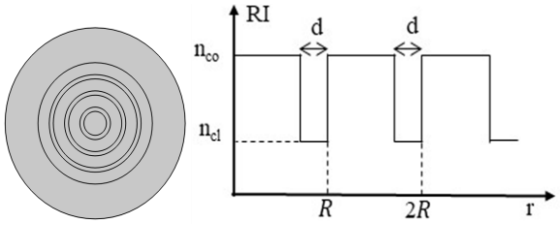

Figure-1: Schematic diagram of the cross-section of Bragg fiber and refractive index profile.

Bragg fibers are studied with air-silica structure [2]. We, however, studied silica-dielectric layered structure and focused on how the dispersion curve behaves by the varying the transverse geometry.The schematic cross-section of the fiber is shown in Fig.1, where the inner core silica is surrounded by alternatelayers of low refractive index dielectric medium and silica. We take the value ofn_{co} = 1.4438 and n_{cl} = 1.025 (Al_2O_3 thin film) for our analysis with varying inner core radius for the Bragg fiber.

II. ANALYSIS AND RESULTS

To determine the waveguide dispersion of the fiber we used finite element method (FEM) in COMSOL Multiphysics, using perfectly matched layer (PML). We calculated the fundamental guided mode yielding the effective mode-index and then wecomputed waveguide dispersion (D_w) and material dispersion (D_m) [3]. To calculate D_w we have not considered the wavelength dependence of refractive index profile, rather we have used Sellmeier equation to compute D_w[3]. We have evaluated the wavelength dependence dispersion curve for different combinations of 'R' and 'd' parameters.

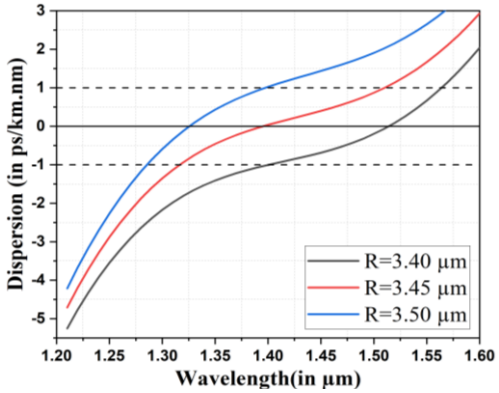

Figure-2: Dispersion curve for different combination of R and constant d=0.12 μm

We show that by varying the 'R' parameter, the ZDW can be shifted to near infrared region. A typical result is shown in Fig.2 for which we kept$d = 0.12\mu m$ in our calculation while by changing the 'R' value we obtained the zero dispersion wavelengths (ZDWs) of 1.52 μm, 1.40μm and

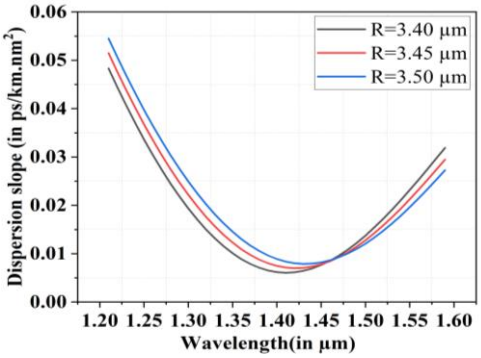

Figure-3: Dispersion slope

1.32μm for R = 3.40μm, 3.45μm and 3.50μm, respectively. We have also calculated the dispersion slope which is shown in Fig.3.These lower values of the slopes reveal the nature of flatness near the ZDW. The obtained parameters are tabulated in table 1.

Table 1

R (μm)	ZDW (μm)	Dispersion slope at ZDW (ps /km-nm²)	Flat wavelength band (μm) for dispersion interval 0±1 ps/km.nm²
3.40	1.52	0.015	0.11
3.45	1.40	0.007	0.19
3.50	1.32	0.020	0.12

III. CONCLUSION

We have studied the dispersion propertiesof the coaxial Bragg fiber as a function of wavelength with varying geometrical parameters of the fiber in the range of 1.2 μm to 1.60 μm. We obtained a few hundreds of nanometer band in the region of 0±1 ps/km.nm dispersion interval.

REFERENCES

[1] F. Begum, I. K. Yakasai, E. Abas, J. Zaini, I. Petra and A. K. Azad, "High nonlinear coefficients of photonic crystal fiber with ultra-flattened chromatic dispersion," 7th Brunei International Conference on Engineering and Technology 2018 (BICET 2018, pp. 1-4.

[2] Juan A. Monsoriu, Enrique Silvestre, Albert Ferrando, Pedro Andrés, and Juan J. Miret, "High-index-core Bragg fibers: dispersion properties," Opt. Express 11, 1400-1405 (2003)

[3] M. Seifouri, M. M. Karkhanehchi, and S. Rohani, "Design of Multi-Layer Optical Fibers with Ring Refractive Index to Reduce Dispersion and Increase Bandwidth in Broadband Optical Networks", *Eng. Technol. Appl. Sci. Res.*, vol. 2, no. 3, pp. 216–220, Jun. 2012

[4] Ghatak, A., & Thyagarajan, K. (1998). Material dispersion. In *An Introduction to Fiber Optics* (pp. 78-96). Cambridge: Cambridge University Press. doi:10.1017/CBO9781139174770.

Beam Steering with Integrated Optical Phased Array using DNN

Makoto Nakai, Isamu Takai

Toyota Central R&D Labs., Inc.

E-mail: m-nakai@mosk.tytlabs.co.jp

1. Introduction

Integrated optical-phased-array (OPA) has drawn significant attention due to the potential use in wide range of applications, such as LiDAR (Light Detection and Ranging) and free space communication. Beam emitted from OPA is electronically steerable by controlling the phase of light entering the antenna array [1]. During the fabrication process, the device dimension and waveguide sidewall roughness apt to change within the OPA circuit. This shifts the phase of light entering each antenna, resulting in a phase error. To prevent the distortion of the emitted beam, a look-up table of phase modulation voltage (PM-voltage) is prepared for each beam angle. Another factor which distorts beam is the change of chip temperature, which shifts the refractive index. In an environment which temperature changes rapidly, a look-up table for each angle and temperature will be required, resulting in a massive amount of calibration work. In this work, deep neural network (DNN) is used to predict the PM-voltage which controls the phase modulators to form a desired far field pattern (FFP).

2. System Configuration and Method

Fig. 1 shows the schematic of the proposed system. The DNN model is designed by 7 fully connected layers (FCL), with batch normalization (BN). Training and prediction of the DNN model was operated in a personal computer. The trained DNN will predict the PM-voltage to form the input Desired FFP. The predicted PM-voltage will be applied to the OPA circuit to drive the phase modulators through a printed circuit board. The OPA circuit was designed to operate at transverse electric (TE) mode with wavelength of 1550nm. Thermo-optic modulators were utilized to modulate the phase of each antenna. The antenna was designed to emit equivalent power along the longitudinal direction with the length of 1.1mm. Total of 128 antennas are aligned in an array with the pitch of 1.4μm. The emitted beam was measured with FFP camera mounted on top of the OPA circuit. The temperature of the OPA circuit was controlled with a Peltier device to maintain 45°C for initial demonstration to prove the proposed concept.

The DNN was trained with a set of randomly set PM-voltage values and measured FFP. The predicted PM-voltage values are compared with the actual randomly set PM-voltage values, and the parameters of the DNN are updated to minimize the difference.

3. Results

FFP with single peak were inputted into the DNN. Fig. 2 shows the measured FFP controlled with the predicted PM-voltage for 9 different arbitrary angles, each with different color, within -25deg. to +25deg. Each beam forms a peak at the designed angle. Small emissions at angles other than the designed angle are observed due to thermal crosstalk between modulators. These emissions are assumed to be suppressed by improving the OPA circuit design in future work.

4. Conclusion

OPA beam forming was proposed and demonstrated utilizing DNN as controller of the phase modulator. The proposed system forms beam at arbitrary angle within the 50° FoV.

[1] S. Chung *et al.*, “Optical phased-array FMCW LiDAR with on-chip calibration,” in IEEE ISSCC (IEEE, 2021), paper 19.1

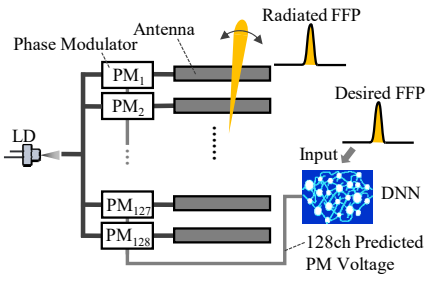

Fig. 1. Schematic of the proposed system with OPA circuit controlled with DNN.

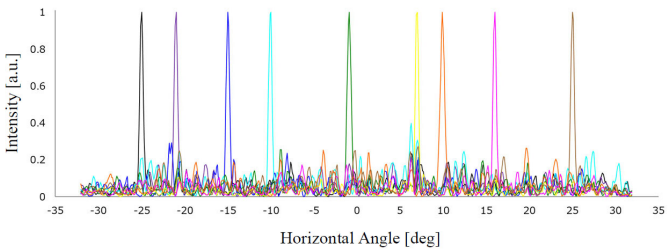

Fig. 2. Single peak beam formed with predicted PM-voltage.

Inverse Design of Low Back Reflection Grating Coupler

Yuduan Wang[1], Tsuyoshi Horikawa[1], Yoshitaka Ohiso[1], Tomohiro Amemiya[1] and Nobuhiko Nishiyama[1,2,3]

1 Dept. of Electrical and Electronic Engineering, 2 Institute of Innovative Research (IIR), Tokyo Institute of Technology

3 Photonic Electronics Technology Research Association (PETRA)

E-mail: wang.y.br@m.titech.ac.jp

Introduction

Grating couplers (GC) on silicon-on-insulator (SOI) have an excellent interconnectivity between photonic integrated circuit (PIC) device and fibers. Traditional theory-first hand-turning design method by sweep parameters is time-consuming to perform. In contrast, the target-first inverse design optimization algorithm enables obtaining the best solution in just a few iterations [1]. Although such inverse design was already applied to GC, only transmission characteristics was considered as the target. However, back-reflection is also critical for PICs, especially the lasing performance of semiconductor lasers [2]. In this work, we report Figure of Merit (FoM) dependance of the coupling efficiency as well as back-reflection of GC.

Result

First, the gradient-based optimization requires finding a suitable initial condition [1]. Fig.1 shows the model to initial inverse design structure which contains the design parameters be the starting position of the grating (x_0), the width of the pitch (=580 nm), and the duty ratio of each grating (95%). Using FDE and FDTD solver to determine the initial linearly apodized grating based on the defined optimization parameters (central wavelength = 1550 nm, fiber angle =10°). Here, the number of gratings is fixed at 25 and the etched depth at 80 nm, they are changeable for farther calculation.

Intel Xeon(R) Gold 6242R CPU with 512 GB RAM PC was used for calculation. 2 FOM monitors to optimize coupling efficiency (fom_coupl) and back reflection (fom_back) were set as shown in Fig.1. The optimizing wavelength was set to be only at 1550 nm and the convergence condition was set to 1e-5. Fig. 2 shows the calculated results of grating couplers with only maximized coupling efficiency (1 FoM) and 2 FoM. The back reflections at 1550 nm are -35.94 dB and -47.45 dB respectively and the coupling efficiencies are 66.02% and 66.00% respectively, which successfully minimum the back reflection and almost don't influence the perform of coupling efficiency. Since we set the optimizing wavelength as 1550 nm, only the point at 1550 nm meets good reflection value. In the future, we will set the range of optimizing wavelength to cover whole C-band wavelength. Fig.3 shows 9 grating etching trenches from left side, since the width at each trench gets wider as the grating number increase toward right side, when calculate 2 FoM, trench widths are overall smaller than 1FoM.

After this calculation, several trench widths became even less than 50 nm which maybe too narrow to fabricate. To get the manufacturable structure, restraint condition of the minimum feature size was set to be 100 nm. Fig.4 shows the results. The back reflections at 1550 nm are -32.00 dB and -39.70 dB, respectively, and the coupling efficiencies are 66.00% and 65.46%, respectively. The calculation of 1FoM costs about 2 h20 min, 2FoM costs about 3 h50 min.

Acknowledgment

This work was financially supported by NEDO (JPNP16007) and ARIM (JPMXP1222IT0025 and JPMXP1223IT0005).

Reference

[1] Logan Su et al., Opt.Express, vol. 26, no. 4, pp. 4023–4034, 2018.

[2] Takeda et al., Opt Express. 2014 Apr 7;22(7):8451-9.

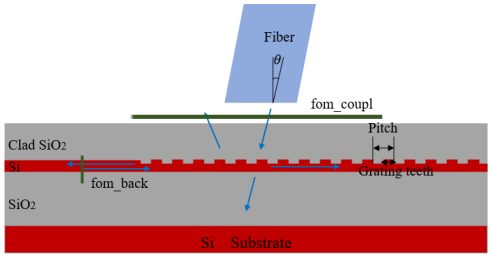

Fig.1 Model for Inverse Design Initialization

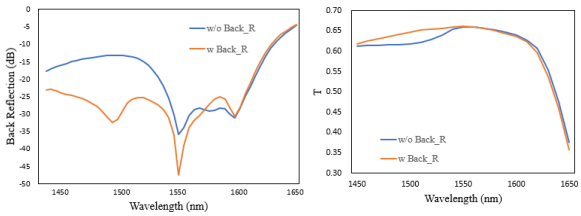

(a) Back Reflection (b) Coupling Efficiency

Fig.2 Result of Grating Coupler without Fabrication Constrain

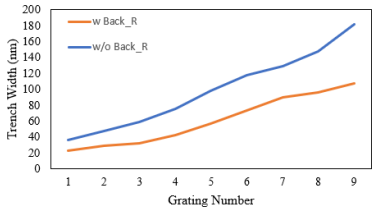

Fig.3 Trench Width of Designed Structure

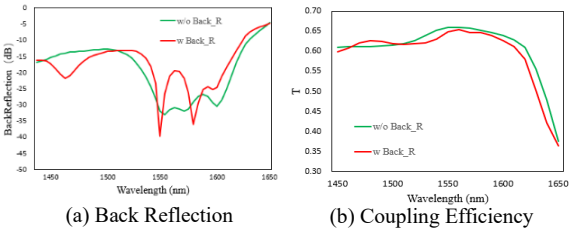

(a) Back Reflection (b) Coupling Efficiency

Fig.3 Result of Grating Coupler with Fabrication Constrain

Morphology dependent shape resonances by optical fiber encaved nanoantenna for refractive index sensing

Jasleen Kaur [1,2], Kaushal Vairagi [1,2], Samir K Mondal[2]
[1]Academy of Scientific and Innovative Research (AcSIR), Ghaziabad-201002, Uttar Pradesh, India
[2]Micro & Nano-optics Centre (μ-NOC), CSIR-Central Scientific Instruments Organisation, Chandigarh 160030, India
E-mail: samir_mondal@csio.res.in

Abstract: We present the numerical study to demonstrate excitation of morphology dependent resonances in microresonator by an encaved nanoantenna surrounded by conical cavity in an optical fiber. The microresonator is excited by a focused beam coming from the nanoantenna when placed off-axially to it. The resonances show Lorentzian and Fano peaks having Quality factor, Q of the order of ~10^5. The proposed design can be experimentally fabricated by chemical etching of a photosensitive fiber. The design has potential to sense the change in dielectric environment having sensitivity ~31.832nm/ RIU.

When a highly symmetric dielectric resonator exhibits the optical scattering phenomena known as morphology dependent shape resonances (MDSR), electromagnetic energy is trapped inside the structure at specific ratios of refractive index and radius. As per Van de Hulst's principle the maximum excitation is observed when the focal point of excitation just lies at the proximity of the edge of resonator[1]. The photons overcome the potential barrier provided by the resonator, just like electrons do in a quantum mechanical resonance, and tunnel through their forbidden area[2]. We here introduce a novel integrated experimental configuration to excite MDSR by a nanoantenna encaved inside a conical cavity in an optical fiber tip. The said design is fabricated by chemical etching of a photosensitive optical fiber by 48% of Hydrofluoric acid. The cleaved end of the fiber is made to touch the meniscus of acid and the different etching rates of core and cladding aids in formation of required optical fiber tip, Fig 1(a). The nanoantenna have the potential to produce a focused beam of FWHM ~ 3μm at distance ~25μm from nanoantenna. The conical cavity provides a platform for holding the microresonator and helps with resonator positioning relative to axial position of nanoantenna. Experimentally, the developed probe has shown Q-factor ~10^5 for a Barium titanate resonator having diameter 15μm. We have performed numerical simulations in COMSOL Multiphysics of the same design to explore refractive index sensing application. Fig 1b shows the trapped electromagnetic energy inside a microresonator and the simulated electric field v/s wavelength results suggest that the configuration shows a redshift when the refractive index (RI) of surroundings of resonator is changed, Fig 1c. A sensitivity of the order of ~31.832 nm/RIU is observed.

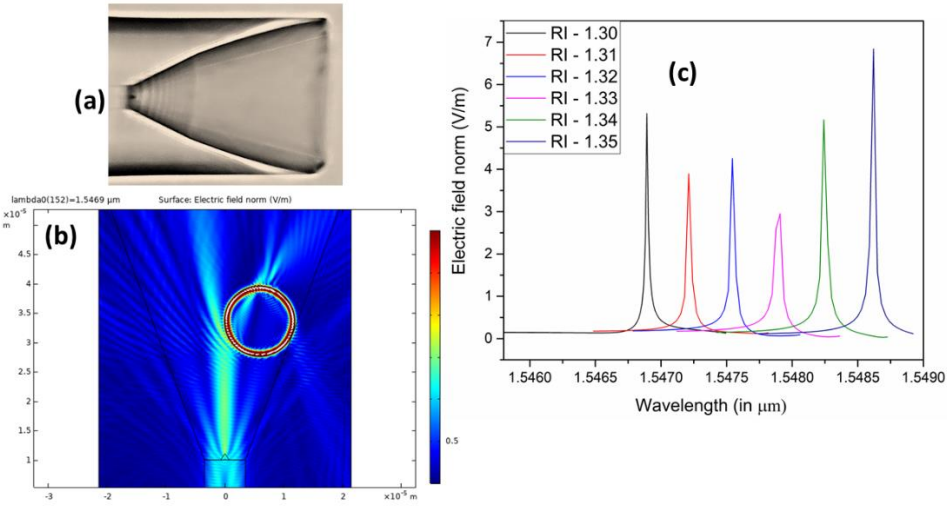

Fig 1 (a) Microscopic image of encaved nanoantenna in an optical fiber tip(b)Simulation result showing electric field distribution inside the barium titanate resonator of diameter 15μm (c) Simulation showing redshift with the change in refractive index around the resonator.

References

1. Barton, J. P., Alexander, D. R. & Schaub, S. A., *J. Appl. Phys.* **65,** 2900–2906 (1989).
2. Marmolejo, J. T., Canales, A., Hanstorp, D. & Méndez-Fragoso, R., *Phys. Rev. Lett.* **130,** 1–6 (2023).

AlN Stressor Layer for Ge-on-Si Photonic Devices

Toyohashi Univ. Tech. [1], Tokushima Univ. [2], ◦Jose A. Piedra-Lorenzana[1], Shohei Kaneko[1], Takaaki Fukushima[1], Keisuke Yamane[1], Junichi Fujikata[2], Yasuhiko Ishikawa[1]

E-mail: piedra.lorenzana.jose.alberto.ei@tut.jp, ishikawa@ee.tut.ac.jp

1. Introduction

In Si photonics, epitaxial Ge layers are required for photonic devices such as photodetectors (PDs) operating at near-infrared optical communicational wavelengths [1]. The lattice strain in Ge plays a significant role in the operating wavelengths of the devices. In the Ge layer on Si, an in-plane tensile strain is generated as high as 0.2% due to the thermal expansion mismatch with Si [2]. In this work, an AlN layer is studied as an external stressor to enhance the near-infrared absorption in Ge strip structures.

2. Sample preparation

Strip structures of Ge epitaxial layers were prepared by a selective chemical vapor deposition on a (001) Si substrate partially covered with 100-nm-thick SiO_2 masks. The width of the Ge strip ranged from 0.9 µm to 100 µm. A 300-nm-thick AlN layer was deposited on Ge by reactive RF magnetron sputtering at 200°C.

3. Experimental Results

To evaluate the lattice strain in the Ge strip covered with AlN, the Raman spectra were measured. Fig. 1 shows typical Raman spectra of the Ge strips with different widths. The observed peaks at around 300 cm^{-1} are derived from the Ge-Ge bonding. Compared to an unstrained bulk Ge at the bottom of Fig. 1, the peaks from the Ge strips showed negative shifts due to the tensile lattice strain. In the 100-µm-wide strip, equivalent to the blanket Ge film, the in-plain tensile strain was estimated as 0.21%. It is important that such a negative peak shift was maintained or slightly increased for the strips as narrow as 1 µm in contrast to the bare strips (not shown), which show a reduced negative shift due to the strain relaxation [3]. This indicates that the AlN layer acts as an external stressor to induce the tensile strain.

Fig. 2 shows typical photoluminescence (PL) spectra at around 1.55 µm, derived from the direct transitions in Ge. Compared to the 100-µm-wide strip, the 1.1-µm-wide one without the AlN layer showed a blue shift because of a strain relaxation [3]. On the other hand, the blue shift was suppressed by depositing AlN. The result supports that the AlN layer acts as an external stressor to potentially enhance the near-infrared absorption.

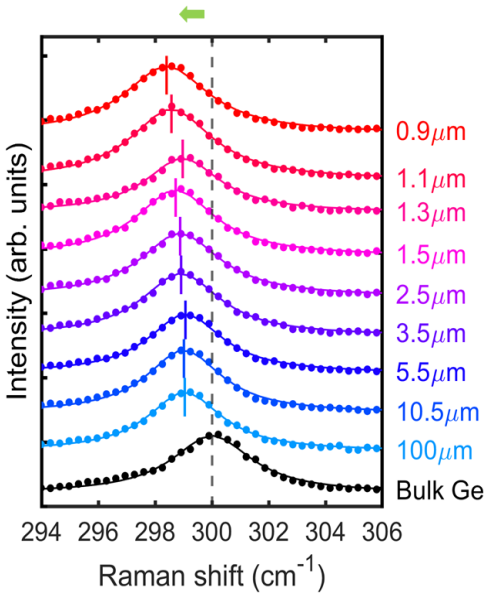

Fig. 1. Typical Raman spectra for different widths of the Ge strips covered with AlN.

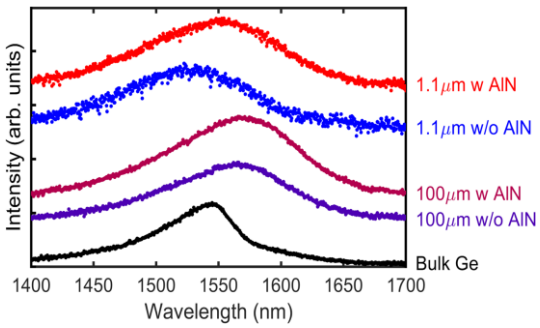

Fig. 2. Typical PL spectra at RT obtained for the 1.2- and 100-µm-wide Ge strips with and without the AlN overlayer.

4. Conclusion

The AlN layer on the Ge strip was studied as an external stressor. The Raman and PL spectra showed that the AlN layer acts as a stressor to induce the tensile strain.

References

[1] J. Michel et al., Nature Photon. **4**, 527 (2010).
[2] Y. Ishikawa et al., Appl. Phys. Lett. **82**, 2044 (2003).
[3] S. Sonoi et al., IEEE J. Quantum Electron. **58**, 8400209 (2022).

Radius Optimization of SoI Rectangular Waveguide based Optical Power Splitter and Combiner

Wridheeman Bhattacharya[1], Devansh Srivastava[1], Ritu Raj Singh[2]
[1]*Dept. of Electronics and Communication, Indian Institute of Information Technology Ranchi, Jharkhand, India.*
[2]*Dept. of Electronics and Communication, Netaji Subhas University of Technology, Delhi, India.*
rituraj.singh@nsut.ac.in

1. Introduction

Optical power splitters and combiners are crucial in broadband optical communication, suppressing active devices in passive optical networks. They enable Photonic Integrated Circuits (PICs) by creating specific photonic band gaps. Coupled Mode Theory (CMT) and FDTD methods analyze the coupling between Y-branch and parallel waveguides. Symmetrical power splitters 1x2 divide power equally, facilitating simple Y-branch or parallel waveguide branch designs [1], [2]. They are easy to fabricate and have low sensitivity to tolerances. Performance is evaluated based on transmittance and absorptance.

Neil et al. proposed his study in 1999 examined phase deviation and power splitting ratio in the Mach Zehnder Interferometer (MZI) [3]. Previously, MMI-based optical splitters and combiners gained attention [4], [5]. This paper aims mainly at the radius optimization for the 1x2 power splitter. Apart from CMT, FEM analysis is used to study the losses in conventional splitters based on rectangular silicon-on-insulator (SoI) waveguide structures.

2. Structure

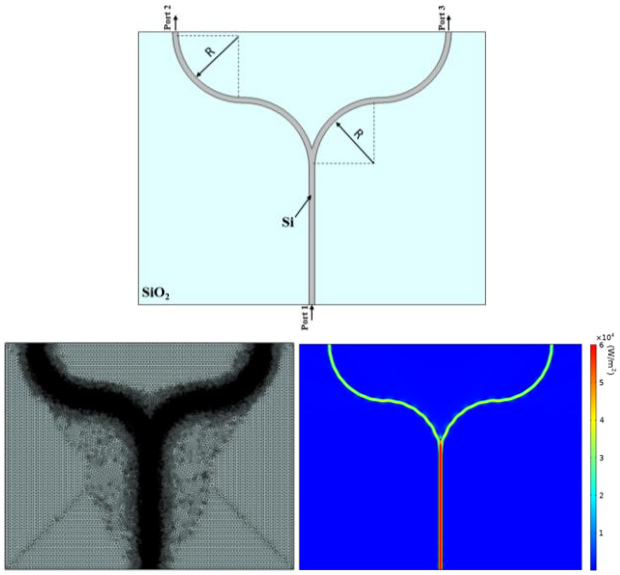

Fig. 1. (a) Schematic diagram; (b) Structured triangular mesh; and (c) Poynting vector

The 1x2 optical power splitter has been designed in COMSOL Multiphysics software as shown in Fig. 1(a). The input port is shown as Port 1, and the output ports as Port 2 and Port 3. Silicon is acting as the material for the splitter working in the SiO_2 environment. Radius optimization has been performed along the power splitter curves, thus showcasing its efficiency. Fig. 1(b) shows the structure with fine meshing to enable accurate simulation with efficient results. Fig. 1(c) demonstrates the intensity propagation of the power splitter, which further demonstrates that power is being divided into its two arms equally with minute losses.

3. Result and Discussion

The range of radius optimization was taken from 0 to 50 µm with a resolution of 0.01 µm. Figure 2(a) shows the comparison analysis of absorptance with respect to radius. The value of absorptance decreases with increasing radius. Figure 2(b) shows the analysis of transmittance at output ports 2 and 3 with respect to radius which demonstrates that transmittance increases with increasing radius. At a radius of 20 um, it is observed that both transmittance and absorptance saturate, giving us a result, that 20 um is the optimized radius for the power splitter to act in its most efficient state.

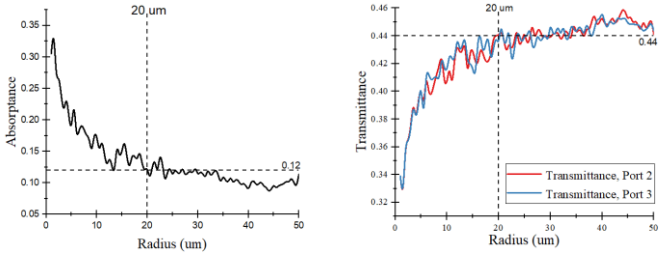

Fig. 2. (a) Absorptance; and (b) Transmittance at output ports.

4. Conclusion

The above analysis demonstrates radius optimization for the optical power splitter and combiner. It can be observed that the absorptance decreases with increasing radius and transmittance increases with increasing radius. A radius 20 um is obtained as the optimized value of radius for which both the transmittance and absorptance saturates thus leading to the conclusive fact of the splitter working at its most desirable efficient state at this optimized radius.

Reference

[1] D. Srivastava, S. Vardhan, and R. R. Singh, "SoI Based Optical 1 × 2 Wavelength Independent 3-dB Power Splitter Design Using Three Rectangular Cross-Sectional Cuboidal Waveguides," *Silicon*, vol. 15, no. 3, pp. 1381–1391, Feb. 2023, doi: 10.1007/s12633-022-02105-8.

[2] K. Ishihara, K. Tsujikawa, M. Ohashi, K. Shiraki, and M. Tateda, "Full 2-D photonic bandgaps in silica/air structures," *Electron. Lett.*, vol. 31, no. 22, pp. 1941–1943, 1995.

[3] N. S. Lagali, M. R. Paiam, R. I. MacDonald, K. Worhoff, and A. Driessen, "Analysis of generalized Mach-Zehnder interferometers for variable-ratio power splitting and optimized switching," *J. Light. Technol.*, vol. 17, no. 12, pp. 2542–2550, 1999, doi: 10.1109/50.809675.

[4] D. Dai and S. He, "Optimization of Ultracompact Polarization-Insensitive Multimode Interference Couplers Based on Si Nanowire Waveguides," *IEEE Photonics Technol. Lett.*, vol. 18, no. 19, pp. 2017–2019, Oct. 2006, doi: 10.1109/LPT.2006.882227.

[5] Hongzhen Wei, Jinzhong Yu, Zhongli Liu, Xiaofeng Zhang, Wei Shi, and Changshui Fang, "Fabrication of 4 x 4 tapered MMI coupler with large cross section," *IEEE Photonics Technol. Lett.*, vol. 13, no. 5, pp. 466–468, May 2001, doi: 10.1109/68.920753.

Wavelength Independent Coupling Length Variation analysis using Silicon on Insulator based Rectangular Waveguide for Coupler/Splitter Application

Shalini Vardhan[1], Ritu Raj Singh[1]
[1]Department of Electronics and Communication Engineering, Netaji Subhas University of Technology, Delhi, India
E-mail: shalini.vardhan.phd21@nsut.ac.in

1. Introduction

Silicon on Insulator (SoI) technology poised to revolutionalize photonic world in terms of device compactness and operational speed. Many of the photonic active and passive devices uses waveguides in their geometry to couple optical power. Devices which uses coupler as their part of geometry are ring resonator, race track resonator, coupler and splitter itself [1]–[3]. As optical power transfers from one waveguide to other waveguides, therefore, coupling length (L_c) is an important parameter which requires precise calculation. To validate coupling length variation, rigourous simulation is performed using Finite Element Method (FEM) based Comsol Multiphysics software at 1550 nm operational wavelength.

2. Structure

The coupler strcture is demostrated in this section using two and three rectangular waveguides with no bends as shown in figure 1 subjecting to power coupled length variation. In SoI based waveguides mode exist because of high refractive index contrast between Si and SiO_2 [4] and therefore the power propagates. These two materials refractive index is calculated using Sellmeier's equation [5]. The width (w_{Si}) and height (h_{Si}) taken are 400 nm and 220 nm [6]. For ease of simulation the propagational length for each waveguide considered is 20 um and the gap (G) between each waveguide taken is 55 nm [1].

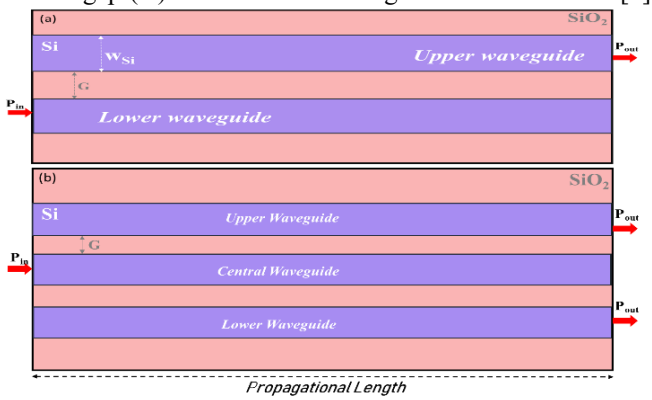

Figure 1. Top view schematic of SoI Rectangular Waveguide using (a) two waveguides (b) three waveguides

3. Result and Discussion

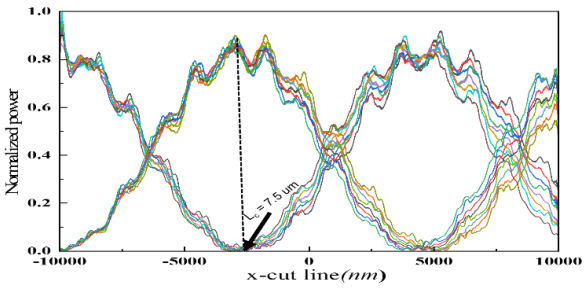

Figure. 2. Coupling length analysis with normalized power using two rectangular waveguides

The coupling length variation is studied using two and three rectangular waveguides.

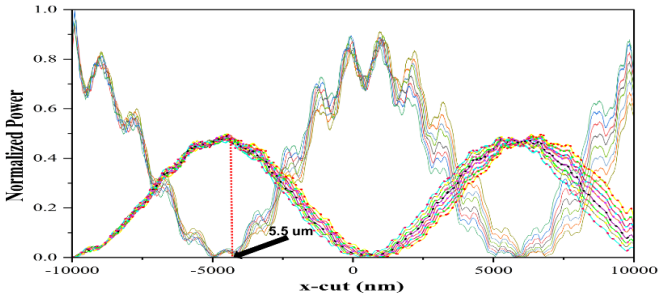

Figure 3. Coupling length analysis with normalized power using two rectangular waveguides

Figure 2 and figure 3 demostrates the relation of normalized power with x-cut on the propagational length of rectangular waveguides. In case of two rectangular waveguide structure power is fed to the lower waveguide and it couples to upper waveguide and it has been observed at 7.5 um power is equally splitted into both waveguides. while in case of three rectangular waveguide structure, power is impinged at the central waveguide and it equally splits to upper and lower waveguide approaching with the different coupling length i.e., 5.5 um.

4. Conclusion

Variation in coupling length in two and three waveguide coupler geometry is observed with power coupling length as 7.5 um and 5.5 um. The geometry has propagation length of 20 um in each case. The results shows that both the coupler has wavelength independency in the optical C-band. As no bends are reported in the coupler geometry, therefore bending losses are minimal. This section of geometry can be used in the application where power spliiter/coupler is designed and is a part of any device e.g., racetrack resonator.

REFERENCES

[1] D. Srivastava, S. Vardhan, and R. R. Singh, "SoI Based Optical 1 × 2 Wavelength Independent 3-dB Power Splitter Design Using Three Rectangular Cross-Sectional Cuboidal Waveguides," *Silicon*, vol. 15, no. 3, pp. 1381–1391, Feb. 2023, doi: 10.1007/s12633-022-02105-8.
[2] L. Zhang *et al.*, "Ultrahigh-Q silicon racetrack resonators," *Photonics Res.*, vol. 8, no. 5, p. 684, May 2020, doi: 10.1364/PRJ.387816.
[3] W. Couplers, L. Zimmermann, K. Voigt, G. Winzer, K. Petermann, and C. M. Weinert, "C -Band Optical 90 -Hybrids Based on," *IEEE Photonics Technol. Lett.*, vol. 21, no. 3, pp. 143–145, 2009.
[4] S. Dwivedi *et al.*, "Measurements of effective refractive index of SOI waveguides using interferometers," *Integr. Photonics Res. Silicon Nanophotonics, IPRSN 2015*, p. 371p, 2015, doi: 10.1364/iprsn.2015.im2a.6.
[5] S. Vardhan and R. R. Singh, "Design, simulation and performance comparison of SoI rectangular waveguide and SMF for methane detection," in *Integrated Photonics Platforms II*, May 2022, p. 32, doi: 10.1117/12.2621459.
[6] S. Vardhan and R. R. Singh, "Poynting Vector Analysis of SoI based Hybrid Plasmonic Rectangular Waveguide," in *JSAP-Optica Joint Symposia 2022 Abstracts*, 2022, p. 20p_C304_13, [Online]. Available: https://opg.optica.org/abstract.cfm?URI=JSAPO-2022-20p_C304_13.

[19p-B205-1~14] 4.3 Lasers and laser materials processing

Sze Yun Set(Univ. of Tokyo), Satoshi Hasegawa(Utsunomiya Univ.), Yusuke Ito(Univ. Tokyo)

Tue. Sep 19, 2023 1:30 PM - 6:30 PM B205 (Civic Auditorium)

△：Presentation by Applicant for JSAP Young Scientists Presentation Award

▲：English Presentation

▼：Both of Above

No Mark：None of Above

▲[19p-B205-1] [JSAP-Optica Joint Symposia 2023 Invited Talk] Ultrafast fiber lasers for multi-photon microscopy

○Takao Fuji[1], Hideji Murakoshi[2] （1.TTI, 2.NIPS）

1:30 PM - 2:00 PM

▲[19p-B205-2] Concise and Robust All-Fiber Ultrafast Laser Mode-Locked by Nonlinear Multimode Interference

○(D)Maolin Dai[1], Bowen Liu[1], Yifan Ma[1], Takuma Shirahata[1], Sze Yun Set[1], Shinji Yamashita[1] （1.Univ. of Tokyo）

2:00 PM - 2:15 PM

▲[19p-B205-3] High Speed Glucose Detection Infrared Spectroscopy System Based on Quantum Cascade Laser

○(P)JUNYI CHEN[1], Hiromitsu Furukawa[1] （1.AIST）

2:15 PM - 2:30 PM

▲[19p-B205-4] Tunable-Repetition-Rate Dual-Comb Generation in a Polarization-Maintaining Bidirectional Fiber Laser

○(DC)BOWEN LIU[1], MAOLIN DAI[1], YIFAN MA[1], TAKUMA SHIRAHATA[1], SHINJI YAMASHITA[1], SZE YUN SET[1] （1.The Univ. of Tokyo）

2:30 PM - 2:45 PM

▲[19p-B205-5] [JSAP-Optica Joint Symposia 2023 Invited Talk] Applying 3.6 μ m Mid-IR Fibre Lasers Beams to Compensate Thermal Lensing in LIGO Detectors

○Ori Henderson-Sapir[1,2,3], Daniel D. Brown[1,2], Michael Maclean[1,2], David J. Ottaway[1,2] （1.Dept. of Physics and Institute of Photonics and Advanced Sensing, The University of Adelaide, 2.OzGrav, University of Adelaide, 3.Mirage Photonics）

2:45 PM - 3:15 PM

▲[19p-B205-6] [JSAP-Optica Joint Symposia 2023 Invited Talk] The Visualization of Local Fluence Dependence in the Femtosecond Laser Processing of Dielectrics

○Haruyuki Sakurai[1] （1.The Univ. of Tokyo）

3:30 PM - 4:00 PM

▲[19p-B205-7] Laser Parameters for Square-Hole Drilling with Femtosecond Polarized Beam

○Wataru Watanabe[1], Kosuke Yoshina[1], Keiji Ebata[2], Hisao Kikuta[3] （1.Ritsumeikan University, 2.Sumitomo Electric Industries, 3.Osaka Metropolitan University）

4:00 PM - 4:15 PM

▲[19p-B205-8] Femtosecond Laser Ablation of Silicon using GHz to THz Burst Pulses: Numerical Simulation

○(P)Ashkan MomeniBidzard[1], Koji Sugioka[1] （1.RIKEN Center for Advanced Photonics）

4:15 PM - 4:30 PM

▼[19p-B205-9] Ultrafast dynamics of the interaction between double-pulse femtosecond laser and silica glass

○Guoqi Ren[1], Yusuke Ito[1], Reina Yoshizaki[1], Huijie Sun[1], Junya Hattori[1], Naohiko Sugita[1] （1.The University of Tokyo）

4:30 PM - 4:45 PM

▲[19p-B205-10] [JSAP-Optica Joint Symposia 2023 Invited Talk] Femtosecond laser ablation of dielectrics: experimental strategies for probing dynamics and controlling performance

○Mario Garcia-Lechuga[1], Jan Siegel[1], Javier Solis[1], Nicolas Sanner[2], Olivier Uteza[2], David Grojo[2] （1.Institute of Optics, CSIC, 2.Aix Marseille Univ, CNRS, LP3）

5:00 PM - 5:30 PM

▲[19p-B205-11] MACHINE LEARNING APPLICATION FOR HIGH – PRECISION AUTO FOCUSING IN LASER PROCESSING ON CURVED SURFACE

○(M1)Thi Phuong Anh Nguyen[1,2], Viet Hoang Dinh[2,3], Xuan Binh Cao[1,2] （1.School of Mechanical Engineering, Hanoi University of Science and Technology, 2.Square Lab, Hanoi University of Science and Technology, 3.School of Physical and Mathematical Sciences, Nanyang Technological University,）

5:30 PM - 5:45 PM

▲[19p-B205-12] Synthesis of Laser-Induced Graphene via Colorless Polyimide Film and its Potential in Pressure Sensing and Triboelectric Nanogenerators

○(D)SungYeob Jeong, Yusuke Ito, Huijie Sun, Naohiko Sugita

5:45 PM - 6:00 PM

▲[19p-B205-13] Microfluidic biochip of amorphous fluoropolymer CYTOP fabricated using two-photon polymerized 3D mold for high-resolution cell observation

○Kotaro Obata[1], Mirai Hanzawa[1,2], Felix Sima[1,3], Hiroyuki Kawano[1,4], Kazunari Ozasa[1], Yasutaka Hanada[5], Godai Miyaji[2], Atsushi Miyawaki[1,4], Koji Sugioka[1] （1.RIKEN RAP, 2.Tokyo Univ. of A. &T., 3.INFLPR, 4.RIKEN CBS, 5.Hirosaki Univ.）

6:00 PM - 6:15 PM

▲[19p-B205-14] Processing of Cultured Animal Cells by Femtosecond Laser Ablation: Toward Development of Compact and Low-cost Processing System for Cell Biology

○Kazunori Okano[1,2], Kishima Koichiro[2], Hosokawa Yoichiroh[1] （1.NAIST, 2.Pinpoint Photonics）

6:15 PM - 6:30 PM

1:30 PM - 2:00 PM (Tue. Sep 19, 2023 1:30 PM - 6:30 PM B205)

▲[19p-B205-1] [JSAP-Optica Joint Symposia 2023 Invited Talk] Ultrafast fiber lasers for multi-photon microscopy

○Takao Fuji[1], Hideji Murakoshi[2] (1.TTI, 2.NIPS)

Keywords: fiber laser, ultrashort pulse, multi-photon microscope

We introduce two femtosecond fiber laser systems for multiphoton microscopy, producing ~220 fs pulses at 1.3 μm and ~150 fs pulses at 1.8 µm, respectively. Starting from an erbium-doped silica fiber laser, we employ a highly nonlinear fiber for 1.3 μm conversion and a Raman shift fiber for 1.8 µm conversion. The pulses are amplified using Pr:ZBLAN and Tm:ZBLAN fiber amplifiers, reaching average powers of 0.1 W and 1.3 W, respectively. With the system of the Tm:ZBLAN fiber amplifier, we successfully image TurboFP635-expressing cortical neurons at a depth of 0.7 mm using three-photon excitation and Clover-expressing astrocytes at a depth of 0.15 mm using four-photon excitation with 1.8 μm pulses. Our findings demonstrate the potential of our laser system in advancing cellular imaging in deep tissues, enhancing our understanding of dynamic biological processes.

Concise and Robust All-Fiber Ultrafast Laser Mode-Locked by Nonlinear Multimode Interference

Maolin Dai[1], Bowen Liu[1], Yifan Ma[1], Takuma Shirahata[1], Sze Yun Set[1] and Shinji Yamashita[1]

[1] The University of Tokyo
E-mail: maolin@cntp.t.u-tokyo.ac.jp

1. Introduction

Ultrafast fiber lasers achieved by passive mode-locking techniques have wide application potentials from fundamental research to industry applications. Recently, nonlinear multimode interference existed in multimode fibers is proved to provide fast saturable absorption and can be used for ultrafast laser generation, and is especially paid much attention owing to various advantages [1]. We report an all-fiber ultrafast laser mode-locked by a graded-index multimode fiber (GI-MMF) saturable absorber based on nonlinear multimode interference, with a super concise cavity configuration and robust laser operation.

2. Experiment results and discussions

The schematic diagram of the proposed laser is shown in Fig. 1. The laser cavity enjoys a very concise and compact ring configuration, by incorporating a tap/isolator/wavelength division multiplexer (TI-WDM), a in-line polarization controller (PC), and a 15-cm graded-index multimode fiber with a core diameter of 50 μm. The 980 nm laser diode is used as the pump source, and 30-cm highly Er-doped fiber (EDF, Er 80-4/125, Liekki) is adopted to provide enough gain for laser operation. A fiber stretcher is employed to tune the light propagation in GI-MMF for laser mode-locking.

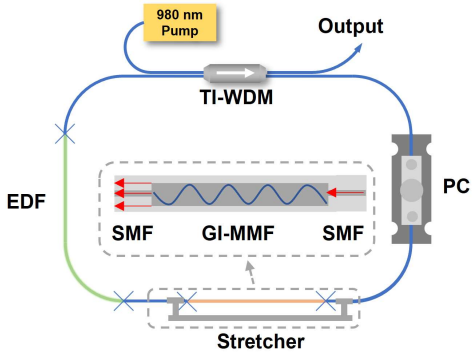

Fig. 1. Schematic diagram of the proposed mode-locked fiber laser.

By properly controlling the PC and the fiber stretcher, self-started mode-locking is achieved when pump power is turned to 150 mW. The output power in 1550 nm is measured as 1.6 mW, with the 10% tap coupling ratio. The laser output is shown in Fig. 2. Fig. 2(a) shows the optical spectrum of the mode-locked laser, measured by an optical spectrum analyzer (OSA, AQ6317B, ANDO), which is a typical traditional soliton spectral shape. Multiple explicit Kelly sidebands are distributed symmetrically around the central wavelength. The central wavelength of mode-locking is at 1563 nm, and the full width at half maximum (FWHM) is measured as 10.81 nm. The theoretical pulse width is calculated as 236.4 fs, which is benefited from the fast saturable absorption of GI-MMF. Fig. 2(b) shows the uniform pulse train measured by a photodetector (1-GHz, NEWFOCUS) and an oscilloscope (DS2202A, RIGOL). The pulse interval is measured as 17.4 ns. The radio frequency (RF) spectrum measured by a spectrum analyzer (RSA3045, RIGOL) is shown in Fig. 2(c), the central frequency is located 58.07 MHz, indicating the laser owns a fundamental repetition rate of 58.07 MHz. The signal to noise ratio (SNR) is measured as larger than 70 dB, showing the robust single pulse operation. In Fig. 2(d), the spectral stability is proved by recording the spectral shape in 4 hours. The optical spectrum keeps its original shape during the test.

3. Conclusions

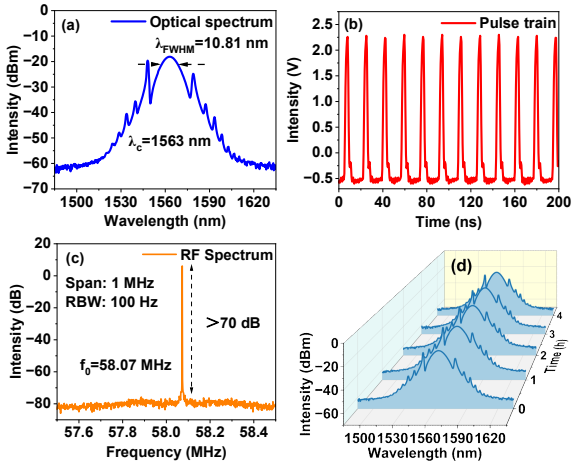

Fig. 2. Laser output. (a) Optical spectrum, (b) pulse train, (c) RF spectrum and (d) spectral stability.

We proposed an ultrafast fiber laser mode-locked by nonlinear multimode interference, with a concise cavity configuration. The proposed laser shows its good performance, and has potential for real applications.

Acknowledgements

We would like to express sincere thanks to Japan Society for the Promotion of Science (JSPS) Grant-in-Aid for Scientific Research (A) 23H00174, (A) 22H00209, and Core Research for Evolutional Science and Technology (JPMJCR1872).

References

[1] X. Liu et al., Opt. Laser Technol., 159 (2023), 108941.

High Speed Glucose Detection Infrared Spectroscopy System Based on Quantum Cascade Laser

Junyi Chen[1], Hiromitsu Furukawa[1]

[1] Sensing System Research Center, National Institute of Advanced Industrial Science and Technology
E-mail: chen.junyi@ aist.go.jp, h-furukawa@aist.go.jp

1. Introduction

The global prevalence of diabetes has risen dramatically, with the number of affected individuals increasing from 108 million in 1980 to 537 million in 2021 [1]. Unfortunately, there is currently no known cure for diabetes, making early detection through blood glucose testing necessary. Therefore, the development of accurate, rapid, simple, and real-time methods for measuring blood glucose levels is of utmost importance in diagnosing diabetes. Traditional invasive techniques for measuring blood glucose involve the uncomfortable and inconvenient process of pricking a finger to obtain a blood sample [2]. Infrared spectroscopy has emerged as a promising noncontact method for detecting glucose concentrations. Mid-infrared spectroscopy demonstrates a strong and broad absorption pattern that serves as a fingerprint absorption for glucose. Consequently, there has been significant interest in exploring the application of these spectroscopic methods [3].

2. General Instructions

This study introduces a novel method for measuring glucose concentration through transmission spectroscopy. This method utilizes a high-speed infrared spectroscopic technique employing a mid-infrared wavelength-swept pulse quantum cascade laser (QCL). The advantage of this approach is its implementation of the transmission optics system, which eliminates the need for complex adjustments or regular maintenance. Additionally, a special asynchronous signal method is developed to reduce the measurement time to 20 ms, while achieving a 30× integration in a mere 0.6 s. With the high power of the QCL and the proposed algorithm, the concentration of glucose solution samples with an optical path length of 0.2 mm can be accurately measured.

Figure 1 is the absorbance spectra of glucose in different concentration. In all the spectra, there are two high-intensity absorption peaks at 9.25 μm and 9.60 μm and a low-intensity peak at 9.05 μm. These peaks can be attributed to the stretching and bending vibrations of the C-H-O bonds.

Figure 2 illustrates the average absorbance in various concentration samples, accompanied by a linear regression line describing the relationship between absorbance and glucose concentration. The error bars associated with the concentration points indicate a maximum error of 1.2% and a minimum error of 0.4%, affirming the consistency and stability of repeated measurements. The linear regression yields R^2 values as high as 0.999.

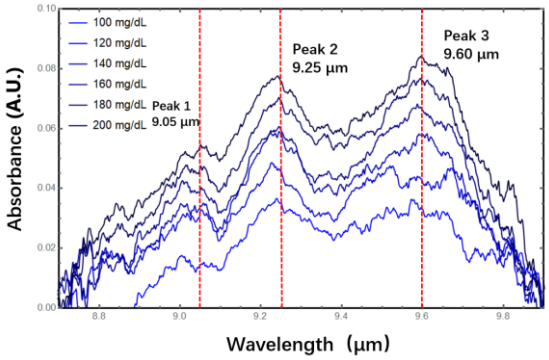

Fig.1. Absorbance spectra of glucose at difference concentrations transformed from the transmittance spectra.

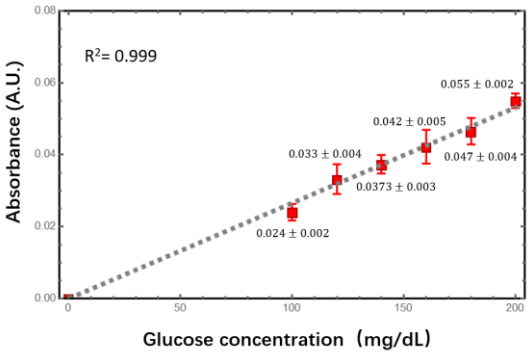

Fig. 2. Linear regression of the average absorbance and glucose concentration.

3. Conclusions

Our transmission spectroscopic system can rapidly detect different concentrations of glucose even in strong water absorption cases. In future studies, we plan to improve the system to measure the blood glucose concentration, such as measurement of tear on the eyeball. we intend to design a simulated solution resembling tear fluid and measure its glucose concentration.

Acknowledgements

This work was supported by the New Energy and Industrial Technology Development Organization (NEDO) [project code P19005].

References

[1] H. Sun, et al., Diabetes Res. Clin. Pract. **183** (2022) 109119.
[2] S. Kubihal, et al., Diabetes Metab. Syndr. Clin. Res. Rev. **15** (2021) 45–53.
[3] T. Koyama, et al., Sensors. **20** (2020) 1–11.

偏波保持双方向ファイバーレーザーにおける可変繰り返しレートデュアルコム生成

Tunable-Repetition-Rate Dual-Comb Generation in a Polarization-Maintaining Bidirectional Fiber Laser

東京大学先端研，○柳 博文，戴 茂林，麻 一凡，白畑 卓磨，山下 真司，セット ジイヨン

The Univ. of Tokyo, RCAST, ◦Bowen Liu, Maolin Dai, Yifan Ma, Takuma Shirahata, Shinji Yamashita, Sze Yun Set

E-mail: bwliu@cntp.t.u-tokyo.ac.jp

Ultrafast laser is an ideal playground for the study of precise spectroscopy and microscopy that heavily rely on the high-performance optical frequency combs, which is the unique nature of mode-locked fiber laser. In particular, dual-comb fiber laser can greatly improve system performance while reducing complexity by developing self-referencing combs and coupling pulse trains with different repetition rates. Whereas the repetition rate is generally determined for a certain lasing resonator, which creates additional constraints in dual-comb applications. In this paper, we demonstrate a bidirectional polarization-maintaining mode-locked fiber laser, of which the two orthogonal polarization components propagating along fast- and slow-axis are bidirectionally multiplexed resonate clockwise and counterclockwise, respectively. The repetition rate of clockwise lasing pulses is fixed according to the certain cavity length, while the one of another lasing components traveling opposite can be tuned continuously through the intra-cavity delay line. The maximum tuning range of the counterclockwise repetition rate reaches 681.6 kHz. Compared with fixed loop, the largest RF difference between two combs is 978.2 kHz, almost equals to 1 MHz. Meanwhile, the dual combs generate in two opposite directions have nearly the same central wavelength, enabling high coherence. Different from most current dual-comb solutions, this high-coherent characteristic could greatly improve the performance of the dual-comb system, making it also have potential in some specific spectroscopy and microscopy measurement scenarios.

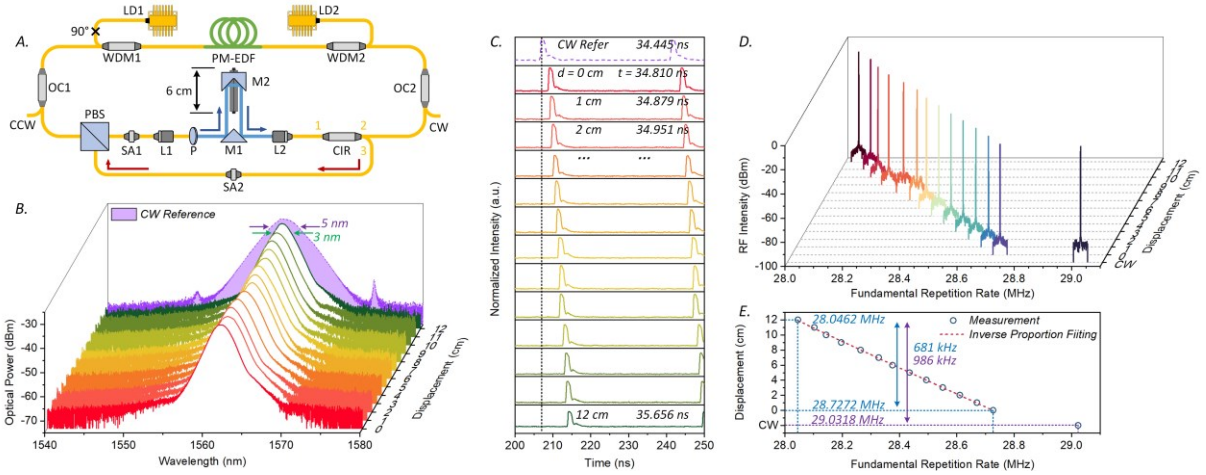

Fig. 1 (A) Schematic diagram of the laser setup; (B) Optical spectra and (C) Pulse trains as the delay line moving; (D) Repetition rate tuning; (E) Inverse proportional fitting.

Applying 3.6 μm Mid-IR Fibre Lasers Beams to Compensate Thermal Lensing in LIGO Detectors

Ori Henderson-Sapir[1,2,3], **Daniel D. Brown**[1,2], **Michael Maclean**[1,2] and **David J. Ottaway** [1,2]

1. Dept. of Physics and Institute of Photonics and Advanced Sensing, The University of Adelaide, SA, Australia

2. OzGrav, University of Adelaide, Adelaide, SA, Australia

3. Mirage Photonics, Oaklands Park, SA, Australia

The initial detection of gravitational waves at LIGO (Laser Interferometric Gravitational Observatory) from merging massive stellar objects ushered in a new type of astronomy [1]. Improved detector sensitivities increased the observable volume of space from which gravitational wave events can be detected. This has brought into focus the era of multi-messenger astronomy in 2017 [2], where various types of observation from different parts of the electromagnetic spectrum (radio, infrared, visible, X-ray, gamma rays) can observe simultaneously the same cataclysmic events expending our understanding of the universe, elements creation and the birth and death of stars.

Further increase of the observable volume of space in the current generation of LIGO detectors relies on increasing the circulating power of the laser beams within the interferometer arms. However, increased power results in stronger thermal lensing at the centre of test masses (the mirrors confining the laser beams within the interferometer). Increased thermal lensing causes the interferometer to lose lock on the propagating optical modes. Currently the thermal lensing issue is dealt with ring heaters around the test masses that apply heat to the outside of the large circular optics to counteract the lensing and return the optic back to its original curvature. Residual wavefront distortion is then countered by projecting CO_2 laser beams onto the back side of the compensation plate optics through fixed transmission masks.

We propose to swap the CO_2 lasers with mid-IR based fibre lasers operating at the 3.6 μm band. In additional to also replace the fixed masks with spatial light modulators (SLMs) as the mechanism to shape the projected patterns onto the compensation plates (see Fig. 1). The 3.6 μm fibre laser will be based on the dual wavelength pumping technique [3] operating at a few Watts. It is expected that good power stability can be obtained from these sources compared with the CO_2 lasers. Using SLMs will enable dynamic control of the projection shape and location on the optics. This will allow to address both point absorber defects in the optics, as well as allowing for varying levels of compensation during power up – essential for maintaining the interferometer lock at high circulating power and a current roadblock to increasing sensitivity.

We will offer a brief summary of the present status of mid-IR fibre lasers in the 3.6 μm band, followed by a presentation of our most recent design parameters and outcomes related to the LIGO project.

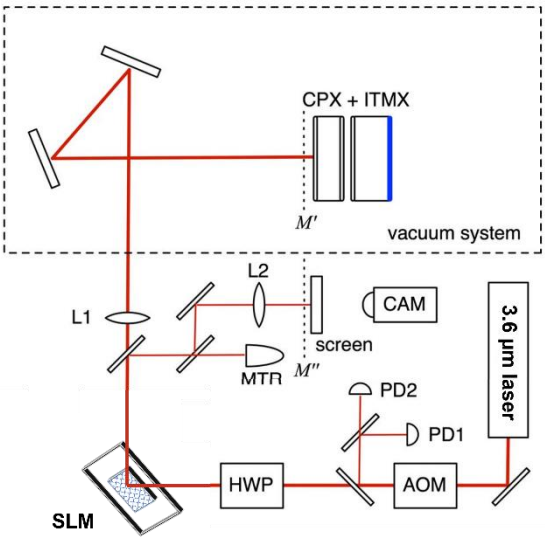

Fig. 1 Schematics of the proposed laser projection compensation system. AOM – Acousto optic modulator, HWP – half waveplate, MTR – power meter, SLM – spatial light modulator, CAM – camera, CPX – compensation plate X arm, ITMX – input test mass X arm.

References

[1] B.P.Abbott et al., Observation of Gravitational Waves from a Binary Black Hole Merger. Physical Review Letters, 2016. 116(6): p. 061102.

[2] Abbott, B.P. et al, Multi-messenger Observations of a Binary Neutron Star Merger. The Astrophysical Journal Letters, 2017. 848(2): p. L12.

[3] Henderson-Sapir, O., J. Munch, and D.J. Ottaway, Mid-infrared fiber lasers at and beyond 3.5um using dual-wavelength pumping. Optics Letters, 2014. 39(3): p. 493-496.

The Visualization of Local Fluence Dependence in the Femtosecond Laser Processing of Dielectrics

Haruyuki Sakurai

The University of Tokyo, Institute for Photon Science and Technology
E-mail: sakurai@ipst.s.u-tokyo.ac.jp

1. Introduction

Femtosecond laser processing has gained attention in recent years as a method to allow for non-contact, freeform processing of a wide variety of materials, including transparent dielectrics [1]. However, effective use of femtosecond lasers is not always trivial due to the large variety of parameters available for tuning the highly nonlinear process. Knowledge of the basic light-matter interaction dependencies to each parameter would be important to improving the controllability of laser processing.

One of, if not the first parameter tuned in laser processing and a key independent variable in many fundamental experiments is the incident laser fluence. Defined as the incident energy per unit area, for Gaussian pulses, the value of the fluence at the pulse center, or the peak fluence, is often used to standardize experimental results obtained in various laser systems. However, this approach does not explicitly recognize the spatially local fluence distribution and the effect it may have on final ablation results. The appropriateness of this treatment is a non-trivial issue, which, when explored in detail, should yield a richer and deeper understanding of the underlying physical processes occurring during the laser ablation process.

To move beyond this paradigm of characterizing laser ablation by a singular fluence value, we developed a new technique to characterize and correlate the entire laser fluence distributions to the final ablation results [2]. With this technique, we seek to elucidate the limits of the singular fluence treatment of the ablation process.

2. Experiment

To characterize the fluence distribution of a laser pulse, the beam profile must be measured in detail at the focal point. To achieve this, we modify a commercially available CMOS camera with 1.12 μm pixel pitch to directly image the beam profile at the focus. Afterwards, the same beam is used to ablate a sample. Each point on the ablation crater can then be spatially correlated to a local fluence value. This relationship may be plotted on a histogram, or "fluence map," thereby visualizing the relationship between the incident local fluence and ablation results. An illustration of this process is shown in Figure 1(a). Correspondingly, Fig. 1(b) shows an actual fluence map. Here, a single 30 μJ pulse energy, 1030 nm central wavelength, 190 fs pulse focused onto the surface of sapphire by an f100 mm plano-convex lens. A laser scanning microscope is then used to characterize the crater morphology. The fluence map correlates the height information from the microscope with the fluence information from the profiler. This single map details important ablation characteristics. For example, the peak fluence corresponds to the right-most data point, while the crater depth the bottom-most. The threshold fluence can be seen as the point where heights decline from zero. In the presentation, we further demonstrate how the fluence map can reveal information about the ablation properties of dielectrics, among other recent results.

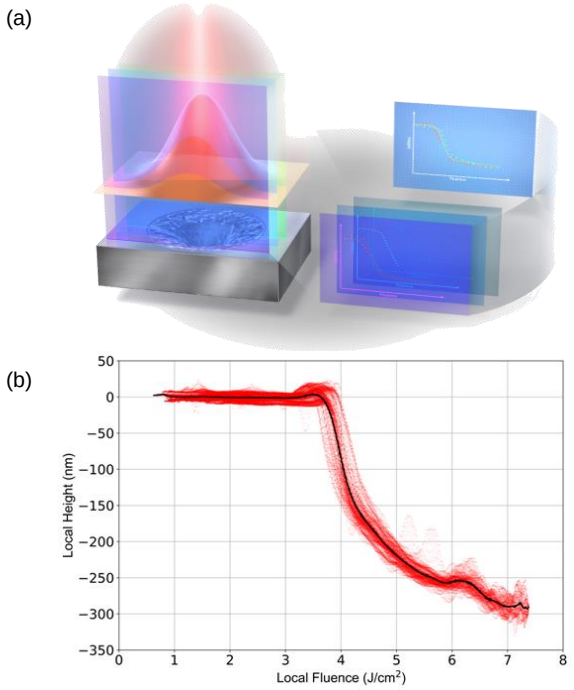

Figure 1 (a) Conceptual image of the fluence mapping process. (b) An actual fluence map of a femtosecond-laser ablated crater on sapphire.

Acknowledgements

This work was supported in parts by MEXT Leading Graduates Schools Program, Advanced Leading Graduate Course for Photon Science (ALPS), MEXT Quantum Leap Flagship Program (MEXT Q-LEAP) Grant Number JPMXS0118067246, the Center of Innovation Program funded by the Japan Science and Technology Agency (JST), and the New Energy and Industrial Technology Development Organization (NEDO) project "Development of advanced laser processing with intelligence based on high-brightness and high-efficiency laser technologies (TACMI project)."

References

[1] P. Balling and J. Schou, Rep. Prog. Phys. **76**, 036502 (2013).
[2] H. Sakurai *et al*., Commun. Mater. **2**, 38 (2021).

Laser Parameters for Square-Hole Drilling with Femtosecond Polarized Beam

Wataru Watanabe[1], Kosuke Yoshina[1], Keiji Ebata [2], Hisao Kikuta[3]
[1] Ritsumeikan University, [2] Sumitomo Electric Industries, [3] Osaka Metropolitan University
E-mail: wata-w@fc.ritsumei.ac.jp

1. Introduction

Micro-hole drilling with femtosecond lasers enable micro-fabrication with minimal thermal effects, has attracted much attention. The polarization state of a laser beam has a strong influence on the process in almost any kind of laser material processing [1-3]. Previous studies have reported the possibility of obtaining square holes by controlling the intensity distribution and polarization distribution using polarization converters [4,5].

In this study, we investigate the processing conditions for square hole processing using a polarization-converting element.

2. Experimental

Figure 1 shows a schematic for square-hole drilling with femtosecond polarized beam. Square hole machining drilling was performed using a Ti:sapphire laser system with 800 nm wavelength and a 1 kHz repetition rate. A laser beam was attenuated using a rotatable half-wave plate and a Glan laser polarizer. Laser pulses of 130-fs duration were focused using a lens (focal length: 50 mm). The irradiation of laser pulses was conducted in air. We used the unequally divided polarization conversion element. The element consists of a combination of 1/2-wave plates with different principal axes at different locations, alternating between 8-segmented 1/2-wave plates with center angles of 60° and 30°.

In this experiment, the laser processing conditions for square-hole drilling were investigated by changing the number of irradiation pulses, pulse energy, displacement from the focal point of the focusing lens, and aperture diameter. Stainless steel (SUS304) plate with a thickness of 0.1 mm is used as samples. The shape of the holes after drilling was observed using a scanning electron microscope.

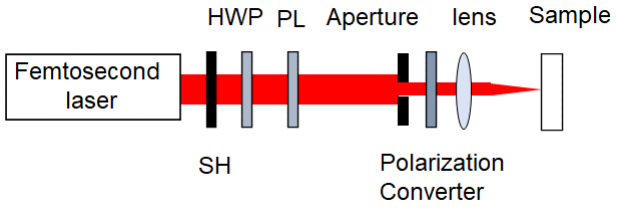

Fig. 1. Schematic for square-hole drilling with femtosecond polarized beam. SH: shutter, HWP: half-wave plate, and PL: polarizer.

3. Results

Figure 2 shows SEM images of front and rear surface of the drilled hole. The aperture diameter of 2 mm and the number of irradiation pulses of 8000 were fixed, and only the pulse energy was varied between 45 and 110 μJ/pulse. When the pulse energy was 45 μJ/pulse, the hole was not produced. When the pulse energy was higher than 95 μJ/pulse, the corners are rounded off due to the influence of intensity distribution rather than the influence of polarization. Therefore, a pulse energy range of 60~75 μJ/pulse is considered optimal energy for square hole drilling.

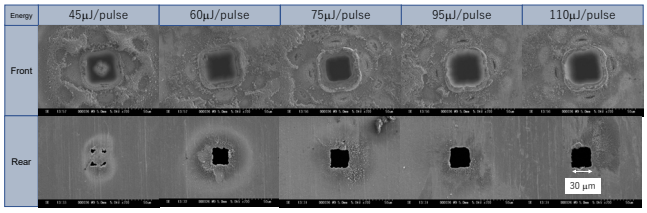

Fig. 2 SEM images of square hole drilled with a cross-polarized beam.

4. Conclusions

A polarization converter was used to control the intensity and polarization distribution at the focal point to produce a square hole. We investigated laser processing windows for square-hole drilling of stainless steel (SUS304) plate with a thickness of 0.1 mm.

References

[1] S. Nolte, C. Momma, G. Kamlage, A. Ostendorf, C. Fallnich, F. Vonalvensleben, and H. Welling, Appl. Phys. A **68** (1999) 563.
[2] V. G. Niziev and A. V. Nesterov, J. Phys. D: Appl. Phys. **32** (1999) 1455.
[3] M. Meier, V. Romano, and T. Feurer, Appl. Phys. A **86** (2007) 329.
[4] M. Kraus, M. Ahmed, A. Michalowski, A. Voss, R. Weber, and T. Graf, Opt. Express **18** (2010) 22305.
[5] H. Kikuchi, A. Mizutani, and H. Kikuta, Jpn. J. Appl. Phys **55** (2016) 042701.

Femtosecond Laser Ablation of Silicon using GHz to THz Burst Pulses: Numerical Simulation

Ashkan Momeni, Koji Sugioka*

RIKEN Center for Advanced Photonics, 2-1 Hirosawa, Wako-shi, Saitama 351-0198, Japan
E-mail: ksugioka@riken.jp

1. Introduction

In recent years, laser processing with GHz and THz bursts of femtosecond pulses has attracted great attention to improving the efficiency of laser-induced microfabrication [1-6]. In this context, we demonstrated that femtosecond laser ablation of silicon in GHz burst mode can improve ablation efficiency [3, 4]. The efficient absorption of laser energy in the GHz burst and the heat-accumulation effect have been proposed as the main mechanisms for ablation enhancement [3-5]. However, the possible mechanisms have not yet been fully elucidated and more investigations are needed. Therefore, in this study, we used COMSOL Multiphysics to simulate the GHz and THz burst mode femtosecond laser ablation of silicon and investigate the responsible mechanisms of the ablation efficiency enhancement.

2. Simulation Method and Results

The deformation geometry model was applied to simulate material removal and crater formation. We used the model of heat transfer by thermal conduction to study the temperature evolution of silicon during irradiation with GHz and THz bursts of femtosecond laser pulses. The heat transfer model can be defined by [6]:

$$\rho C \frac{\partial T}{\partial t} - \nabla.(k\,\nabla T) = 0, \quad (1)$$

where ρ, k and C are the density, thermal conductivity and specific heat capacity of silicon, respectively. The burst pulse was considered as an incoming heat flux on the silicon surface defined by [6]:

$$-\mathbf{n}.(k.\nabla T) = I(r,z,t), \quad (2)$$

where n is the normal vector of silicon surface and I represents the laser intensity of a burst pulse as [6]:

$$I(r,z,t) = (1-R)\left(\frac{2E_{Burst}}{\pi\omega^2}\right)B(t)\,e^{-2\left(\frac{r}{\omega}\right)^2}e^{\alpha(z-z_0)}, \quad (3)$$

with R being the reflectivity of silicon, ω the focused laser spot radius and $\alpha = \alpha_{SPA} + \alpha_{FCA}$ sum of the coefficients of absorption by a single-photon and native free carrier absorption [6]. We defined the laser energy distribution of the burst pulse over time by function of *B(t)*, consisting of a train of femtosecond laser pulses with intervals of 0.05 to 500 ps corresponding to 20 THz to 2 GHz.

Figure 1(a) shows a pulse shape of a single burst of femtosecond pulses with an intra-pulse number of 25 with a burst pulse energy of 1 μJ at a 4.88 GHz repetition rate. The simulation results of silicon laser ablation by using this GHz burst are presented in Figure 1(b), indicating a quantitatively good agreement with the experimental measurements for ablation depth as well as crater profile on silicon. The simulated results demonstrated the enhancement of ablation efficiency due to the heat-accumulation effect and efficient absorption of laser energy in the GHz burst. Moreover, this simulation model could predict an enhancement in silicon ablation efficiency using THz bursts of femtosecond laser pulses.

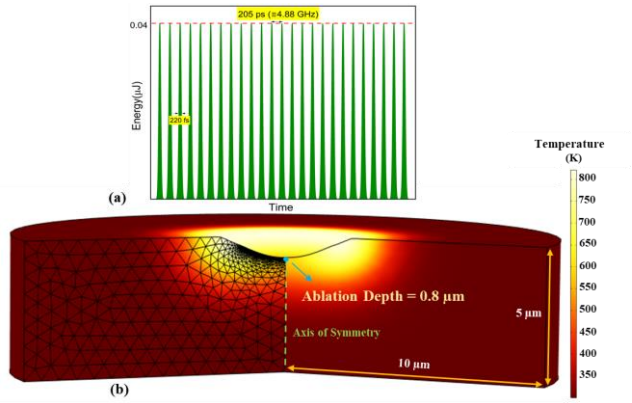

Fig. 1 Computational geometry for silicon with a thickness of 5 μm and a diameter of 20 μm.

3. Conclusions

This study presented a numerical simulation of the GHz and THz burst mode femtosecond laser ablation of silicon using COMSOL Multiphysics. The results were in a good agreement with the experimental measurement to confirm ablation efficiency enhancement with the GHz burst mode laser processing. In addition, the simulation model predicted that the laser ablation of silicon using THz bursts of femtosecond pulses could improve the ablation yield.

Acknowledgements

This work was partially supported by MEXT Quantum Leap Flagship Program (MEXT Q-LEAP) Grant Number JPMXS0118067246.

References

[1] K. Sugioka: Int. J. Extrem. Manuf.,**1** (2019) 012003.
[2] C. Gaudiuso, et al: Sci Rep, **11**, (2021) 13321.
[3] F. Caballero-Lucas. K. Obata, and K. Sugioka: Int. J. Extrem. Manuf., **4** (2022) 015103.
[4] K. Obata, et al: Int. J. Extrem. Manuf., **5** (2023) 025002.
[5] K. Mishchik, et al: Opt. Lett., **44**, (2019) 2193-2196.
[6] A. Momeni, and K. Sugioka: J. Laser Micro/Nanoeng., (in press).

Appendix

Secretariat of the JSAP-Optica Joint Symposia
E-mail: meeting@jsap.or.jp

Ultrafast dynamics of the interaction between double-pulse femtosecond laser and silica glass

Guoqi Ren[1], Yusuke Ito[1], Reina Yoshizaki[1], Huijie Sun[1], Junya Hattori[1], Naohiko Sugita[1]

[1] Department of Mechanical Engineering, School of Engineering, The University of Tokyo,
E-mail: y.ito@mfg.t.u-tokyo.ac.jp

1. Introduction

Temporally shaping a single femtosecond (fs) laser pulse into a double-pulse (DP) mode has been demonstrated to be an efficient method for internal modifications of transparent dielectrics [1,2]. However, the mechanism of double-pulse propagation and excitation in dielectrics has not been well clarified. In this work, the ultrafast response of silica glass under the irradiation of a shot of DP fs laser is studied. The results are helpful for understanding the laser absorption into the excited electrons, as well as the microprocessing applications in integrated photonics.

2. Experimental setup

Figure 1 shows the experimental setup. A 1030 nm fs laser pulse generated from a Yb:KGW laser system is split into pump and probe pulses. The pump pulse is further divided into two sub pulses P1 and P2 with an adjustable inter-pulse delay (IPD). The pump pulses are focused into the sample using an objective (Mitutoyo; M Plan Apo NIR 10×). The probe pulse is frequency-doubled by a beta barium borate (BBO) and then passes through the sample perpendicularly with pump pulses. The captured images are magnified by another objective (Mitutoyo; M Plan Apo NIR 20×) and recorded onto a cooled charge-coupled device (CCD) (Bitran; BU-55LN) which is synchronized with the laser system. Both pump pulses have an energy of 10 μJ, and a fluence of 3.93 J/cm^2 on the sample surface.

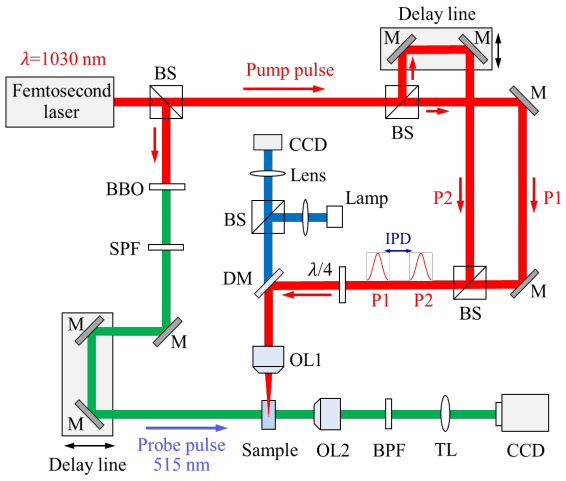

Fig. 1. Experimental setup. BS: beam splitter; λ/4: quarter waveplate; SPF: short pass filter; BPF: band pass filter; TL: tube lens; M: mirror; DM: dichroic mirror.

3. Results and discussion

The plasma filaments captured with a pump-probe delay of 1 ps are presented in Fig. 2. After the irradiation of P1, the plasma filament is shown in Fig. 2(I), where the main excitation regions are inside the materials, starting around Z = 40 μm. After the irradiation of P2 with an IPD of 1 ps, filament extends to the sample surface, and its diameter becomes larger. With the increase of IPD from 1 to 1000 ps, the starting position of the filament gradually shifts into a deeper region, and filament diameter gradually decreases, as shown in Fig. 2(II)-2(V), indicating that P1 excitations have a temporal effect on P2 propagation and excitations. Part of P2 is absorbed in the shallow and edge regions of filament induced by P1 when the IPD is smaller thus resulting in a separation of main excitation regions between P1 and P2. More energy of P2 can be delivered into a deeper region with a smaller diameter to excite more electrons while using larger IPDs, which contributes to the efficient internal processing.

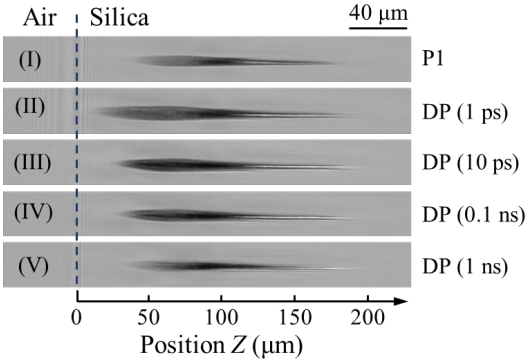

Fig. 2. Plasma filament induced by P1 and DP. The pump and probe delays are 1 ps in all the conditions.

4. Conclusion

In this work, the interaction between DP fs laser and silica glass has been studied using the pump-probe imaging method. The free electrons excited by P1 have a temporal effect on the absorption and propagation of P2, resulting in different processing characteristics.

References

[1] S. Ahn, J. Choi, J. Noh, and S.-H. Cho. Opt. Lasers Eng. 101, 85–88 (2018).
[2] J. Del Hoyo, R. Meyer, L. Furfaro, and F. Courvoisier. Nanophotonics 10(3), 1089–1097 (2021).

Femtosecond laser ablation of dielectrics: experimental strategies for probing dynamics and controlling performance

Mario Garcia-Lechuga [1], Jan Siegel [1], Javier Solis[1], Nicolas Sanner [2], Olivier Utéza [2], David Grojo [2]

[1] Laser Processing Group, Instituto de Optica Daza de Valdes (IO), CSIC, 28006 Madrid, Spain

[2] Aix Marseille Université, CNRS, LP3, UMR7341, 13288 Marseille, France 2

E-mail: mario.garcia.lechuga@csic.es

Femtosecond lasers are widely used in the processing of dielectric materials, with applications ranging from microelectronics and photonic device manufacturing to glass processing. Furthermore, the extreme nonlinear and thermodynamic conditions experienced by the material during femtosecond laser processing make it an area of great interest from a fundamental perspective. However, these lead to complex problems with interplay between various processes. In this work, we present different experimental approaches that allow for a better understanding of the fundamentals involved in modifying the dielectric surface, as well as the resulting consequences on machining performance.

In the first part, we present the results obtained using time-resolved microscopy. This pump-and-probe technique enables the visualization of electron excitation dynamics with femtosecond time resolution, aiding in determining the relative roles of different excitation mechanisms (multiphoton versus impact ionization). We also examine irreversible transformation dynamics, such as ablation [1], by comparing the results with behavior observed in metals and semiconductors, as well as studying the formation of a heat-affected zone [2], corroborating that thermal effects in processing with ultrashort laser pulses cannot be neglected.

In the second part, we conduct a comprehensive study on the role of laser wavelength, covering the range from UV to MIR, in superficial modifications of dielectrics. Firstly, we focus on understanding and controlling spatial resolution aspects, challenging the applicability of the concept of nonlinear resolution commonly used in multiphoton microscopy to femtosecond laser ablation [3]. Secondly, we investigate laser-induced topographies in dielectrics by tuning the wavelength. The study reveals a counterintuitive quasi-invariance of material responses, including the measured fluence threshold for ablation and the maximum achievable crater depth, despite strongly varying nonlinear interaction processes. These findings are supported by simulations considering the balance between the different excitation mechanisms (multiphoton, tunneling, and avalanche) and applicable dissociation energy conditions [4].

References**:**

[1] M. Garcia-Lechuga, J. Solis, and J. Siegel, Appl. Phys. A 124, 221 (2018).

[2] M. Garcia-Lechuga, J. Solis, and J. Siegel, Appl. Phys. Lett. 108, 171901 (2016).

[3] M. Garcia-Lechuga, O. Utéza, N. Sanner, and D. Grojo, Opt. Lett. 45, 952 (2020).

[4] M. Garcia-Lechuga, O. Utéza, N. Sanner, and D. Grojo, Phys. Rev. Appl. 19, 044047 (2023).

MACHINE LEARNING APPLICATION FOR HIGH – PRECISION AUTO FOCUSING IN LASER PROCESSING ON CURVED SURFACE

Thi Phuong Anh Nguyen [1,2], Viet Hoang Dinh [2,3], Xuan Binh Cao[1,2*]

[1] School of Mechanical Engineering, Hanoi University of Science and Technology, Hanoi 100000, Viet Nam

[2] Square Lab, Hanoi University of Science and Technology, Hanoi 100000, Viet Nam

[3]School of Physical and Mathematical Sciences, Nanyang Technological University, Singapore 637371, Singapore

***E-mail:** binh.caoxuan@hust.edu.vn

ABSTRACT:

The use of the laser technology in production has several limitations, particularly when fabricating on curved surfaces. Thus, we suggested a new method that combines an autofocusing methodology with machine learning algorithm that precisely assess the focus status during laser processing on curved surface.

Keywords: Autofocusing, Machine learning.

I. INTRODUCTION

Laser processing is the technique which patterning outcome depends on the ability of maintaining the laser focal point. Failure in locating the focal position often leads undesirable patterns. The proposed method which combinated of experimental setup with CNN model that correctly predicts sample's focus status.

II. METHODOLOGY

In 2016, Cao et al. [1] proposed an experimental setup for determining the sample's defocus distance and tilt angle during laser material processing (Fig. 1). To properly calculate the position of the focus point on curved surfaces, we created a CNN model using the results of this experiment (Fig.2). Regardless of image complexity, the CNN model may learn domain-specific features and predict various qualities based on these features. Furthermore, a CNN model is capable of eliminating noise from the data environment while retaining the critical feature. As a result, this technology is the most precise and effective for laser processing on curved surface patterns.

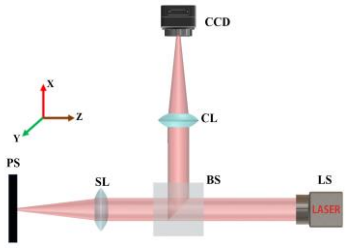

Figure 1: Experimental setup for detecting focal point

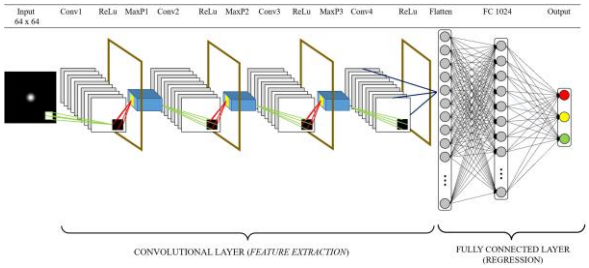

Figure 2: CNN model architecture

III. RESULT AND DISCUSSION

The proposed method achieves high precision results with a tolerance of defocus of less than ±10μm and tilt angles along the x and y axes of less than ±0.05◦.

IV. CONCLUSION

In this paper, we provided and systematically investigated a convolutional neural network-based focus inspection technique.

REFERENCES

[1] Binh Xuan Cao, Phuong Le Hoang, Sanghoon Ahn, Jeng-o Kim, and Jiwhan Noh. High-precision detection of focal position on a curved surface for laser processing. Precision Engineering, 50:204–210, 2017.

Synthesis of Laser-Induced Graphene via Colorless Polyimide Film and its Potential in Pressure Sensing and Triboelectric Nanogenerators

Sung-Yeob Jeong[1], Yusuke Ito[1], Huijie Sun[1], and Naohiko Sugita[1, *]
[1] Department of Mechanical Engineering, The University of Tokyo, Tokyo 113-8656, Japan
E-mail: s.jeong@mfg.t.u-tokyo.ac.jp

1. Introduction

This study focuses on the fabrication of Laser-Induced Graphene (LIG) from Colorless Polyimide (CPI) films. We examined the graphitization mechanism during laser treatment of CPI using Reactive Force-Field simulations and developed a fabrication method for porous LIG in a single step. The derived LIG's microporous structure, confirmed by multiple characterizations, enhances the performance of pressure sensors and Triboelectric Nanogenerators (TENG). The CPI-derived LIG electrode, with its increased sensitivity, presents promising applications in human motion monitoring systems, wearable devices, and flexible electrodes. The general overview of the experiment is depicted in the Fig.

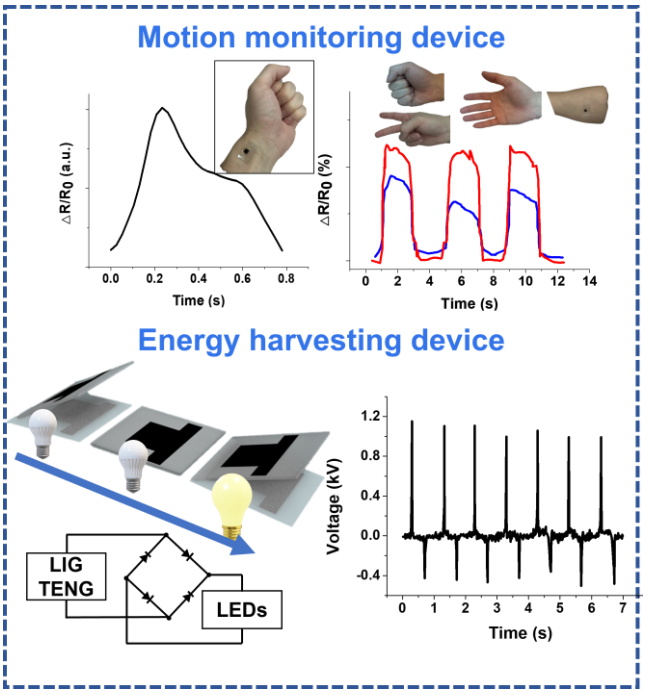

2. Results and Discussion

2.1 Characterization

Our study presents the detailed characterization of CPI-derived LIG using advanced techniques like FE-SEM, EDS, Raman spectroscopy, XRD, and XPS. We found that laser fluences significantly affected LIG surface porosity, with the highest fluence yielding a more porous structure, thereby improving the performance of pressure sensors and TENGs. Raman spectra and XRD highlighted the graphitic and crystalline nature of LIG, respectively. XPS further confirmed the transformation of the polymer to a graphitic structure during laser irradiation.

2.2 ReaxFF simulation

ReaxFF simulations were utilized to investigate the graphitization mechanism of ten distinct CPI-derived LIG formations. Different CPI monomers are divided into two groups based on their fluorine content, and lasing simulation is conducted at ~2500/3000/3500 K. The study records the change in molecular structures, formation of various carbon rings, and gas evolution over time. It is found that under such conditions, amorphous carbon structures transition into planar graphitized structures, producing gases like H_2O and CO. The study also reveals an increase in surface area for CPI monomers with fluorine, suggesting their potential for sensor and energy harvesting applications.

2.3 LIG Pressure sensor

The LIG pressure sensor exhibited high sensitivity and quick response time due to its unique structure, performing well in low-pressure scenarios. Comparative data demonstrated its superiority over other graphene and metal electrode-based sensors. It could accurately detect pressure distribution changes, heart rate, breathing rate, and muscle movement, proving its utility in sports and healthcare, particularly for human motion detection and monitoring. Despite being fabricated in a single step, the sensor showed robust and reliable performance, suggesting significant potential for future applications.

2.4 LIG TENG device

The CPI-derived LIG-based TENG to contribute to sustainable energy solutions. The unique structure and high conductivity of the LIG enhanced TENG performance, which could generate ~1.1kV of open-circuit voltage. The device showed excellent durability and reliability, promising as an alternative power supply for various electronic devices.

3. Conclusions

This study unveils a method to fabricate LIG from CPI films, introducing Fluorine atoms to induce a porous structure, boosting performance of pressure sensors and energy harvesters. The CPI-LIG-based pressure sensor displays high sensitivity and swift response times, showcasing potential for physiological monitoring. Furthermore, the CPI-derived LIG used in a D-D TENG demonstrates substantial power output, reinforcing its applicability in various fields, paving the way for future advancements in energy harvesting and wearable electronics.

Microfluidic biochip of amorphous fluoropolymer CYTOP fabricated using two-photon polymerized 3D mold for high-resolution cell observation

°Kotaro Obata[1], Mirai Hanzawa[1,2], Felix Sima[1,3], Hiroyuki Kawano[1,4], Kazunari Ozasa[1], Yasutaka Hanada[5], Godai Miyaji[2], Atsushi Miyawaki[1,4], and Koji Sugioka[1]

[1]RIKEN RAP, [2]Tokyo Univ. of A. & T., [3]INFLPR, [4]RIKEN CBS, [5]Hirosaki Univ.
E-mail: kobata@riken.jp

Development of biochips which enables distortion-free imaging in the microchannel filled with a culture medium (water) is required to investigate behaviour of living cells in micro and nano environments. Fluoropolymer CYTOP (AGC Corporation) is a promising material with excellent properties such as high transparency in an ultraviolet region, high chemical resistance, and water repellence [1]. More importantly for the high-resolution observation of biological samples, its refractive index (1.34) is almost same as that of water (1.33), which is very attractive to be used as a substrate of biochip. However, its excellent material properties make it difficult to create 3D micro and nanostructures [2]. In this study, we have developed a new 3D fabrication method for CYTOP by using femtosecond laser based two-photon polymerized structures as molds.

Figure 1 shows a schematic diagram of the experimental procedure in order to fabricate an embedded microchannel connected to two open reservoirs. In the experiment, a 3D microstructure was first fabricated by two-photon polymerization (2PP) using a femtosecond laser (wavelength: 515 nm, pulse width: 216 fs) with SU8, a photosensitive resin, drop-casted on a cover glass. After the 2PP process, the fabricated 3D structure was covered with liquid CYTOP and was then thermally treated to cure CYTOP. Finally, 3D SU8 microstructure was dissolved by chemical treatment, resulting in fabrication of 3D CYTOP microstructure. Figure 2(a) shows an optical image of the 3D microfluidic structure fabricated inside CYTOP. The microchannel with a width of 100 µm was observed (upper). When the ethanol was filled into the channel, the boundary of the channel wall disappeared due to good refractive index matching of CYTOP with ethanol whose refractive index is close to water. This result suggests that the 3D CYTOP biochip fabricated by the developed technique is suitable for high-resolution observation of biological samples. Figure 2(b) shows the confocal microscope images of human prostate cancer cells (PC3) observed using the fabricated CYTOP biochips. PC3 cell is entering the microchannel with a width of 10 µm along the sidewall. Refractive index matching between CYTOP and water enables capturing clear images of cells even near the channel sidewall. Thus, excellent microscopic observation of PC3 cells was achieved without image distortion thanks to refractive index matching of CYTOP with the liquid medium (water).

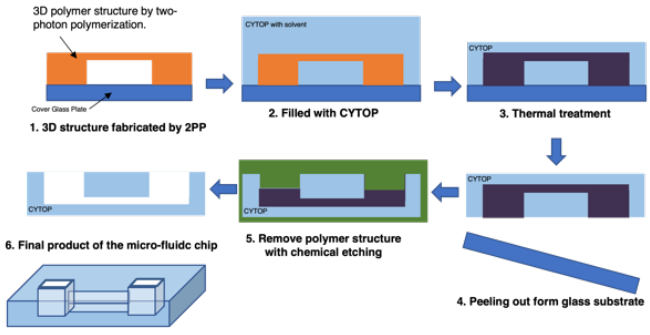

Fig. 1 Schematic illustration of procedure for 3D fabrication of CYTOP.

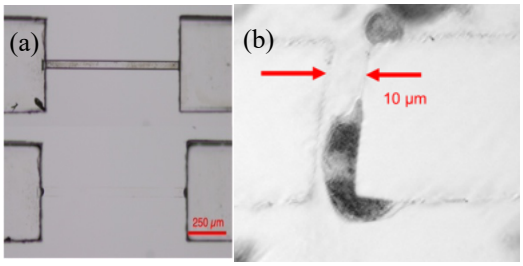

Fig. 2 Optical images of (a) embedded micro-channels in CYTOP filled without (upper) and with (bottom) ethanol and (b) PC3 cell entering the microchannel with width of 10 µm.

Reference
[1] Reports Res. Lab. Asahi Glass Co., Ltd., 55 2005.
[2] Y. Hanada, K. Sugioka, H. Kawano, T. Tsuchimoto, I. Miyamoto, A. Miyawaki and K. Midorikawa, Appl. Surf. Sci., vol.255, pp. 9885-9888 (2009).

Processing of Cultured Animal Cells by Femtosecond Laser Ablation: Toward Development of Compact and Low-cost Processing System for Cell Biology

Kazunori Okano[1,2], Koichiro Kishima[2], Yoichiroh Hosokawa[1]

[1] Nara Institute of Science and Technology, [2] Pinpoint Photonics, Inc.

E-mail: k-okano@ms.naist.jp

1. Introduction

We have reported in single cell processing, manipulating and photoporating of exogenous ionic molecules such as fluorophore dextran with less thermal phenomena of the femtosecond laser. Although we have been developing a series of methodology coupled with femtosecond laser ablation, we are aware that femtosecond laser is difficult to spread widely such the methodologies in biology and medicine because of expensive, necessity of well-trained technicians and researches for optics. The economic and maintenance free system shall be perennially solved to be general methodology. One possibility is to use Q-switch nanosecond lasers that have recently progress, realizing economic, downsizing, and maintenance free system. Here we have a plan to evaluate the feasibility of nanosecond lasers in processing of animal cells, which have been achieved by femtosecond laser ablation. Before the feasibility test, we show progress of femtosecond laser-applied cell scratching and healing of the scratched area and photoporation to different animal cell spices.

2. Experimental

Cell lines of human lung adenocarcinoma (A549) and Madin-Darby canine kidney (MDCK) were cultured to confluence on glass-bottom dish in DMEM, FBS (9% v/v) and antibiotic agents in humid atmosphere having CO_2 (5%) at 37°C. The fs laser (800 nm, 1 kHz, 40-100 nJ/pulse) was scanned at 800 μm/s on the confluent cells where the water ablation threshold was about 40 nJ/pulse.

We examined propidium iodide (PI) uptake of cells. At energy level of water ablation threshold, the fs laser-irradiated cells were stained with PI, indicating cell death and were eventually detached from substrate few hours delay. However, fs laser irradiation at 100 nJ/pulse cause the cells acute wound. After immediate medium change, the cells with the wound were disappeared from the dish surface. The cells adjacent to laser scratched area were stained with PI. It is specially noted that the confluent MDCK like sheet quickly shrank and was flip the sheet edge inward by fs-laser irradiation, while A549 only slightly shrined. Accordingly, the MDCK detached area width was about twice wide of A549 that (Fig.1).

Time-lapse imaging revealed that the scratched area was recovered by 6 h in both A549 and MDCK (Fig. 1). Detailed analysis of the images showed that recovery of the resected area occurred by collective migration, but not by proliferation.

Finally, we applied the fs laser-induced cell removing and the recovering to show a feasibility of our method to evaluate a candidate drug as an anti-cancerous agent. It is known that apigenin is a plant-derived flavonoid and induces apoptosis on the A549 cancerous cells at low dose of several tens μM [2]. Recovery rate under 20 μM of apigenin condition delayed from 2.5 to 4 h to reach half width in preliminary test (Fig. 2).

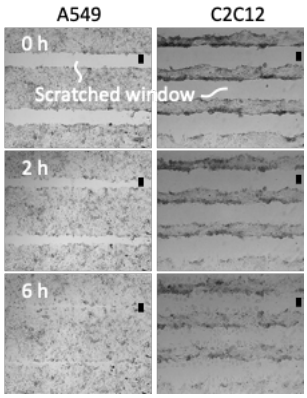

Fig. 1 Time-lapse images of A549 and C2C12 at fs laser scrunching area. Bars indicate scanning width (20 μm).

3. Conclusions

In the present study, we showed the phenomenon occurred on cells cultured to confluent after fs laser irradiation. The intense laser of higher than water ablation threshold induced immediate cell death and the irradiated cells were perfectly removable form the culture substrate by changing medium. The cell removed area on the substrate was refiled with cells by collective cell migration. The fs laser induced cell scrunching have a potential to apply for evaluate drug evaluation. Based on the present study, we have a plan to use a common and small near infrared nanosecond pulse laser having high power for wide spreading of the laser-based scrunching. The system will be down-sized to attach to the conventional biological microscope and be easily handling.

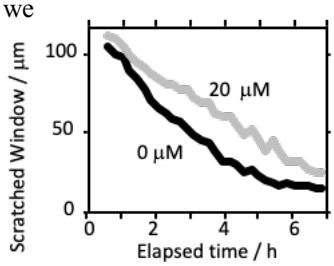

Fig. 2 Effect of apigenin on A549 collective migration on scratched area.

Acknowledgements

This study is supported by Ichimura Foundation for New Technology (2023).

References

[1] K. Okano et al. Biochem. Biophys. Rep. **24** (2020) 100818.
[2] R. Aida et al. Mol. Biol. Rep. 48 (2021) 2291-2297.

[22a-C301-1~4] 4.6 Terahertz Photonics

Hideaki Kitahara(Fukui Univ.)

Fri. Sep 22, 2023 10:00 AM - 11:00 AM C301 (Int'l Ctr.)

△：Presentation by Applicant for JSAP Young Scientists Presentation Award

▲：English Presentation

▼：Both of Above

No Mark：None of Above

▲[22a-C301-1] Real-time data acquisition in THz-TDS using MHz laser repetition rates for lock-in detection

○(PC)Maria Balgos[1], Norihiko Hayazawa[1,2], Masahiko Tani[3], Takuo Tanaka[1,4,5]
（1.Photon Team, RIKEN, 2.SISL, RIKEN, 3.FIR-UF, 4.Mets Lab, RIKEN, 5.Tokushima Univ）

10:00 AM - 10:15 AM

▼[22a-C301-2] Evaluation of Reflective Characteristics of Meta-atoms Employing Point Terahertz Sources and Its Application

○(D)LUWEI ZHENG[1], Kazuki Hara[1], Masayoshi Tonouchi[1], Kazunori Serita[1] （1.Institude of Laser Engineering, Osaka Univ.）

10:15 AM - 10:30 AM

▲[22a-C301-3] Variety of Stokes Beam Generation from Slant-Stripe-Type Periodically Poled Lithium Niobate

○Deepika Yadav[1], Yuma Takida[1], Joselito E. Muldera[1], Hiroaki Minamide[1] （1.RIKEN）

10:30 AM - 10:45 AM

▼[22a-C301-4] Chirp optimization for efficient two-color terahertz generation in gas

○(D)Anna Martinez[1], Said Idlahcen[3], Jonathan Houard[2], Domenico Paparo[1], Angela Vella[2], Ammar Hideur[3] （1.Department of Physics 'E. Pancini", University of Naples "Federico II", Italy, 2.GPM, UMR6634 CNRS, INSA, University of Rouen, France, 3.CORIA, UMR6614 CNRS, France）

10:45 AM - 11:00 AM

Real-time data acquisition in THz-TDS using MHz laser repetition rates for lock-in detection

Maria Herminia Balgos[1], Norihiko Hayazawa[1,2], Masahiko Tani[3], Takuo Tanaka[1,4,5]

[1] Innovative Photon Manipulation Research Team, RIKEN Center for Advanced Photonics, [2] ce and Interface Science Laboratory, RIKEN Cluster for Pioneering Research, [3] Research Center for Development of Far-Infrared Region, University of Fukui, [4] Metamaterials Laboratory, RIKEN Cluster for Pioneering Research, [5] Institute of Post-LED Photonics, Tokushima University

E-mail: mariaherminia.balgos@riken.jp

1. Introduction

Terahertz time domain spectroscopy (THz-TDS), which relies on the coherent detection of terahertz radiation using a pump-probe scheme, is one of the most common techniques to measure optical constants at THz frequencies [1]. Standard lock-in detection is often employed to measure weak THz signals with high signal-to-noise ratio (SNR), For lock-in detection, the signal is modulated at a certain frequency f_{mod}, which is different from the frequencies of unwanted signals. The lock-in amplifier detects and amplifies the signal only at f_{mod} resulting in high SNR. However, data acquisition time is limited by f_{mod}. In particular, the minimum data acquisition time is given by $2/f_{mod}$, as dictated by the Nyquist criterion. Previous reports to modulate the THz signals in THz-TDS mostly utilized optical choppers or AC biased photoconductive antenna (PCA) emitters, with reported modulation frequencies varying from few kHz to few hundreds of kHz, respectively [2,3]. Consequently, the data acquisition times need to be about few milliseconds to few hundreds of microseconds, to get acceptable SNR.

In this work, we introduce the use of the repetition rate of the pump laser to modulate the THz signal at MHz frequencies (Fig. 1a), allowing us to significantly reduce the data acquisition time during lock-in detection [4].

2. Discussion

A home-built THz-TDS system with PCA emitter and detector was used in the experiments. Pump and probe pulses came from a Ti:Sapphire fs laser with 80 MHz repetition rate and 800 nm center wavelength. We varied the pump repetition rate from 1 MHz to 40 MHz using an electro-optic modulator (EOM) operated as a pulse picker, while the probe beam remains at 80 MHz.

A comparison of the THz-TDS spectra acquired using an optical chopper and EOM modulated at 2 kHz and 40 MHz, respectively, is shown in Fig. 1b. At longer time constants from 10 ms to 1 ms, the noise levels between the two measurements are comparable. However, at 500 µs, which is beyond the Nyquist criterion for 2 kHz, significant increase in noise is clearly observed for the spectrum taken using the optical chopper. At 100 µs, the signal is completely lost. In contrast, the signal is still observed at 100 µs for the spectra taken using EOM, because it is still well within the Nyquist limit for 40 MHz. These results showed the possibility of using fast delay scans to map the THz time domain spectrum. We also demonstrate the possibility of real-time signal monitoring using a THz signal varying up to 10 kHz using an acquisition time of 1 µs (Fig. 1c), which is approximately two orders of magnitude faster than previously reported values.

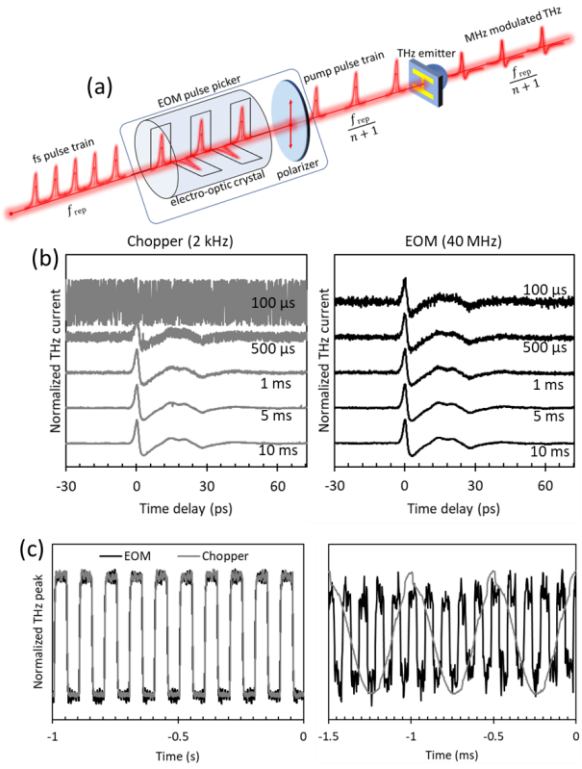

Figure 1.(a) Our proposed scheme for MHz modulation rates. (b) THz-TDS spectra taken using optical chopper and EOM pulse picker modulators. (c) Real-time signal data acquisition for 10 Hz and 10 kHz.

References

[1] J Neu & CA Schmuttenmaer, J. Appl. Phys **124** (2018) 231101
[2] T. Yasui & T. Araki, Jap. J. of Appl. Phys **44.4R** (2005) 1777
[3] LA Sterczewski, et al., Rev. Sci. Instr. **87.1** (2016) 014702
[4] MH. Balgos, N. Hayazawa, M. Tani, and T. Tanaka, Rev. Sci. Instr. **94** (2023) 043002

Evaluation of Reflective Characteristics of Meta-atoms Employing Point Terahertz Sources and Its Application

Osaka Univ. [1], ○Luwei Zheng[1], Kazuki Hara[1], Masayoshi Tonouchi[1], Kazunori Serita[1]

E-mail: serita.kazunori.omp@osaka-u.ac.jp

THz technology has attracted considerable attention as a powerful sensing tool across a wide range of disciplines, including non-invasive/non-destructive detection, biology and material science[1]. Near-field technique[2] with the capability of significantly enhancing the resolution and metamaterials technique[3] with that of remarkably modulating electromagnetic wave properties has considerably facilitated its practical application in the THz band. In fact, we have successfully realized detection of solutes in solutions at the level of several hundred attomoles in picoliter volumes by measuring the resonance frequency shift. However, all results are carried out in transmission mode. And we believe that immense potential in terms of high resolution and high sensitivity features can be implemented in reflection mode.

This study presents an investigation into the reflective properties of terahertz (THz) meta-atoms, which are fundamental components of metamaterials. The evaluation involves the use of point THz sources positioned in the near-field region. The local generation of near-field THz emission is achieved through the process of optical rectification within a non-linear optical crystal, specifically GaAs, under femtosecond laser irradiation at a focused spot. This emission effectively excites the meta-atoms, resulting in a modulation of their resonance states. The reflected THz wave pulses are detected employing a conventional THz time-domain spectroscopy technique. The findings indicate that meta-atoms with diverse configurations exhibit substantial potential for highly sensitive interactions, primarily driven by the electric-field-coupling effect. As a consequence, this phenomenon enables improved spatial resolution and enhanced detection sensitivity. These findings hold significant promise for the advancement of industrial and medical applications, particularly those requiring micro-scale resolution, as well as for the development of THz lab-on-chip devices capable of highly sensitive bio-sensing and trace amount detection.

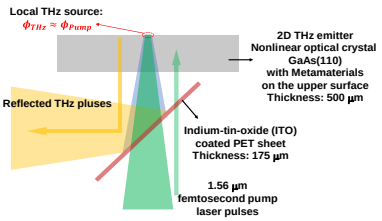

Figure 1. The schematic of the experimental setup.

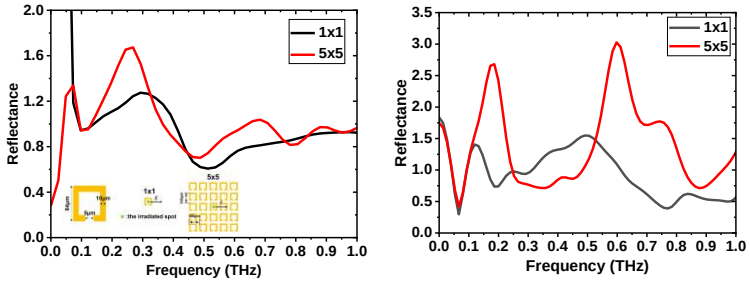

Figure 2. The measured(a) and simulated(b) THz reflectance of arrayed meta-atoms, respectively.

Fig 1 illustrates the schematic of the experimental setup employed in this study. The metamaterial structures are directly fabricated on the surface of a 500-μm-thick GaAs substrate. The size of meta-atom, an elementary unit of metamaterials, is 84μm. The laser beam spot is focused on the center of the center meta-atom region, and it is believed that the diameter of the generated THz beam is almost same as that of the focused laser beam ($\phi 10\,\mu$ m). Fig 2(a) and Fig 2(b) presents the measured and simulated results. The insert demonstrates the employed metamaterial structure of a 1x1 and 5x5 arrays with a period of 100μm. A manifest LC resonance is observed at approximately 0.2 THz, and the experiment and the simulation are in good agreement presenting a great performance for practical applications.

Acknowledgements

This work is supported by JSPS KAKENHI JP20H00247, JP20K20536, JP21H01392, Fusion Oriented Research for disruptive Science and Technology JPMJFR2029, and China Scholarship Council (Grant No. 202206170007).

References

[1] M. Tonouchi, Nature photonics, 1, 97-105(2007).
[2] O. A. Smolyanskaya et al., Progress in Quantum Electronics, 62, 1-77(2018).
[3] J. He et al., Journal of Physics D: Applied Physics, 55, 123002(2021).
[4] K. Serita et al., Journal of Infrared, Millimeter, and Terahertz Waves, 38, 1107-1119(2017).
[5] K. Serita et al., APL Photonics, 3, 051603(2018).
[6] K. Serita et al., Photonics, 6, 12(2019).
[7] K. Serita et al., Journal of Physics: Photonics, 4, 034005(2022).

Variety of Stokes Beam Generation from Slant-Stripe-Type Periodically Poled Lithium Niobate

RIKEN , °Deepika Yadav, Yuma Takida, Joselito E. Muldera, Hiroaki Minamide

E-mail: deepika.yadav@riken.jp

Periodically poled lithium niobate (PPLN) has emerged as a versatile and efficient material for the generation of terahertz (THz)-wave radiation. By making use of its excellent nonlinear optical properties and tailored periodically poled structure for quasi-collinear phase matching (QCPM), a new backward THz-wave parametric oscillator (BW-TPO) was previously realized in a compact, cavity-less setup [1,2]. In this work, we further harness the properties of slant-stripe-type PPLN crystal and show multiple Stokes beam generation at THz frequencies in the backward, forward, and transverse directions.

The experimental setup is shown in Fig.1(a). A laboratory-built Nd:YAG master-oscillator power-amplifier laser system (λ = 1064.44 nm, 0.46 ns, 100 Hz) is used as a pump source and a tunable distributed-feedback laser diode (Innolume DFB-1066-PM-50), serving as injection seeder, are shined onto a slant-stripe-type MgO (5 mol%): PPLN crystal with a pitch of Λ = 35.0 μm, slant angle of α = 67.0° and dimensions of 50 x 5 x 1 mm^3. The spectra of the pump and generated idler beams are given in Fig.1 (b), taken at a pump energy of 8 mJ and seed power of 500 mW. The backward idlers resulting from the main BW-TPO phase-matching, are at λ_1 = 1066.18 nm with a spectral separation from the pump corresponding to the BW-TPO frequency of 0.45 THz. Higher order idlers observed at λ_2 = 1067.91 nm, and λ_3 = 1069.5 nm are due to a cascading process, where one idler acts as the new pump source generating the next order idler, indicating efficient energy conversion. Similar cascading is also observed in the forward direction with a frequency of 1.2 THz. Interestingly, each idler generates a pair (upwards and downwards) of Stokes beams in the transverse direction separated in frequency of 2 THz from the parent idler. The forward and backward measured idler wavelengths are in good agreement with QCPM calculations and the elucidation of the origin of phase matching in the transverse direction is under investigation. The observed frequencies can be easily tuned by rotating the PPLN, as well as by changing the PPLN design parameters (poling period and slant angle), making this a promising source of THz-wave radiation for a variety of applications.

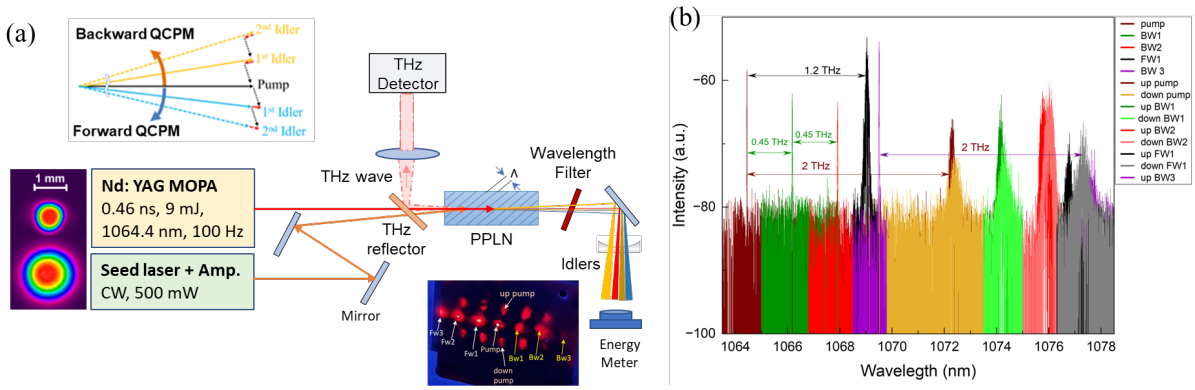

Figure 1: (a) Schematic of the experimental setup, inset on top left shows QCPM scheme for cascaded backward and forward travelling waves, inset on bottom right shows Stokes beams as seen on the IR visualizer (b) measured spectra of various Stokes signals.

References

[1] K. Nawata *et. al*, "Tunable backward terahertz-wave parametric oscillation" Sci. Rep. 9, 726 (2019).
[2] Y. Takida *et. al*, "Injection-seeded backward terahertz-wave parametric oscillator" APL Photonics 5, 061301 (2020).

Acknowledgements

This work was supported (in part) by Japan-China Scientific Cooperation Program between JSPS and NSFC Grant Number JPJSBP120207407, Innovative Science and Technology Initiative for Security Grant Number JPJ004596, ATLA, Japan. The authors express their gratitude to Prof. H. Ito of RIKEN/Tohoku University and Prof. M. Kumano of Tohoku University for the valuable discussions.

Chirp optimization for efficient two-color terahertz generation in gas

Anna Martinez[1], Said Idlahcen[2], Jonathan Houard[3], Domenico Paparo[1], Angela Vella[3], and Ammar Hideur[2]

[1]Dipartimento di Fisica 'E. Pancini', Università 'Federico II', Italy

[2]CORIA, UMR6614 CNRS, France

[3]GPM UMR6634 CNRS, INSA Université de Rouen Normandie, France

E-mail: angela.vella@univ-rouen.fr

Terahertz (THz) emission generated from laser plasma formed by the focusing of two-color femtosecond pulses offers broad emission spectra and relatively high THz peak values, making it a widely used technique. One crucial aspect of optimization is controlling the properties of the THz fields produced, and pulse chirp provides an important means for achieving this. Previous studies, such as the work by Zhang et al. [1], have investigated the influence of chirp on the generated THz intensity. Interestingly, it has been found that the dependence of THz intensity on chirp is non-monotonic. In this contribution, we aim to generalize the results obtained in [1] by considering the simultaneous effect of the phase shift between the first and second harmonics, both on the generation efficiency and on the variation of the THz shape.

The experimental setup utilizes a Spitfire model laser system from Spectra Physics, delivering a 35 fs infrared pulse with a wavelength of 800 nm, a repetition rate of 1 kHz, and a maximum energy of 4 mJ. The laser beam is divided into two parts, with 90% of the energy dedicated to terahertz generation and mechanically chopped at 145 Hz. The remaining 10% of energy is utilized as a probe for the temporal characterization of terahertz pulses in an electro-optic (EO) sampling setup employing a Gallium Phosphide (GaP) crystal. To manipulate the phase shift, we adjusted the position of the Beta-Barium Borate (BBO) crystal relative to the plasma. Additionally, we induced chirp variation by detuning the diffraction grating of the compressor. In Fig.1 we have reported the results obtained, and the variation of the chirp optimization curve as a function of the phase shift is clear (a). It is also clear that a variation of the chirp can induce a variation of the shape of the THz signal (b).

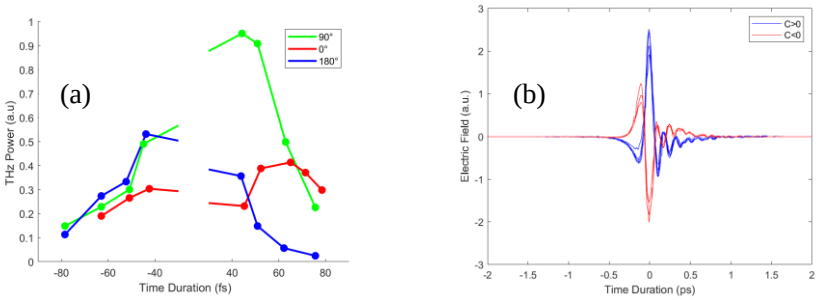

Fig. 1: (a) Variation of the power of the THz electric field with the duration of the FHW at different positions of the BBO crystal.

(b) The THz shape varies depending on the chirp variation, in the figure the phase shift between FHW and SHW is fixed at 0°.

The red curve, representing a 0° phase shift, shows the optimization point at a positive chirp and a phase delay of 65 fs. When aiming for a 90° phase shift, the optimal THz power generation requires a positive chirp and a time duration of approximately 44 fs. Conversely, a 270° phase shift necessitates a negative chirp and a time duration of around 43 fs. This new insight is of utmost importance as it emphasizes that the optimal chirp value is contingent upon the position of the BBO crystal and the specific desired shape of the THz signal we seek to achieve.

[1] Z. Zang, N. Panov, V. Andreeva, et al., *Appl. Phys. Lett.*, vol. 113, 2018.

[22a-A310-1~5] 4.7 Quantum Optics, Nonlinear Optics and Structured Optics

Sunao Kurimura(NIMS)

Fri. Sep 22, 2023 9:00 AM - 10:45 AM A310 (KJ Hall)

△：Presentation by Applicant for JSAP Young Scientists Presentation Award

▲：English Presentation

▼：Both of Above

No Mark：None of Above

▲[22a-A310-1] [JSAP-Optica Joint Symposia 2023 Invited Talk] Quantum information processing with continuous variables over optical fiber

○Kuanshou Zhang[1,2], Jinxia Feng[1,2], Yuanji Li[1,2] （1.State Key Lab. of Quantum Optics and Quantum Optics Devices, Inst. of Opto-Electronics, Shanxi Univ., 2.Collaborative Innovation Center of Extreme Optics, Shanxi Univ.）

9:00 AM - 9:30 AM

▲[22a-A310-2] [JSAP-Optica Joint Symposia 2023 Invited Talk] Versatile quantum state tomography of photonic states via Hong-Ou-Mandel Interference

○Yoshiaki Tsujimoto[1], Rikizo Ikuta[2], Kentaro Wakui[1], Toshiki Kobayashi[2], Mikio Fujiwara[1] （1.NICT, 2.Osaka univ.）

9:30 AM - 10:00 AM

▲[22a-A310-3] Observation of linewidth of electromagnetically induced transparency with temperature

○(D)Anju Pal[1], Ajay Wasan[1] （1.IIT Roorkee）

10:00 AM - 10:15 AM

▼[22a-A310-4] Quantum-enhanced stimulated Raman scattering imaging in dual-polarization scheme

○Zicong Xu[1], Kenichi Oguchi[1], Sho Nitanai[1], Yoshitaka Taguchi[1], Yuki Sano[1], Yasuyuki Ozeki[1] （1.Univ. of Tokyo）

10:15 AM - 10:30 AM

▲[22a-A310-5] Demonstration of Broad and Flat Optical Frequency Comb Generator by Employing Highly Non Linear Optical Fiber

○(DC)PRIYANKA VERMA[1], SUKHBIR SINGH[1] （1.NETAJI SUBHAS UNIVERSITY OF TECHNOLOGY, DWARKA, SECTOR-3, DELHI-110078）

10:30 AM - 10:45 AM

Quantum information processing with continuous variables over optical fiber

Kuanshou Zhang [1,2], Jinxia Feng [1,2], Yuanji Li [1,2]

[1] State Key Laboratory of Quantum Optics and Quantum Optics Devices, institute of Opto-Electronics, Shanxi University, Taiyuan, Shanxi, 030006, People's Republic of China

[2] Collaborative Innovation Center of Extreme Optics, Shanxi University, Taiyuan, Shanxi, 030006, People's Republic of China

E-mail: kuanshou@sxu.edu.cn

Metropolitan fiber quantum communication network is the key step to construct quantum communication network. Owing to continuous variable (CV) quantum entangled states of optical field can be generated unconditionally and deterministically, high-performance quantum information processing with continuous variables based on quantum states of optical field can be achieved. However, quantum information processing with continuous variable over optical fiber is a great challenge.

The entanglement robustness of EPR entangled state distributed over the single-channel and dual-channel optical fiber channel was investigated. It is found that in order to maintain the entanglement robustness of the EPR entangled state in lossy optical fiber channels, the dual-channel scheme has more stringent requirements on the correlation quadrature symmetry and purity of the initial entangled state than the single-channel scheme. In the single-channel scheme, the maximum transmission distance and robustness of the EPR entangled states with asymmetric modes is not sensitive to the asymmetry between modes. The change of asymmetry between modes does not lead to disentanglement. The maximum transmission distance does also not change. Distribution of CV entanglement at a telecommunication wavelength of 1550 nm over single mode fibers are realized experimentally. Entangled beams with quantum entanglement of 8.3 dB is generated using a single nondegenerate optical parametric amplifier based on a type-II periodically poled $KTiOPO_4$ crystal. When one beam of the generated EPR-entangled beams is distributed over 20 km of single mode fiber, 1.02 dB quantum entanglement can still be measured.

A real time deterministic quantum teleportation over a single fiber channel were presented. The effects of the transmission distance, the extra noise in the optical fiber, and the transmission efficiency of the lossy channel on the fidelity of deterministic quantum teleportation over a single optical fiber channel are theoretically analyzed. The real time deterministic quantum teleportation over a single fiber channel by exploiting the generated 1.5 μm EPR entanglement is experimentally implemented. The maximum transmission distance of the deterministic quantum teleportation is 10 km with the fidelity of 0.51 ± 0.01, which is higher than the classical teleportation limit of 1/2.

Versatile quantum state tomography of photonic states via Hong-Ou-Mandel interference

NICT [1], Osaka univ. [2], ◦Yoshiaki Tsujimoto[1], Rikizo Ikuta[2], Kentaro Wakui[1], Toshiki Kobayashi[2] and Mikio Fujiwara[1]
E-mail: tsujimoto@nict.go.jp

Hong-Ou-Mandel (HOM) interference [1] is a bunching phenomenon based on the bosonic nature of photons. When two photons that are perfectly indistinguishable from each other are mixed using a half beam splitter (HBS), they always bunch and exhibit the absence of coincidence resulting in a specific interferogram called HOM dip. The important property of the HOM interference is that the decrease in coincidence reflects the degree of indistinguishability of the input photons, i.e., it provides information regarding the probability of overlap of the input photons. Thus, this property should enable the estimation of a target photon in an unknown quantum state using a probe photon in a known state. In this work, we realize the above concept as the quantum state tomography (QST) applicable to d-dimensional photonic qudits, which we call HOM-QST [2]. Interestingly, we observe that HOM-QST is robust against various imperfections and that the probe photon can be replaced by classical light. Furthermore, we confirm this by demonstrating a proof-of-principle experiment using two-dimensional polarization qubits.

The concept of the HOM-QST is shown in Fig.1(a). For simplicity, we consider the HOM-QST of a polarization qubit as an example. The target photon under test and the probe photon in known polarization state are mixed by a HBS followed by a coincidence measurement. By denoting the polarization of the target photon and probe photon by ρ and k, respectively, the depth of the HOM dip is given by

$$\Delta_k = \frac{\eta n_s n_p}{2}\rho_k$$

where η is a product of the quantum efficiencies of the detectors, n_s and n_p are the average photon numbers of the target photon and probe photon, respectively. $\rho_k = \langle k|\rho|k\rangle$ is the probability of the k-polarized portion of the target photon. Here, $|k\rangle$ is the k-polarized single-photon state. The feature of HOM-QST is that no prior knowledge of the probe light is needed, such as n_p and its intensity correlation function $g^{(2)}(0)$; moreover, there is no theoretical requirement on these values. We perform the proof-of-principle demonstration of the HOM-QST of polarization qubits. We prepare diagonally (D) polarized heralded single photons as the target and compare the estimation results obtained by the conventional QST [3] with HOM-QST using a laser-light probe. The real parts of the reconstructed density matrices are shown in Fig.1 (b) and (c). The estimated fidelity (F) by HOM-QST is above F=0.99. Hence, it is shown that, regardless of the values of n_p and $g^{(2)}(0)$, HOM-QST can realize the precise estimation as our theoretical prediction. Our method serves as an alternative to perform the QST with a passive measurement setup and is applicable to QST of various degrees of freedom.

References

[1] C. K. Hong, Z.Y. Ou and L. Mandel, Phys. Rev. Lett. **59**, 2044 (1987).

[2] Y. Tsujimoto, R. Ikuta, K. Wakui, T. Kobayashi and M. Fujiwara, Phys. Rev. Applied **19**, 014008 (2023).

[3] D. F. V. James, *et al*., Phys. Rev. A **64**, 052312 (2001).

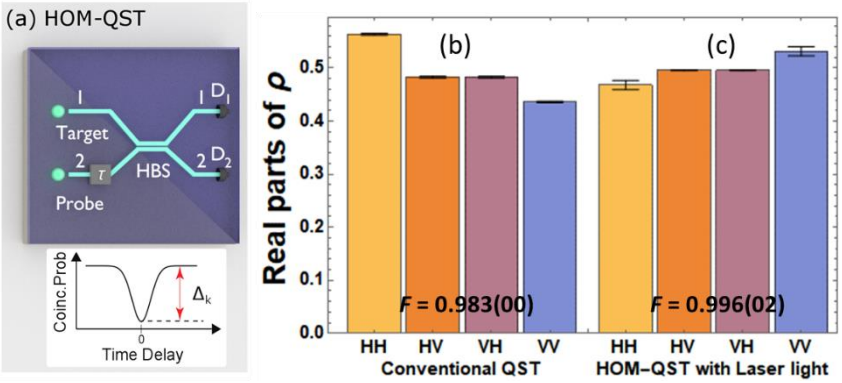

Fig.1 (a) The model of the HOM-QST. (b, c) Estimated density matrices of *D*-polarized target state using conventional QST (b) and HOM-QST with laser-light probe (c). The label "HV" indicates $\mathrm{Re}\langle H|\rho|V\rangle$ for example.

Observation of linewidth of electromagnetically induced transparency with temperature

Anju Pal[1],* and Ajay Wasan[1]
[1]Department of Physics, Indian Institute of Technology, Roorkee, 247667, India
*apal@ph.iitr.ac.in

I. INTRODUCTION

The EIT linewidth plays an important role in high-precision spectroscopy. The EIT linewidth depends on the parameters like laser intensity, doppler broadening and atomic relaxation, etc. In this study, we have observed the dependence of EIT linewidth on the temperature in the D2 transition of ^{87}Rb. The optical density increases with the increase of temperature, which has application in light storage [1], [2].

II. EXPERIMENTAL SETUP

The schematic of the experimental setup and the relevant energy level diagram is shown in Fig. 1 (a and b). In the present experiment, we used two external cavity diode lasers (ECDL) operated independently at wavelength 780 nm as probe and pump lasers. The pump laser was locked at the transition $F_g = 2 \leftrightarrow F_e = 2$ while the probe laser was scanned around the transition $F_g = 1 \leftrightarrow F_e = 2$ as shown in fig.1 (b).

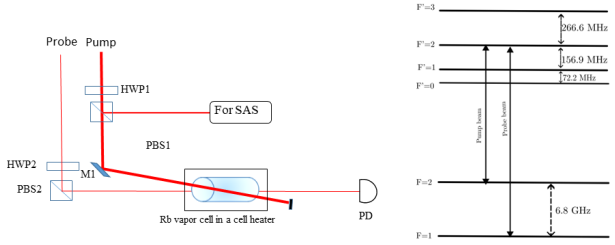

Fig. 1: Schematic diagram of the experimental setup and the corresponding energy level diagram.

Both lasers were passed through the Rb vapor cell in a co-propagating direction. The Rb vapor cell contains both the isotopes of Rb atoms (72% of ^{85}Rb and 28% of ^{87}Rb) and is placed inside a cell heater (THORLABS, GCH25-75). The temperature of the cell heater was controlled using the temperature controller (THORLABS, TC200). After the vapor cell, the probe laser was then monitored by a photodiode and oscilloscope. The probe and pump laser powers was fixed at 0.7 mW and 3.5 mW, respectively.

III. RESULTS AND DISCUSSION

Fig.2 shows the experimentally obtained results in a Λ-type system using D2 transition of ^{87}Rb atoms. To observe the effect of temperature on the EIT, we vary the cell temperature from 22C to 60C. We observed the VSOP dips due to the optical pumping of the pump beam.

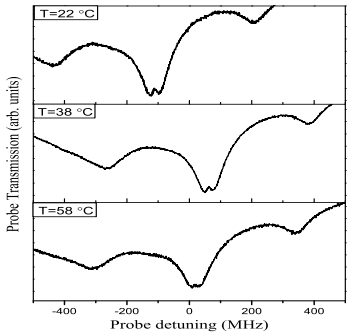

Fig. 2: Experimental results showing probe transmission at different temperatures.

The EIT peak emerged at the central VSOP dip. At a higher temperature, the optical density increases within the cell. So with the increase of optical density, the spontaneously emitted photon increases, which is reabsorbed by the dark state. So the decay rates associated with the ground state increase. Also, atom-atom collision and collision of atoms with the glass cell increases the ground state decay rates. This leads to a reduction in amplitude and an increase in the linewidth of the EIT Window.

IV. CONCLUSION

In conclusion, we have observed the increased amplitude and reduction in linewidth of EIT window with increased cell temperature.

References

[1] Das, Chandan et al., Physica Scripta, 97, 095401, 9 (2022)
[2] Phillips, David F et al., Physical Review Letters, 5, 783 (2008)

Quantum-enhanced stimulated Raman scattering imaging in dual-polarization scheme

Zicong Xu, Kenichi Oguchi, Sho Nitanai, Yoshitaka Taguchi, Yuki Sano, Yasuyuki Ozeki

Research Center for Advanced Science and Technology, The University of Tokyo,
4-6-1 Komaba, Meguro-ku, Tokyo 153-8904, Japan
E-mail: xuzicong19@g.ecc.u-tokyo.ac.jp

1. Introduction

Benefitting from the sub-Poissonian statistics, squeezed light has been applied to push the shot-noise-limited sensitivity of stimulated Raman scattering spectroscopy and microscopy to a sub-shot-noise level [1-4]. To surpass the sensitivity of state-of-the-art SRS microscopes, producing high-power squeezed light is desired. Quantum-enhanced balanced detection offers advantages for high-power operation by combining squeezed vacuum with a high-power local oscillator on a symmetric beamsplitter [5]. However, the balanced detection regime requires a high squeezing level to counteract the 3-dB signal-to-noise ratio (SNR) drawback. In this presentation, we introduce dual-polarization quantum-enhanced stimulated Raman scattering (QESRS), which is also suitable for high-power operation [6]. This approach utilizes a symmetric beamsplitter but detects squeezed light on two independent photodetectors, thus avoiding the 3-dB decrease in SNR.

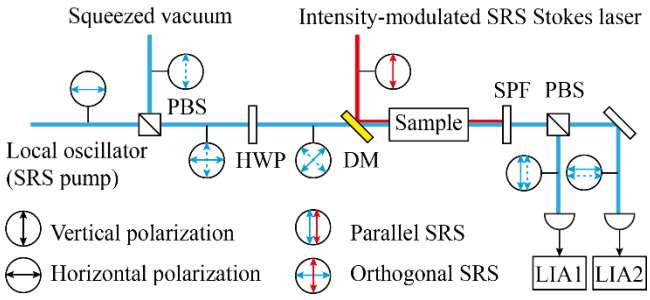

Fig. 1. Schematic of the experimental setup. PBS: polarizing beamsplitter, HWP: half-wave plate, DM: dichroic mirror, SPF: shortpass filter, LIA: lock-in amplifier.

2. Method and experimental setup

Fig. 1 shows the schematic of dual-polarization QESRS. Initially, squeezed vacuum and local oscillator are combined on a polarizing beamsplitter (PBS). The polarizing angles of both are rotated by 45 degrees using a half-wave plate before being directed towards the sample. By introducing an intensity-modulated vertically polarized Stokes laser, parallel and orthogonal SRS can occur simultaneously, resulting in an intensity modulation transferred to the pump laser [7]. At the detection stage, the QESRS signals from the two polarization channels are separated by another PBS and subsequently demodulated by two lock-in amplifiers.

3. Results

Figs. 2(a,b) provide a comparison between classical SRS and QESRS images obtained by blocking or unblocking the squeezed vacuum. The QESRS image demonstrates higher image contrast than the classical one. Figs. 2(c,d) illustrate the noise reduction level of QESRS images at different wavenumbers by sweeping the wavelength of the Stokes laser. Both parallel and orthogonal SRS measurements exhibit an average improvement of 0.5 dB in SNR.

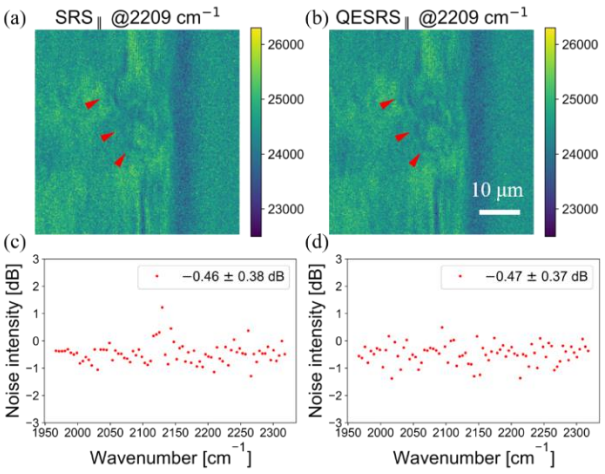

Fig. 2. (a,b) Examples of classical SRS and QESRS images at 2209 cm^{-1} in parallel SRS measurement. (c,d) Plots of noise reduction level at each wavenumber for (c) parallel and (d) orthogonal SRS measurements.

4. Conclusion

In this report, we have presented dual-polarization QESRS that can be operated in a high-power regime (14 mW). We demonstrate the feasibility of achieving sub-shot-noise sensitivity in two polarization channels while achieving a moderate level of noise reduction. This method shows promise for applications in other quantum-enhanced and polarization-resolved measurements as well.

References

[1] R. B. de Andrade, *et al.*, Optica **7**(5), 470 (2020).
[2] C. A. Casacio, *et al.*, Nature **594**(7862), 201 (2021).
[3] Z. Xu, *et al.*, Opt. Express **30**(11), 18589 (2022).
[4] Z. Xu, *et al.*, Opt. Lett. **47**(22), 5829 (2022).
[5] Y. Ozeki, *et al.*, J. Opt. Soc. Am. B **37**(11), 3288 (2020).
[6] Z. Xu, *et al.*, Appl. Phys. Lett., submitted (2023).
[7] J. Shou, *et al.*, Appl. Phys. Lett. **113**(3), 033701 (2018).

Demonstration of Broad and Flat Optical Frequency Comb Generator by Employing Highly Non Linear Optical Fiber

Priyanka Verma[1], Sukhbir Singh[1]
[1]Department of Electronics and Communication Engineering, Netaji Subhas University of Technology, Delhi, India
E-mail: priyanka.verma.phd21@nsut.ac.in

1. Introduction

The optical frequency comb (OFC) is prospective technique that can hike up the communication carrying capability of wide range in optical fiber communication [1]. Due to its numerous applications, including ultra-short pulse generation for different wavelength [2] multi-wavelength ultra-fast photonic signal processing, high-accuracy optoelectronic detectors and wavelength division multiplexing [3, 4], it draws attention of researchers. A collection of spectral lines is produced by a continuous laser source modulating a radio frequency signal. This manuscript proposed an effective technique for generation of OFC with cascading of modulators with Highly Nonlinear Fiber (HNLF) that produces coherent and highly spectral comb lines.

2. Proposed system setup for OFC

The CW laser pump depicts in Fig.1 at 1553nm produce unmodulated signal which passes through Electro Absorption Modulator (EAM) to enhance the intensity of laser light with 10GHz RF Source. The shape of spectrum get further enhanced by cascading of two Mach Zehnder Modulator (MZM) at -1V and 4V biasing voltage. The modulator 1 is intensity modulator, however modulator 2 work as phase modulator. The electrical inputs of MZM such as V_{DC} and V_{RF} drive two phase shifters to modulate E_{in} into two arms of modulator which are recombined to give E_{out} where γ is power splitting ratio. This is governed by equation given by (1) [5].

$$Eout(t) = \frac{Ein}{2}\left[\gamma e^{j\pi\left(\frac{VRF(t)}{V\pi RF}+\frac{Vdc}{V\pi dc1}\right)}+(1-\gamma)e^{j\pi\frac{-VRF(t)}{V\pi RF}}\right] \quad (1)$$

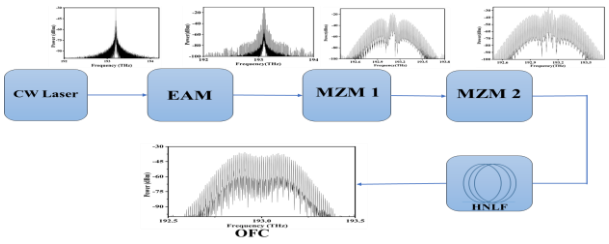

Fig. 1 OFC Generation by employing HNLF

The pulse train gets enhanced with nonlinear index of refraction of HNLF which gives additional optical spectral lines over a high bandwidth range which is governed in equation (2), where γ represents fiber nonlinear coefficient, n_2 is nonlinear index of refraction whereas A_{eff} is effective area of optical fiber and λ is operating wavelength.

$$\gamma = \frac{2\pi n_2}{\lambda A_{eff}} \quad (2)$$

3. Result and Discussion

The performance of generated optical frequency comb is analyzed with Optical Spectrum Analyzer (OSA) in optisystem. The stability is improved with cascading of modulator with RF source of 30GHz. The output spectrum at cascading of modulators is illustrated in Fig. 2 (a) & (b) respectively.

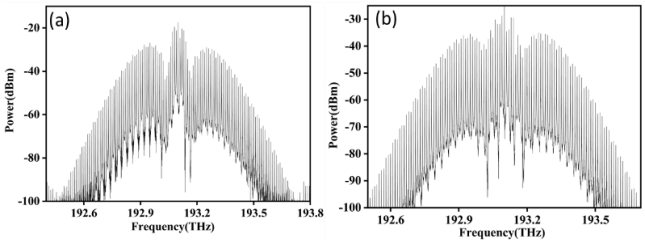

Fig. 2 Modulated Spectrum at (a) MZM 1(b) MZM 2.

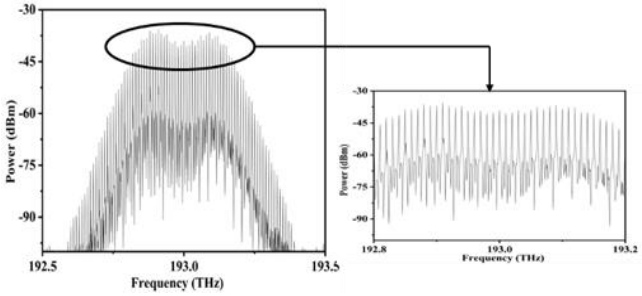

Fig. 3 Optical Frequency Comb Generation at Output of HNLF

The Fig.3 depicts generated OFC at output of HNLF. The obtained comb lines are 45 which is shown in circular image with 3dB flatness.

4. Conclusion

The proposed technique is effective with 45 numbers of comb lines and 3dB maximum power deviation. HNLF plays a vital role by enabling the nonlinear process that broadens and spread the spectral energy resulting in a comb like structure with evenly spaced frequency lines. The comb generated is valuable for a variety of applications such as frequency metrology and communication network.

References

[1] A. Parriaux, K. Hammani, and G. Millot, "Electro-optic frequency combs," *Advances in Optics and Photonics*, vol. 12, pp. 223-287, 2020.
[2] T. Yang, J. Dong, S. Liao, D. Huang, and X. Zhang, "Comparison analysis of optical frequency comb generation with nonlinear effects in highly nonlinear fibers," *Optics express*, vol. 21, pp. 8508-8520, 2013.
[3] R. Ullah, B. Liu, Q. Zhang, Q. Tian, F. Tian, Z. Qu, *et al.*, "Optical frequency comb generation with high tone-to-noise ratio for large-capacity wavelength division multiplexed passive optical network," *Optical Engineering*, vol. 54, pp. 116102-116102, 2015.
[4] C. Lei, H. Chen, M. Chen, S. Yang, and S. Xie, "Recirculating frequency shifting based wideband optical frequency comb generation by phase coherence control," *IEEE Photonics Journal*, vol. 7, pp. 1-7, 2014.
[5] J. Cartledge, C. Rolland, S. Lemerle, and A. Solheim, "Theoretical performance of 10 Gb/s lightwave systems using a III-V semiconductor Mach-Zehnder modulator," *IEEE photonics technology letters*, vol. 6, pp. 282-284, 1994.

[23a-A310-1~7] 4.7 Quantum Optics, Nonlinear Optics and Structured Optics

Takashige Omatsu(Chiba Univ.), Sunao Kurimura(NIMS)

Sat. Sep 23, 2023 9:00 AM - 11:00 AM A310 (KJ Hall)

△：Presentation by Applicant for JSAP Young Scientists Presentation Award

▲：English Presentation

▼：Both of Above

No Mark：None of Above

▲[23a-A310-1] [JSAP-Optica Joint Symposia 2023 Invited Talk] Structured light generations from cylindrically Structured Crystals

○Jingbo Sun[1] （1.Tsinghua University）

9:00 AM - 9:30 AM

▲[23a-A310-2] Scintillation index evolution of chirped ring Pearcey vortex beam through atmospheric turbulence

○(D)Shakti Singh[1], Sanjay Kumar Mishra[2], Akhilesh Kumar Mishra[1] （1.IIT Roorkee India, 2.IRDE, Dehradun, India）

9:30 AM - 9:45 AM

▲[23a-A310-3] 2D mapping of optical vortices

○(DC)Dina Grace Calbero Banguilan[1], Nathaniel Hermosa[1] （1.UP Diliman）

9:45 AM - 10:00 AM

▲[23a-A310-4] Enhancing Nonlinear Signals of Blood Plasma in the Z-scan Technique Using Copper Nanoparticles

○Mustabi Mustafa Chowdhury[1], Yasmeen Haque[1], Md. Enamul Hoque[1] （1.SUST）

10:00 AM - 10:15 AM

▲[23a-A310-5] Optical-skyrmions induced exotic surface structures of azo-polymers

○(D)Rihito Tamura[1], Praveen Kumar[2], A. Srinivasa Rao[1,3,4], Katsuhiko Miyamoto[1,3], Omatsu Takashige[1,3] （1.Chiba Univ, 2.IIT Bhilai, 3.MCRC, Chiba Univ, 4.Chiba Univ. IAAR）

10:15 AM - 10:30 AM

▲[23a-A310-6] Riccati Generalization of Optical Rogue waves

○(DC)Sanjana Bhatia[1], C.N. Kumar[1] （1.Panjab University, Chandigarh, India）

10:30 AM - 10:45 AM

▲[23a-A310-7] Direct generation of orange and red 1st order Bessel-like beams using Pr fiber

○Yuto Yoneda[1], Srinvasa Rao Allam[1], Yasushi Fujimoto[2], Katsuhiko Miyamoto[1], Takashige Omatsu[1] （1.Chiba Univ., 2.CIT）

10:45 AM - 11:00 AM

Structured light generations from cylindrically Structured Crystals

Jingbo Sun*

E-mail: jingbosun@tsinghua.edu.cn

Abstract: Spherulites are crystals with cylindrical crystalline structures and thus exhibit anisotropic optical properties with cylindrical symmetry. Here we show several intriguing designs of the devices including the generation and the modulations on the cylindrical beams with spherulites in both linear and nonlinear ways. Such a kind of naturally existed circular anisotropy opens entirely new opportunities in the field of the structured light applications.

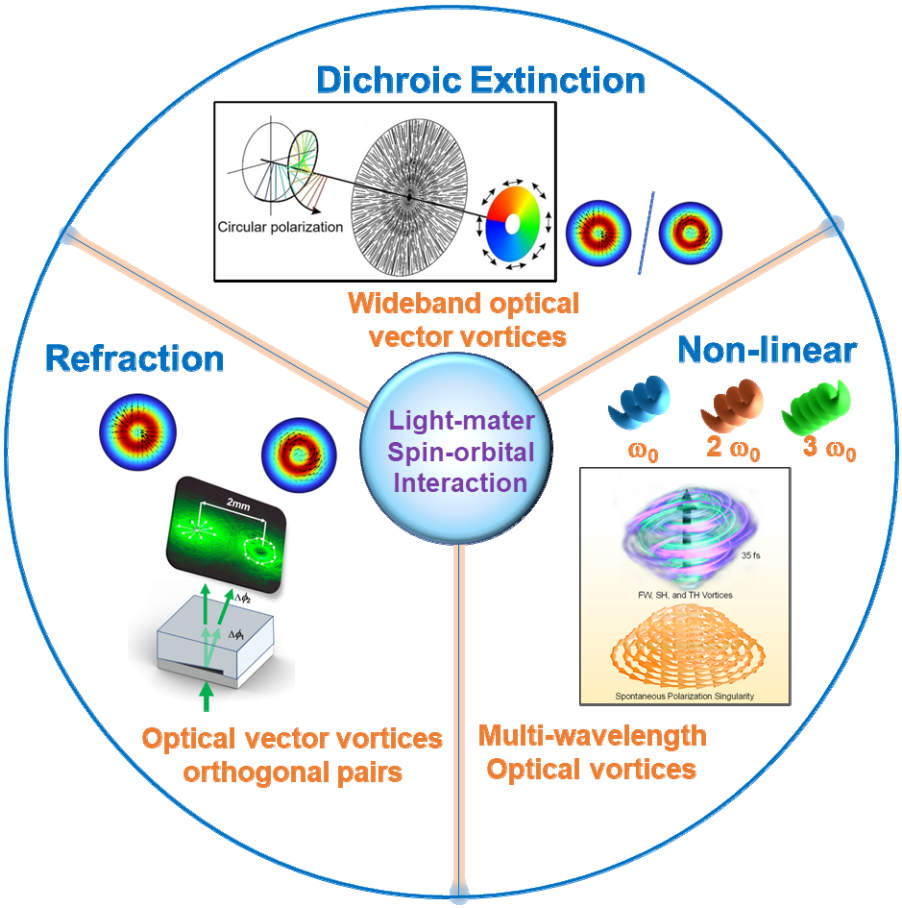

Fig.1 Structured light generations by using spherulites that have cylindrical crystal structures.

Scintillation index evolution of chirped ring Pearcey vortex beam through atmospheric turbulence

Shakti Singh[1], Sanjay Kumar Mishra[2], Akhilesh Kumar Mishra[1,*]
[1]Department of Physics, Indian Institute of Technology Roorkee, Roorkee-247667, India
[2]Photonics Division, Instruments Research and Development Establishment, Dehradun-248008, India
[*]Corresponding author: akhilesh.mishra@ph.iitr.ac.in

1. Introduction

The research field of abruptly autofocusing (AAF) beam is witnessing a great surge of attention due to its unique properties such as self-healing, non-diffracting nature among others [1]. AAF beams with orbital angular momentum (OAM) [2] hold applications in free space optical communication (FSO) [3] due to its additional degree of freedom.

2. Numerical Modelling

To model the phase screen mimicking turbulence, we have used Von Karman power spectral density (PSD), whose mathematical expression is given by [4]

$$\phi_n(\kappa) = 0.033 c_n^2 (\kappa^2 + \kappa_0^2)^{-11/6} \, exp\left(\frac{-\kappa^2}{\kappa_m^2}\right), \quad (1)$$

where c_n^2 represents the represents the strength of atmospheric turbulence, $\kappa_0 = \frac{2\pi}{L_0}$ and $\kappa_m = \frac{5.92}{l_0}$, where L_0 represents the outer scale and l_0 represents the inner scale of the atmospheric turbulence. Input field profile of chirped ring Pearcey vortex beam (CRPVB) is given by

$$E(r, \phi, 0) = Pe\left(\frac{-r}{w_0}, \zeta_0\right) exp\left[b\left(\frac{-r}{w_0}\right)\right] \exp(il\phi) \, exp\left(ic\left(\frac{-r}{w_0}\right)^2\right), \quad (2)$$

where Pe is the Pearcey function, whose expression is given by

$$Pe(x, y) = \int_{-\infty}^{\infty} \exp\left(is^4 + is^2 x + isy\right) ds, \quad (3)$$

here x and y are dimensionless variables, w_0 is the width of the beam, b is the truncation factor, c is chirp parameter, ζ_0 denotes a constant and l is the value of topological charge.

3. Results and Discussion

In our numerical simulation we have considered $l = 2, w_0 = 3\ cm$, $N = 512$, $\zeta_0 = 0$, wavelength $\lambda = 2\ \mu m$, $l_0 = 1\ cm$, $L_0 = 3\ m$ and $b = 0.1$. The propagation of CRPVB up to $2\ km$ is simulated in atmospheric turbulence by using 20 random phase screens at an interval of $100\ m$. To provide the sufficient statistics 500 independent realizations have been performed. We have calculated apertured average scintillation index (SI) using formula [5]

$$SI(z) = \frac{\langle \left(\int_{-R}^{R} \int_{-R}^{R} I(x,y,z) dx dy \right)^2 \rangle}{\langle \int_{-R}^{R} \int_{-R}^{R} I(x,y,z) dx dy \rangle^2} - 1, \quad (4)$$

where I is the intensity of the beam and we have considered the radius of receiving aperture $R = 5$ cm for the present numerical investigation.

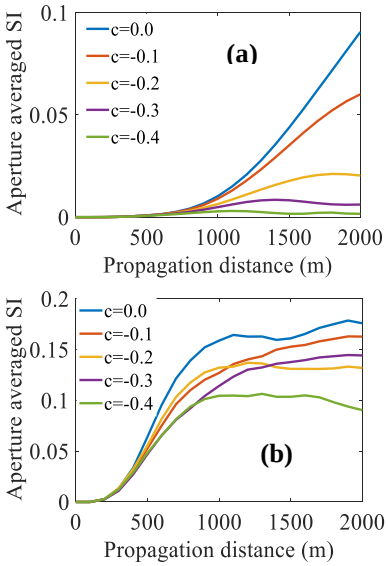

Fig. 1. Apertured average SI for CRPVB for moderate (a) $C_n^2 = 10^{-14} m^{-2/3}$ and strong (b) $C_n^2 = 10^{-12} m^{-2/3}$ turbulence parameters.

In figure 1(a) and 1(b), we observe that on decreasing the value of chirp parameter (increasing the value of the negative chirp) apertured average SI decreases in both weak and strong turbulence.

4. Conclusion

We have found that on decreasing the value of chirp parameters, aperture averaged SI decreases in both weak and strong turbulence, which proves the robustness of CRPVB against atmospheric turbulence.

5. References

[1] D. G. Papazoglou, N. K. Efremidis, D. N. Christodoulides, and S. Tzortzakis, Opt. Lett. 36(10), 1842–1844 (2011).
[2] S Singh and A K Mishra, J. Opt. 24, 075501 (2022).
[3] A. E. Willner, K. Pang and H. Song, Appl. Phys. Rev. 8, 041312 (2021)
[4] K. Khare, P. Lochab and P. Senthilkumaran, "Orbital Angular Momentum States of Light Propagation through atmospheric turbulence" IOP Publishing (2020)
[5] S. Singh, S.K. Mishra, and A. K. Mishra, arXiv. 2205.10771, (2022)

2D mapping of optical vortices

Dina Grace C. Banguilan *, Nathaniel P. Hermosa II
National Institute of Physics, University of the Philippines Diliman, Quezon City, 1101 Philippines
E-mail: dbanguilan@nip.upd.edu.ph

An optical vortex occurs when the real and imaginary parts of a complex electromagnetic wave field become zero, and the phase becomes singular at the beam's center. The light around a beam containing OVs carries a topological charge m [1]. However, higher-order vortices |m| >1 are inherently unstable that they tend to separate in a series of vortices with a unity charge. Here, we demonstrate a technique to locate optical vortices using light's diffraction by a triangular aperture.

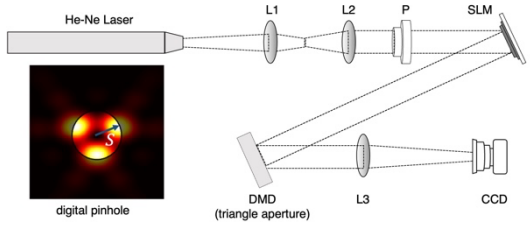

Figure 1. The diffraction of a vortex beam through a triangular aperture was captured using a CCD camera.

Our experimental setup involves a He-Ne laser directed towards a spatial light modulator (SLM), where optical vortices are generated. We select the first-order mode and allow it to propagate until it reaches a triangular aperture programmed in a digital micromirror device (DMD). We move the triangular aperture across the laser beam in two dimensions and record the corresponding pattern using a charged coupled device (CCD). According to Hickman et al., the diffraction produced by a single charge vortex displays a distinct dark region at its center [2]. This characteristic is shared with an optical vortex, which emerges at positions where the complex field amplitude is zero. Using this similarity, we introduce a digital pinhole to measure the intensity signal at the center of the recorded pattern. The pinhole size, S, can be controlled using the formula $S = f\lambda / \pi R$, where f represents the focal length of the Fourier lens, λ is the laser's wavelength, and R corresponds to the radius of the triangular aperture. By plotting the intensity values transmitted through the pinhole for various scanning points, we can identify the lowest intensity region on the map, which indicates the presence of a vortex. First, we optimize the pinhole because as seen in Figure 1, pinhole S still captures high-intensity values from the pattern's bright lobes. We found in single vortex detection that pinhole with size $S/3$ can make more precise measurement of the central intensity. Figure 2a illustrates the intensities measured by this pinhole from patterns generated by a single vortex initially located at the origin (x,y) = (0,0). However, based on the measured lowest-intensity values, we determine that the vortex is now positioned at (x,y) = (0.86 μm,0). We further investigate our technique in detecting two vortices. As a proof-of-concept, we initially place two vortices symmetrically about the host Gaussian beam center such that $|m_1| = 1$ lies at $(x_1, y_1) = (-0.49\ \text{mm}, 0)$ and $|m_2| = 1$ at $(x_2, y_2) = (+0.49\ \text{mm}, 0)$. Using the pinhole, we found the vortices at $(x_{m_1}, y_{m_2}) = (-0.86\ \text{mm}, 0.17\ \text{mm})$ and $(x_{m_2}, y_{m_2}) = (1.21\ \text{mm}, -0.17\ \text{mm})$, as shown in Figure 2b. As a side note, the transmitted signal captured by the pinhole offer insights into the dynamic behavior of the interacting vortices. We observe that the vortices drifted away from their initial locations but rotate around a common axis, consistent with the initial findings of Rozas [3].

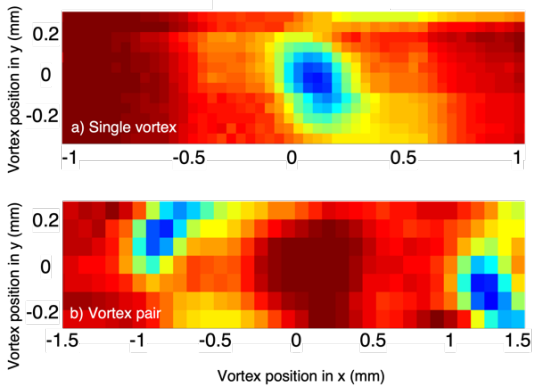

Figure 2. a) Single vortex and b) vortex pair position as measured by a pinhole with size $S/3$.

In conclusion, we have demonstrated that we can determine the position of a vortex carrying a topological charge using the diffraction of light by a triangular aperture. By measuring the intensity at the center of the diffraction using a digital pinhole, we can also resolve vortex pairs that are more than 86.4μm apart.

Acknowledgement
D.G.C. Banguilan was a scholar of the DOST-SEI thru its Accelerated Science and Technology Human Resource Development Program.

References

[1] L. Allen, M. W. Beijersbergen, R. Spreeuw, and J. Woerdman, Phys. Rev. A 45 (1992) 8185.
[2] J. M. Hickmann, E. J. S. Fonseca, W. C. Soares, and S. Chavez- Cerda, Phys. Rev. Lett. 105 (2010) 053904.
[3] D. Rozas, C. T. Law, and G. A. Swartzlander JOSA B 14.11 (1997) 3054-306

Enhancing Nonlinear Signals of Blood Plasma in the Z-scan Technique Using Copper Nanoparticles

Mustabi Mustafa Chowdhury[1], Yasmeen Haque[1], Md. Enamul Hoque*[1]
Department of Physics, Shahjalal University of Science and Technology, Sylhet - 3114, Bangladesh
*Corresponding Author: mjonyh-phy@sust.edu

Abstract: We incorporated pulsed laser ablated copper nanoparticles of indirect bandgap 2.05 ±0.05 eV to enhance the nonlinear optical signal of blood plasma in the Z-scan technique. The nonlinear signal of blood plasma (phase shift = 0.49) has been enhanced at about 114% by mixing with copper nanoparticles.

Introduction: Copper nanoparticles (Cu-NPs) with a reported bandgap of 1.3 - 2.1 eV [1] are very common due to their nontoxicity and abundance making them a cheap material for many biomedical applications [2]. Previously it was found that blood plasma produces a signature nonlinear Z-scan profile which can be enhanced by mixing with iron nanoparticles (Fe-NPs) as the bandgap energy of Fe-NPs (2.1eV) remains close to the energy of the incident laser in the Z-scan [3]. In this study, we aim to investigate the enhancement of blood plasma signals using Cu-NPs prepared through the pulsed laser ablation technique. By incorporating these copper nanoparticles into blood plasma samples, we will examine the Z-scan profiles at different incident power levels. The objective is to explore how the presence of Cu-NPs affects the nonlinear refractive index and enhances the signal response in blood plasma.

Methodology: We prepared the copper nano-colloids by immersing a copper slab in distilled water and irradiating it with an Nd:YAG Laser (532nm, 10ns, 260mJ/pulse). The Z-scan technique was then employed using a 660 nm laser to analyze three samples: (a) Cu nano-colloids, (b) blood plasma, and (c) a 50% v/v mixture of Cu nano-colloids and blood plasma.

Results and Discussions: From the UV-Vis spectroscopy, we observed the absorption peak of copper nano-colloids at 216nm (fig. 1a). Using Tauc's formula, the indirect bandgap was determined to be 2.05 ± 0.05 eV, which aligns with previous research findings [1]. When subjected to different laser power levels, copper nanoparticles exhibited nonlinear responses (fig. 1b), At an incident power of 39.38mW, the normalized phase shifts for copper NPs and blood plasma samples were 0.12 and 0.49, respectively. However, when the Cu NPs were mixed with blood plasma, the normalized phase shift (Δφ) increased significantly to 1.05, representing a 114% enhancement compared to the blood plasma. This enhancement was consistently observed across eight different incident power levels (fig. 1c).

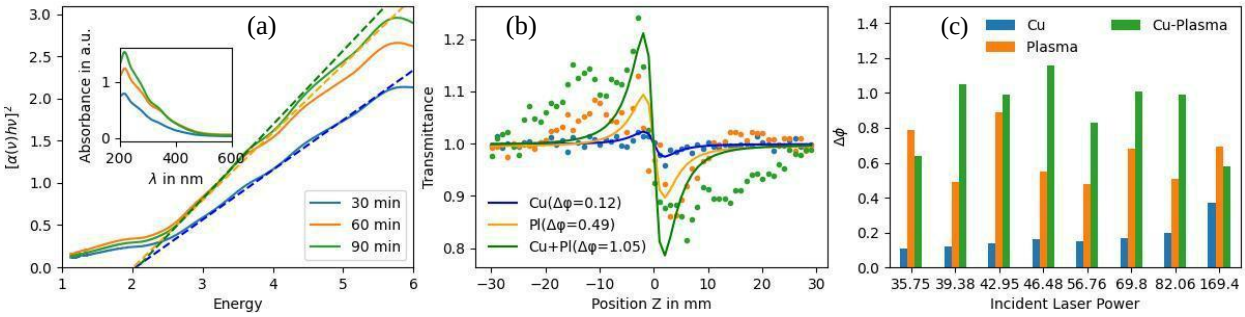

Fig. 1: Illustration of the key findings of this study. (a) The Tauc plot presents the evaluation of the indirect bandgap of Cu-NPs at three different ablation durations, obtained from the UV-Vis absorption spectrum (inset). (b) demonstrates of the enhancement of the normalized transmittance of the blood plasma signal achieved by the presence of copper nano-colloids. Finally, (c) showcases the enhancement of the Z-scan measurement at different incident laser power levels.

Conclusions: The incorporation of copper nanoparticles with an indirect bandgap of 2.05 ± 0.05 eV, corresponding to the wavelength of the incident laser, has successfully enhanced the nonlinear optical phase shift of blood plasma in the Z-scan technique. This enhancement aligns with similar observations made with iron nanoparticles, which possess a bandgap of 2.1 eV that also matches the incident laser wavelength. These findings demonstrate that particles with bandgaps matching the laser wavelength can effectively enhance the nonlinear signal of plasma samples in the Z-scan technique. Such knowledge opens up possibilities for optimizing the design and selection of nanoparticles to maximize the enhancement of nonlinear signals in various biomedical applications.

Reference: 1. Marabelli, F., G. B. Parravicini, and F. Salghetti-Drioli. "Optical gap of CuO." *Physical Review B* 52.3 (1995): 1433.
2. Milenkovic, Jelena, et al. "Bactericidal activity of Cu-, Zn-, and Ag-containing zeolites toward Escherichia coli isolates." *Environmental Science and Pollution Research* 24 (2017): 20273-20281.
3. Chowdhury, Mustabi Mustafa, Yasmeen Haque, and Md Enamul Hoque. "Enhancement of Nonlinear Optical Phase Shift of Blood Plasma with Iron Nano-colloids in the Z-scan Technique." *Photonic Networks and Devices*. Optica Publishing Group, 2022.

Optical-skyrmions induced exotic surface structures of azo-polymers

Chiba Univ. [1], Indian Institute of Technology Bhilai [2], Chiba Univ. MCRC [3], Chiba Univ. IAAR[4]

○(D1) Rihito Tamura[1], Praveen Kumar[2], A. Srinivasa Rao[1,3,4],

Katsuhiko Miyamoto[1,3], Takashige Omatsu [1,3]

E-mail: omatsu@faculty.chiba-u.jp

Optical skyrmions [1], in which all polarization states mapped on the Poincaré sphere are projected onto the beam cross-section, have attracted much attention as analogous magnetic skyrmions. Versatile optical skyrmions, such as Néel-, Bloch-, Anti-, and even Hopfion-skyrmions, have been proposed, however, there have been no reports of their polarization textures being transferred to materials, so far.

We herein report on the first demonstration of direct imprinting of the polarization textures of optical skyrmions onto azo-polymers [2] via photo-induced surface reliefs.

Figure 1 shows a schematic diagram of an experimental setup for an optical skyrmion generator based on a single-path self-referenced polarization interferometer with a spatial light modulator (SLM). A continuous-wave green laser (wavelength 532 nm) was used, and its output was incident onto the SLM. The laser output exhibited a linear polarization inclined 45° with respect to a slow axis of *x*-axis, thus converting its *x*-polarized component to be a 1st order Laguerre-Gaussian (LG) mode. After passing through a relay optics and a half-wave plate (the polarization of the laser output was rotated by 90°), the modulated laser output was re-injected into the SLM. A relative phase of *y*-polarized Gaussian mode to the *x*-polarized LG mode was then controlled. Also, the LG and Gaussian modes with orthogonal circular polarizations were coherently superposed with each other by a quarter-wave plate, thereby allowing the generation of the 1st order Néel-, Bloch-, and Anti-optical skyrmions.

The skyrmion numbers of generated Néel-, Bloch-, and Anti-optical skyrmions were estimated to be 0.99, 0.98, and -0.98, respectively, close to an ideal number of 1, thus ensuring the generation of high-quality optical skyrmions (Fig. 2).

The generated optical skyrmions were focused to be ~7 μm spot by a lens (NA~0.5) on an azo-polymer thin film. Laser power and exposure time of optical skyrmions were then fixed to be 100 μW and 30 seconds, respectively. Intriguingly, the photo-induced mass transport of azo-polymers occurs along the perpendicular direction to the polarization of the irradiated optical skyrmions, thereby forming surface relief structures with the polarization textures of optical skyrmions (Fig. 2).

Our demonstration will offer a new fundamental physics of interactions between optical polarization textures and matter, and advanced optical data storage devices with the freedom of skyrmion states.

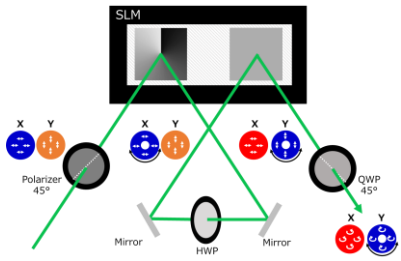

Figure. 1. Optical skyrmion generator based on a SLM with a self-interferometer configuration.

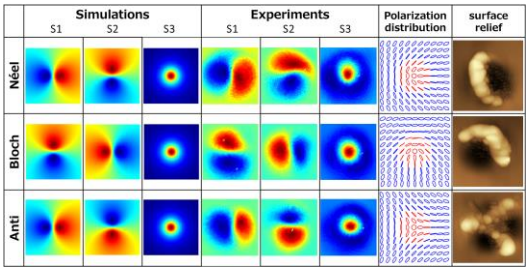

Figure. 2. Simulated and experimental Stokes parameters (S1, S2, S3), polarization distribution, and surface reliefs of optical skyrmions.

References

[1] D. Sugic, R. Droop, E. Otte, D. Ehrmanntraut, F. Nori, J. Ruostekoski, C. Denz, M. R. Dennis, Nat. Commun. 12, 6785-6795 (2021).

[2] T. Omatsu, K. Masuda, K. Miyamoto, K. Toyoda, N. M. Litchinitser, Y. Arita, K. Dholakia, J. Nanophotonics 14, 010901 (2020).

Riccati Generalization of Optical Rogue waves

Sanjana Bhatia[1], **and C. N. Kumar**[1]

[1]*Department of Physics, Panjab University, Chandigarh-160014, India*

E-mail: sanjana.bhatia577@gmail.com

"Rogue waves", "freak waves" and "killer waves", refer to giant isolated waves that appear from nowhere, having amplitudes significantly larger than the background waves. Firstly observed in the oceans as extreme water waves, rogue waves (RWs) are ubiquitous in nature and appear in various contexts such as nonlinear optical systems, Bose-Einstein condensates, microwave cavities, etc. In particular, the study of rogue waves has gained fundamental significance in nonlinear optical systems, because of its potential applications in producing high-intensity optical pulses. Several models have been developed to study the dynamics of RWs, the nonlinear Schrödinger equation (NLSE) being the most studied one [1].

A significant aspect of the implementation of RWs in the communication industry is the manipulation of features like amplitude, speed etc. Recently, Dai and his collaborators have studied the dynamics of controllable rogue waves, modeled by variable coefficient NLSE, through dispersion and nonlinearity management [2]. Authors in [3] have shown that the equation governing rogue wave dynamics admits a wide class of self-similar solutions, whose amplitudes can be exactly controlled by tailoring gain and tapering profiles in optical fibers through a free parameter using the isospectral hamiltonian technique. In the present work, we extend this class of solutions, to control the amplitude by tailoring the gain and tapering profiles through two free parameters. In the paraxial regime, the beam propagation is governed by the inhomogeneous NLSE given by

$$i\frac{\partial U}{\partial Z}+\frac{1}{2}\frac{\partial^2 U}{\partial X^2}+F(Z)\frac{X^2}{2}U-\frac{i}{2}G(Z)U+|U|^2U=0, \tag{1}$$

where $U(X,Z)$ represents the dimensionless complex field envelope, $F(Z)$ is the graded-index profile, and $G(Z)$ is the linear gain/loss function. Fig. 1 demonstrates the effect of

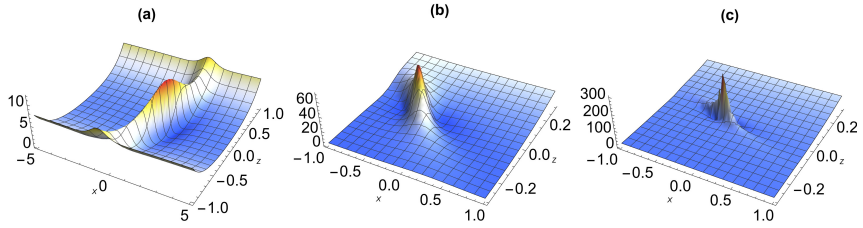

Figure 1: (a) Rogue wave intensity corresponding for undeformed case. Rogue wave intensity for (b) $\lambda_1, \lambda_2 = (0.1, -1.1)$ (c) $\lambda_1, \lambda_2 = (1, -1.1)$

Riccati parameters (λ_1, λ_2) on intensity of the RW. It can be observed that the height of the RW can be effectively controlled through judicious combination of (λ_1, λ_2), increasing **up to 30 times** in Fig. 1(c).

[1] N. Akhmediev, A. Ankiewicz, and M. Taki, " Waves that appear from nowhere and disappear without a trace", Phys. Lett. A **373**, 675 (2009).

[2] C. Q. Dai, Y. Y. Wang, Q. Tian, and J. F. Zhang, " The management and containment of self-similar rogue waves in the inhomogeneous nonlinear Schrödinger equation", Ann. Phys. **327**, 512 (2012).

[3] C. N. Kumar, R. Gupta, A. Goyal, and S. Loomba, " Controlled giant rogue waves in nonlinear fiber optics", Phys. Rev. A **86**, 025802 (2012).

Direct generation of Bessel-like vortex beams using Pr^{3+} fiber laser

Yuto Yoneda[1], A Srinivasa Rao[1,2], Yasushi Fujimoto[3], Katsuhiko Miyamoto[1,2], and Takashige Omatsu[1,2]

[1]Graduate School of Engineering Chiba University Chiba 263-8522, Japan
[2]Molecular Chirality Research Centre, Chiba University, Chiba 263-8522, Japan
[3]Chiba Institute of Technology,2-17-1 Tsudanuma, Narashino, Chiba 275-0016, Japan
E-mail: omatsu@faculty.chiba-u.jp

Optical vortex beams carry a ring spatial form and an orbital angular momentum (OAM) assigned by a topological charge ℓ [1], and they have been widely studied in a variety of applications, such as optical tweezers [2], microscopic imaging [3] and material processing [4]. The above mentioned applications strongly require compact and robust visible vortex sources with high efficiency.

Pr^{3+} ion-doped laser materials with strong visible emission allow the development of compact visible light sources. In fact, we and our co-workers have already demonstrated a visible optical vortex source by using Pr^{3+}: YLF and Pr^{3+}: waterproof fluoro-aluminate glass (WPFG) fiber [5,6].

In this paper, we report on the demonstration of selective oscillation of Bessel-like vortex beams from the Pr^{3+} WPFG fiber laser in combination with an intracavity lens with strong spherical aberration.

Figure 1 shows an experimental setup of our laser system. A 440 nm GaN laser diode was used as a pump source, and its output was delivered and focused onto a Pr^{3+}: WPFG fiber core (8 μm (core diameter) × 40 mm (length)) by utilizing a focusing system (L1~L5 lenses). The cavity was formed of a high reflection input fiber facet and a flat output mirror for 600-700 nm. The cavity length was then fixed to be 70 mm. A convex face of an intracavity aspheric lens L6 (f = 4.51 mm) was facing the gain medium to maximize the intra-cavity spherical aberration, thereby preventing Gaussian mode oscillation [7].

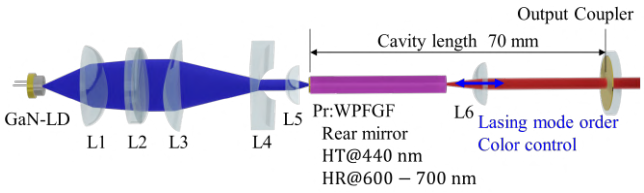

Fig. 1. Experimental setup of Pr^{3+}: WPFG vortex fiber laser.

The system showed the selective laser operation of a red (637 nm) or orange (605 nm) line by properly adjusting the position of the intracavity lens along the optical axis direction owing to chromatic aberrations. Also, red and orange outputs exhibited a multiple-ring-shaped vortex (Bessel-like vortex) profile with ℓ = +1 or -1, as evidenced by a central dark core and Y-shaped interference fringes, as shown in Fig. 2. Note that the selective control of negative or positive topological charge of the generated vortex output was achieved by appropriately adjusting the lateral position of the intracavity lens.

The maximum output powers of 605 nm and 637 nm Bessel-like vortex outputs were measured to be 20 mW and 83 mW, respectively, at the pump power of 2.3W. The system will be potentially extended to generate cyan (480 nm), green (523 nm) and deep-red (697 nm) Bessel-like vortex outputs.

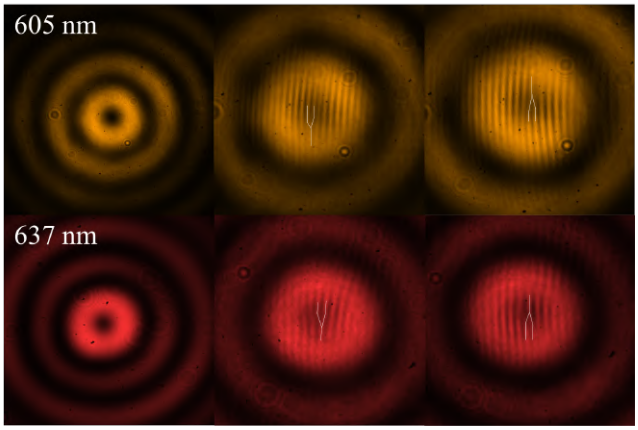

Fig. 2. Spatial forms and wave-fronts of the generated Bessel-like vortex beams.

References

[1] I. Litvin, L. Burger, and A. Forbes, J. Opt. **17**, (2015) 105614.
[2] R. A. Minz, U. Tiwari, A. Kumar, S. Nic Chormaic, K. Lahlil, T. Gacoin, S. K. Mondal, and J. Fick, OSA Continuum **4**, 2 (2021) 364-373.
[3] J. Huisken, D. Y. R. Stainier, Development **136**, 12 (2009) 1963–1975.
[4] Y. Arita, J. Lee, H. Kawaguchi, R. Matsuo, K. Miyamoto, K. Dholakia, and T. Omatsu, Opt. Lett., **45**, 14 (2020) 4080-4083.
[5] A. S. Rao, K. Miamoto, and T. Omatsu, Opt. Exp. **28**, 25 (2020) 37397-37405.
[6] W. R. Kerridge-Johns, A. S. Rao, Y. Fujimoto, and T. Omatsu, Opt. Express **31**, 10 (2023) 16607-16614.
[7] A. S. Rao, T. Morohashi, W. R. Kerridge-Johns, and T. Omatsu, J. Opt. Soc. Am. B **40**, 2 (2023) 406-411.

[23p-A310-1~5] 4.7 Quantum Optics, Nonlinear Optics and Structured Optics

Takashige Omatsu(Chiba Univ.)

Sat. Sep 23, 2023 1:00 PM - 2:30 PM A310 (KJ Hall)

△ : Presentation by Applicant for JSAP Young Scientists Presentation Award

▲ : English Presentation

▼ : Both of Above

No Mark : None of Above

▲[23p-A310-1] [JSAP-Optica Joint Symposia 2023 Invited Talk] Laser Scanning Microscope Techniques with Structured Light Beams Enabling Super-Resolution Imaging and Rapid Three-Dimensional Imaging

○Yuichi Kozawa[1], Yuuki Uesugi[1], Shunichi Sato[1] (1.IMRAM, Tohoku Univ.)

1:00 PM - 1:30 PM

▲[23p-A310-2] Femtosecond optical vortex-induced flower-shaped surface relief in azo-polymer

○Kana Ishihara[1], Katsuhiko Miyamoto[2,1], Takashige Omatsu[2,1] (1.Chiba Univ, 2.MCRC, Chiba Univ)

1:30 PM - 1:45 PM

▼[23p-A310-3] MW Peak Power UV laser by Fourth Harmonic Generation in $YAl_3(BO_3)_4$ crystal

○(P)Florent Cassouret[1], Arvydas Kausas[2], Pascal Loiseau[3], Gerard Aka[3], Daniel Rytz[4], Takunori Taira[1,2] (1.Inst. for Molecular Science, 2.Riken Spring-8 Center, 3.Chimie ParisTech Research Inst., 4.Coherent)

1:45 PM - 2:00 PM

▲[23p-A310-4] High Harmonic Generation from a Microplasma Source

○(D)Maria Carla Lupu[1], Filchito Renee Bagsican[1], Tatsunosuke Hanano[1], Michael Man[1], Julien Madeo[1], Keshav Dani[1] (1.OIST)

2:00 PM - 2:15 PM

▲[23p-A310-5] High-repetition rate table-top XUV source with narrow linewidth and long-term stability for time-resolved photoemission spectroscopy

○(PC)Filchito Bagsican[1], Jacques Hawecker[1], David Bacon[1], Xing Zhu[1], Vivek Pareek[1], Maria-Carla Lupu[1], Prajakta Kokate[1], Harley Suchiang[1], Michael Man[1], Julien Madeo[1], Keshav Dani[1] (1.FSU, OIST)

2:15 PM - 2:30 PM

Laser Scanning Microscope Techniques with Structured Light Beams Enabling Super-Resolution Imaging and Rapid Three-Dimensional Imaging

IMRAM, Tohoku Univ., ◦Yuichi Kozawa, Yuuki Uesugi, Shunichi Sato

E-mail: y.kozawa@tohoku.ac.jp

The amplitude, phase, and polarization of light are the fundamental parameters that characterize light waves. In general, Gaussian beams with uniform phase and polarization distribution on the beam cross-section are mostly used in many applications using laser light beams. By contrast, when these parameters are spatially distributed on the beam cross-section, unique properties that cannot be attained by conventional light beams are manifested. Such light beams are also called structured light beams and have attracted much attention in recent years.

Radially and azimuthally polarized beams are well-known structured light beams, also referred to as cylindrical vector beams, which are characterized by axially symmetric polarization distributions. Due to the axial symmetry of polarization, vector beams exhibit distinctive behaviors when strongly focused by a high numerical aperture (NA) lens. For example, a radially polarized beam can produce a strong longitudinal electric field at the focus, which has a feature of a small focal spot compared to a conventional linearly or circularly polarized beam. This feature is particularly advantageous to enhancing the spatial resolution in laser scanning microscopy [1]. We have recently revealed that a higher-order radially polarized Laguerre-Gaussian (LG) beam can generate an extremely small focal spot, also known as superoscillation spot, by precisely controlling the incident beam size of a radially polarized LG beam on the pupil plane of an objective lens [2]. The use of the superoscillation focal spot in confocal laser scanning fluorescence microscopy enabled the significantly enhanced lateral spatial resolution approaching 100 nm even when a visible excitation beam was used.

In this talk, we will briefly review the use of structured light beams, including vector beams, in laser scanning microscopy to enhance spatial resolution. In addition, we will also introduce a new type of three-dimensional imaging technique that can be realized by controlling the spatial structure of light beams [3,4]. In this method, the depth information of samples is obtained from a single two-dimensional raster scanning of a light needle spot with an extended focal depth without the movement of the observation plane, allowing rapid three-dimensional image acquisition in laser scanning microscopy.

References:

[1] Y. Kozawa and S. Sato, “Small focal spot formation by vector beams” Prog. Opt. **66**, 35-90 (2021).
[2] Y. Kozawa, D. Matsunaga, S. Sato, “Superresolution imaging via superoscillation focusing of a radially polarized beam” Optica **5**, 86-92 (2018).
[3] Y. Kozawa and S. Sato, “Light needle microscopy with spatially transposed detection for axially resolved volumetric imaging,” Sci. Rep. **9**, 11687 (2019).
[4] Y. Kozawa *et al*., “Wavefront engineered light needle microscopy for axially resolved rapid volumetric imaging” Biomed. Opt. Express **13**, 1702-1717 (2022).

Femtosecond optical vortex-induced flower-shaped surface relief in azo-polymer

Kana Ishihara[1], Katsuhiko Miyamoto[1,2], and Takashige Omatsu[1,2]
1. Chiba Univ., 2. MCRC, Chiba Univ.
E-mail: omatsu@faculty.chiba-u.jp

Laguerre-Gaussian (LG) modes, that is most commonly used optical vortices, possess an orbital angular momentum (OAM) characterized by a topological charge, ℓ, associated with their helical wavefronts, and they have been widely studied in a variety of fields, such as optical manipulations, optical-quantum communication, scanning fluorescence microscopes, and materials processing [1,2]. Surface relief formation of azo-polymers occurs through single-photon or two-photon induced trans-cis isomerization, and it has the potential to develop rewritable optical data storages with high data capacity [3].
There are several demonstrations of optical vortex induced chiral surface reliefs of azo-polymers [4,5], in which the optical vortex twists the irradiated azopolymer films to form chiral surface structures owning to OAM transfer effects. Such chiral surface structures of azo-polymers will be potentially applied to the development of ultrahigh density optical data storages with the freedom of OAM.
In this presentation, we demonstrate the formation of new optical vortex induced surface reliefs, that is flower-shaped surface reliefs with petals along the azimuthal direction, via two-photon induced photoisomerization.

The experimental setup is shown in Fig. 1. An azo-polymer film was spin-coated on a slide glass, and its thickness was measured to be ~1 μm. A near-infrared femtosecond laser (wavelength: 800 nm, pulse repetition frequency: 80 MHz, pulse width: 51 fs) was used, and its output was converted into a circularly polarized optical vortex with ℓ=1 or 2 by a spiral phase plate (SPP) and a quarter wave plate (QWP). The generated optical vortex was focused to be a diameter of ~4 μm on the azo-polymer film by an objective lens (NA=0.9). The beam power of the focused optical vortex was measured to be ~35 mW. The exposure time and laser power were then fixed to be 200 seconds and 18.7 mW, respectively.
Figure 2 shows atomic force microscope (AFM) images of structured surface reliefs. A flower-shaped surface relief with 6 or 8 petals along the azimuthal direction was then created, and its diameter and height were measured to be ~3 or ~3.6μm and ~420 or ~390 nm, respectively.

Such flower-shaped surface relief formation manifests the spatial mode instability associated with third-order nonlinear effects in azo-polymers, and it offers us a new fundamental physical insight of light–matter interaction.
Also, it will be applied to develop advanced optical data storages with new freedoms of multiple number of petals reflecting a topological charge, ℓ, of the optical vortex.

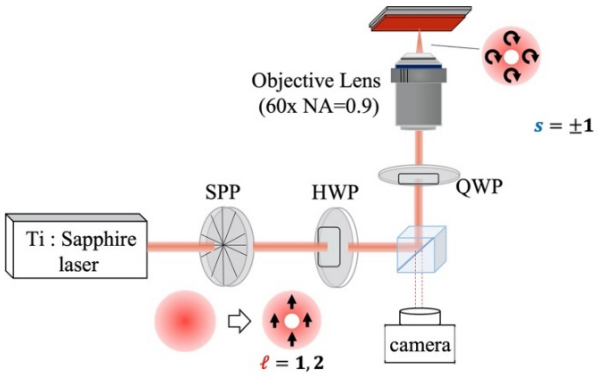

Figure 1. Experimental setup for 'flower-shaped surface relief' formation in azo-polymer film

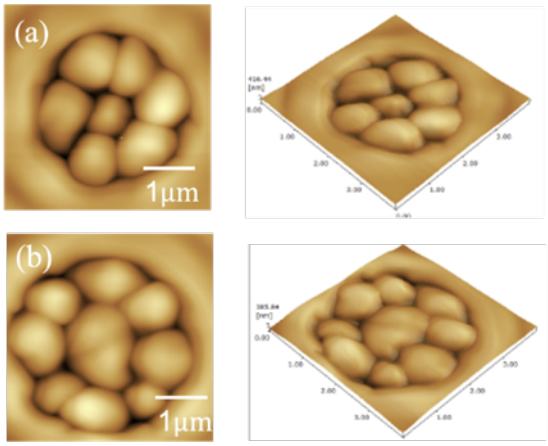

Figure 2. Surface reliefs formed by illumination of femtosecond optical vortices with (a) ℓ = 1, (b) ℓ = 2

References

[1] L. Allen, M. W. Beijersbergen, R. J. C. Spreeuw, J. P. Woerdman, Phys. Rev. A 45, 8185–8189 (1992).
[2] A. Mair, A. Vaziri, G. Weihs, A. Zeilinger, Nature 412, 313–316 (2001).
[3] W. Zhang, S. Bian, S. Kim, M. G. Kuzyk, Opt. Lett. 27, 1105–1107 (2002).
[4] T. Omatsu, K. Miyamoto, K. Toyoda, R. Morita, Y. Arita, K. Dholakia, Adv. Opt. Mater. 7, 1801672 (2019).
[5] T. Omatsu, K. Masuda, K. Miyamoto, K. Toyoda, N. M. Litchinitser, Y. Arita, K. Dholakia, J. Nanophotonics 14, 010901 (2020).

MW Peak Power UV laser by Fourth Harmonic Generation in $YAl_3(BO_3)_4$ crystal

Inst. for Molecular Science [1], Riken Spring-8 Center [2], Chimie ParisTech Research Inst. [3] , Coherent[4], Florent Cassouret [1], Arvydas Kausas [2], Pascal Loiseau [3], Gérard Aka [3], Daniel Rytz[4] and Takunori Taira [1,2]

E-mail: florent-cassouret@ims.ac.jp

1. Introduction

In 2008, $YAl_3(BO_3)_4$ (YAB) was reported as new non-hygroscopic material with good d_{eff} (0.63 pm/V) and small walk-off (1.9°) which can be a good alternative to the two commercial crystals: the hygroscopic $CsLiB_6O_{10}$ (CLBO) or to the β-BaB_2O_4 (BBO; which presents large walk-off) for UV generation at 266 nm [1]. However, until now the UV peak power obtained with YAB was only limited to the kW range [2]. In this work, we demonstrate 1.6 MW peak power at 266 nm using YAB as nonlinear crystal.

2. Experimental setup

The main source at 1064 nm was a Q-switched Nd^{3+}:YAG/Cr^{4+}:YAG-based gain aperture of micro-MOPA (Master Oscillator Power Amplifier). The cavity was build using 1.1at-% Nd^{3+}:YAG crystal as gain medium, a Cr^{4+}:YAG crystal (T_0 = 40%) as saturable absorber and an output coupler (OC) mirror with 50% reflectivity and it was pumped by 808 nm laser diode. The gain aperture was a Nd^{3+}:YAG crystal pumped by another 808 nm laser diode. This system improves output energy to 4.5 mJ (792 ps pulse duration) and beam quality (M^2 from 2.5 to 1.1) by amplifying the fundamental TEM_{00} mode and not the higher order ones [3]. Green laser at 532 nm (3.3 mJ, 619 ps pulse duration) was obtained through second harmonic generation with a type I LiB_3O_5 (LBO) crystal (θ = 90° φ = 11.4°). The green beam was finally focused (φ = 250 µm) inside an uncoated 2.94 mm thick YAB crystal oriented for the FHG at 266 nm (θ = 66.6° φ = 0°) (Fig. 1-a).

3. Results and discussion

Up to 423 µJ were obtained at 266 nm (268 ps pulse duration), corresponding to 1.6 MW peak power with a power conversion efficiency η of 32 % as can be seen in Fig. 1-b. This peak power is one order of magnitude higher than the 240 kW previously reported for YAB [3]. However, regarding theoretical conversion efficiency calculations, higher conversion can be expected with YAB material in these conditions. The difference comes from linear absorption ($T_{crystal}$ = 44 % at 266 nm due to Fe^{3+} impurities) but also from two photon absorption phenomena as the saturation of η increase with the pumping intensity.

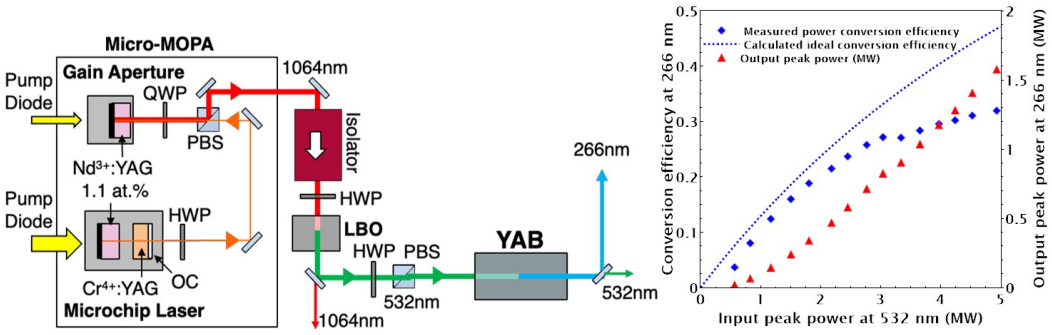

Fig. 1. Experimental setup UV light generation at 266 nm using YAB crystal (a) and obtained UV energy at 266 nm with corresponding power conversion efficiency.

4. Conclusion

Despite the limited transmission of the YAB crystal, up to 423 µJ of UV energy at 266 nm with 268 ps pulse duration were obtained by frequency conversion, corresponding to 1.6 MW peak power and 32% conversion efficiency. Further improvements are expected with the increasing of transmission at 266 nm through better growth control to open a path toward the use of longer crystals to reach >10 MW peak power. Also, two photon absorption in this material is under investigation.

Acknowledgement

This work was partially supported by Innovative Science and Technology Initiative for Security Grant Number JPJ004596, ATLA, Japan.

References

[1] D. Rytz, A. Gross, S. Vernay, V. Wesemann, in Proc. Spie, **6998**, 699814–1 – 699814–12 (2008).

[2] S. Ilas, P. Loiseau, G. Aka, T. Taira, Opt. Exp., **22**(24), 30325-30332 (2014).

[3] V. Yahia, T. Taira, Opt. Exp., **26**(7), 8609-8618 (2018).

High Harmonic Generation from a Microplasma Source

Maria Carla Lupu, Filchito Renee Bagsican, Tatsunosuke Hanano, Michael K. L. Man, Julien Madéo and Keshav M. Dani

Femtosecond Spectroscopy Unit, Okinawa Institute of Science and Technology, 1919-1 Tancha, Onna son, Okinawa, Japan, 904-0495
E-mail: kmdani@oist.jp

The nonlinear process of High Harmonic Generation (HHG) has enabled table-top ultrafast sources of coherent radiation, mainly in the extreme ultraviolet (XUV) spectral region, with extensive use in a large variety of domains, such as industry [1], biology [2], and photoemission science [3]. In particular, the latter would greatly benefit from tunable high repetition rate XUV sources, to map the electronic band structure of materials over a large range of the Brillouin Zone with fast data acquisition. Generally, in HHG experiments, the required peak intensity is reached with the use of femtosecond lasers with a pulse energy in the range of 10 µJ – 1 mJ, typically focused down to a spot diameter of 10 µm – 100 µm, respectively. Focusing the beam tighter than a few microns, thus generating a microplasma, would enable the use of sub-µJ sources. However, a microplasma HHG source is expected to lead to a very poor XUV photon flux. This assumption originates from the phase matching condition in an ultra-tight focusing geometry, where the significant contribution of Gouy phase factor cannot be balanced out. Prior HHG work based on micron-scale spot diameter [4] has shown an XUV photon flux multiple orders of magnitude lower than the requirement for photoemission experiments [3]. Here, we demonstrate experimentally the high efficiency of a microplasma XUV source [5], with a photon flux that exceeds 10^{11} photons/s/harmonic, driven by a pulse energy lower than 1 µJ. As a driving source, we use a noncolinear optical parametric amplifier system operated at 4 MHz repetition rate, from which we tune the driving wavelength between 700 nm - 900 nm. In Fig. 1, we show the measured XUV spectra, with two regimes of tunability: a) a discrete harmonic tunability ranging from 20 to 50 eV and b) a continuous tunability of about 9 eV. The generation of efficient XUV radiation with sub-µJ class sources could open a new era for spectroscopy and material science.

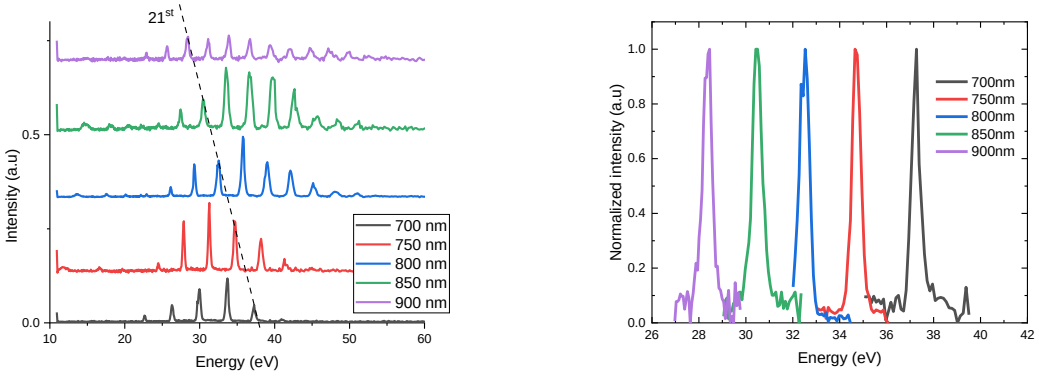

a) b)

Fig. 1. a) Measured XUV spectra for driving wavelength varied from 700 nm to 900 nm. b) Continuous tunability of the 21st harmonic.

Acknowledgments
This work is supported by the Femtosecond Spectroscopy Unit – OIST, OIST Innovative Technology Research – Proof of Concept Program, and JSPS Kakenhi Grant Nos. JP21H01020 and JP22K18270.

References
[1] D. Gardner, et al., Nature Photon 11, 259–263 (2017).
[2] P. D. Baksh, et al., Sci Adv. 6 (2020).
[3] J. Madéo, et al., Science 370, 1199-1204 (2020).
[4] A. Blättermann, CT. Chiang, and W. Widdra, Physical Review, A 89, 043404 (2014).
[5] J. Madeo, M. K. L. Man, K. M. Dani, US20200333559A1 (2020).

High-repetition rate table-top XUV source with narrow linewidth and long-term stability for time-resolved photoemission spectroscopy

Filchito Renee G. Bagsican, Jacques Hawecker, David Bacon, Xing Zhu, Vivek Pareek, Maria-Carla Lupu, Prajakta Kokate, Harley Suchiang, Michael K.L. Man, Julien Madéo, and Keshav M. Dani

Femtosecond Spectroscopy Unit, Okinawa Institute of Science and Technology Graduate University
E-mail: kmdani@oist.jp

1. Introduction

The emergence of table-top XUV sources has ushered in a new era of multidimensional photoemission spectroscopy that allowed access to the nature and dynamics of excited states in various material systems [1]. Here we present our XUV source that operates at 2 MHz with very high signal-to-noise, long-term stability, and narrow linewidth that has been instrumental to our recent achievements in understanding exciton physics in 2D semiconductors [2-4].

2. Experimental set-up and source characteristics

Time-resolved photoemission spectroscopy is a powerful tool in studying the dynamical evolution of excited states in materials. Fig. 1 illustrates the typical scheme employed in our experiments. A portion of the output from a Yb-doped fiber amplifier is used to drive a non-colinear parametric amplifier to produce a widely tunable photoexcitation source (320-2500 nm). Another portion is used to produce XUV through high-harmonic generation (HHG) using our patented technology [5].

Our technology uses a very tight focusing of the pump laser, typically < 5µm, which allows the use of lower pulse energies (< 10 µJ) and long pulse durations (> 200 fs) to reach the required laser intensity for HHG [5]. The ability to use uncompressed pulses directly from the Yb-doped fiber amplifier greatly reduces the complexity of the experiment. Furthermore, having a small XUV source (< 5 µm) allows us to achieve a small XUV probe on the sample spot (FWHM < 10µm) with just a single XUV ellipsoidal mirror placed in a 2f-2f configuration. This is critical for studying micron-sized samples like exfoliated 2D materials.

We use 21.7 eV (9^{th} harmonic) as XUV probe in our photoemission experiments. This harmonic is separated from the other harmonics and the excess pump laser using a set of Al and Sn filters. A Si plate set at grazing angle is then used to guide the XUV onto the sample. At typical operating conditions, we use around 7 µJ of pump laser (515nm, ~250fs pulse duration, 2 MHz repetition rate) for HHG, which gives an estimated flux of ~1 x 10^{11} ph/s on the sample and a linewidth of < 30 meV. Actual photoemission counts using this XUV source show < 3% RMS variation over a 10-hour period and < 7% for a 1 week-period.

3. Performance demonstration using 2D materials

We demonstrated the performance of our XUV source for momentum microscopy by probing the dynamics of excitons in atomically thin semiconductors [2-4]. The high-repetition rate and long-term stability of our source, in addition to the small spot size and narrow linewidth, were key to obtaining high-quality data with reasonable acquisition time. With a properly prepared monolayer semiconductor sample, our static ARPES measurements at 100K routinely show FWHM linewidths < 90 meV, which to the best of our knowledge, is the best energy resolution achieved on a monolayer semiconductor using a table-top XUV source.

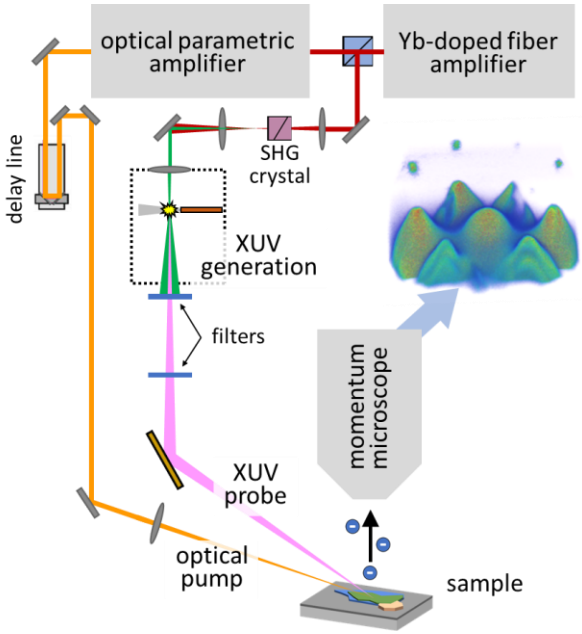

Fig. 1 Experimental set-up.

Acknowledgements

This work is supported by the Femtosecond Spectroscopy Unit – OIST Graduate University, OIST Graduate University Innovative Technology Research – Proof of Concept Program, and JSPS Kakenhi Grant Nos. JP21H01020 and JP22K18270.

References

[1] Karni, O., *et. al*, Adv. Mater. (2022) 2204120.
[2] Madéo, J., *et. al*, Science **370**, 6521 (2020) 1199-1204.
[3] Man, M.K.L., *et. al*, Sci. Adv. **7**, 17 (2021) eabg0192.
[4] Karni, O., *et. al*, Nature **603** (2022) 247-252.
[5] US patent 11,372,199.

4 JSAP-Optica Joint Symposia 2023 | Oral presentation | 4.8 Optica Special Lecture

[20a-A602-1~1] 4.8 Optica Special Lecture

Takuo Tanaka(RIKEN)

Wed. Sep 20, 2023 9:00 AM - 10:00 AM A602 (KJ Hall)

△：Presentation by Applicant for JSAP Young Scientists Presentation Award

▲：English Presentation

▼：Both of Above

No Mark：None of Above

▲[20a-A602-1] Terahertz integrated photonics based on photonic crystals and silicon microstructures

○Masayuki Fujita[1] （1.Osaka Univ.）

9:00 AM - 10:00 AM

9:00 AM - 10:00 AM (Wed. Sep 20, 2023 9:00 AM - 10:00 AM A602)

▲[20a-A602-1] Terahertz integrated photonics based on photonic crystals and silicon microstructures

○Masayuki Fujita[1] (1.Osaka Univ.)

Keywords: tba